

For Reference

NOT TO BE TAKEN FROM THIS ROOM

For Reference

NOT TO BE TAKEN FROM THIS ROOM

Ex LIBRIS
UNIVERSITATIS
ALBERTAENSIS



UNIVERSITY OF ALBERTA
LIBRARY

Regulations Regarding Theses and Dissertations

Typescript copies of theses and dissertations for Master's and Doctor's degrees deposited in the University of Alberta Library, as the official Copy of the Faculty of Graduate Studies, may be consulted in the Reference Reading Room only.

A second copy is on deposit in the Department under whose supervision the work was done. Some Departments are willing to loan their copy to libraries, through the inter-library loan service of the University of Alberta Library.

These theses and dissertations are to be used only with due regard to the rights of the author. Written permission of the author and of the Department must be obtained through the University of Alberta Library when extended passages are copied. When permission has been granted, acknowledgement must appear in the published work.

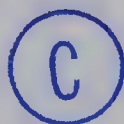
This thesis or dissertation has been used in accordance with the above regulations by the persons listed below. The borrowing library is obligated to secure the signature of each user.

THE UNIVERSITY OF ALBERTA

A LIQUID HELIUM NEUTRON POLARIMETER AND ITS APPLICATION

TO THE REACTION $^{28}\text{Si}(\text{d},\text{n})^{29}\text{P}$

by



Sheung Tsing Lam

A THESIS

SUBMITTED TO THE FACULTY OF GRADUATE STUDIES

IN PARTIAL FULFILLMENT OF THE REQUIREMENTS FOR THE DEGREE

OF DOCTOR OF PHILOSOPHY

DEPARTMENT OF PHYSICS

EDMONTON, ALBERTA

July, 1967



Digitized by the Internet Archive
in 2019 with funding from
University of Alberta Libraries

<https://archive.org/details/Lam1967>

UNIVERSITY OF ALBERTA

FACULTY OF GRADUATE STUDIES

The undersigned certify that they have read, and recommend to the Faculty of Graduate Studies for acceptance, a thesis entitled A LIQUID HELIUM NEUTRON POLARIMETER AND ITS APPLICATION TO THE REACTION $^{28}\text{Si}(\text{d},\text{n})^{29}\text{P}$, submitted by Sheung Tsing Lam in partial fulfillment of the requirements for the degree of Doctor of Philosophy.

Abstract

A neutron time-of-flight system using a 5.5 MeV Van de Graaff with a Mobley compression magnet was set between the target and liquid helium polarimeter for the measurement of fast neutron polarization. The polarization system was calibrated with neutrons from the $D(d,n)^3\text{He}$ reaction at deuteron energies of 3.0, 4.0, 5.0 and 6.0 MeV and at a neutron emission angle of $45^\circ(\text{c.m.})$. Good agreement was found between the present measurements and those of Dubbeldam and Walter.

The polarization angular distributions of neutrons to the ground, 1.38 and 1.96 MeV states of ^{29}P from the reaction $^{28}\text{Si}(d,n)^{29}\text{P}$ were measured at a deuteron energy of 5.0 MeV. The polarization angular distribution corresponding to the ground state ($\ell_p=0$) group is in good qualitative agreement with the derivative rule. Spin dependent effects are observed in the polarization distributions of the 1.38 ($j=\ell_p - \frac{1}{2}$) and the 1.96 ($j=\ell_p + \frac{1}{2}$) MeV states.

The DWBA code written by B.E.F. Macefield was used in the calculation of neutron polarization. Fair agreement between the DWBA prediction and the polarization measurements to the ground state of ^{29}P is found, but there is very poor agreement for the 1.38 MeV state. As for the 1.96 MeV state there is some agreement in the shape of the polarization distribution in the forward angles.

Acknowledgment

I would like to express my gratitude to my supervisor, Professor J.T. Sample for his suggestion of the interesting research project and his able guidance throughout.

I would like to thank Professor W.K. Dawson for his help and suggestions in computer programming, and Professor G.C. Neilson for his guidance in fast neutron time-of-flight techniques.

I am indebted to Mr. D.A. Gedcke for his help in assembling the electronic system and his participation throughout the project. I am also thankful to Drs. G.M. Stinson and S.M. Tang for their help during the long period of data collection. Particular thanks are due to Mr. T.B. Grandy for his suggestions and help in computer programming. I would also like to thank Dr. G. Roy for his help in making the silicon targets.

I am very grateful to Messrs. J.B. Elliott, C. Green, L. Holm and the rest of the technical staff of the Nuclear Research Center for their help throughout the project.

I would also like to thank the technical staff of the Low Temperature Laboratory, especially Mr. H. McClung, for their assistance in handling liquid helium.

Thanks are also due to Miss G. Tratt for her meticulous efforts in typing the thesis.

Finally, I would like to thank the National Research Council for a studentship and the University of Alberta for financial support during the course of this work.

TABLE OF CONTENTS

| | | |
|-------------|--|----|
| | INTRODUCTION | 1 |
| CHAPTER I | LIQUID HELIUM POLARIMETER | 3 |
| 1-1 | Introduction | 3 |
| 1-2 | A Comparison of Different Scatterers | 5 |
| 1-3 | Liquid Helium Cryostat | 8 |
| 1-4 | Analysing Power of Helium | 11 |
| CHAPTER II | EXPERIMENTAL ARRANGEMENT | 15 |
| 2-1 | Production of a 1 ns Pulsed Beam | 15 |
| 2-2 | Experimental Configuration | 17 |
| 2-3 | Electronic Configuration | 19 |
| 2-4 | False Asymmetry | 39 |
| CHAPTER III | CALIBRATION OF THE POLARIZATION SYSTEM WITH D(d,n) ^3He NEUTRONS | 48 |
| CHAPTER IV | POLARIZATION PREDICTIONS FROM DIRECT REACTION THEORY | 56 |
| CHAPTER V | NEUTRON POLARIZATION FROM THE $^{28}\text{Si}(d,n)^{29}\text{P}$ REACTION | 68 |
| 5-1 | Experimental Details | 68 |
| 5-2 | Ground state of ^{29}P | 71 |
| 5-3 | The 1.38 and 1.96 MeV states of ^{29}P | 73 |
| 5-4 | DWBA Predictions | 81 |
| 5-5 | Compound and Direct Effects | 88 |

| | | |
|------------|---|-----|
| APPENDIX 1 | CALCULATION OF THE $n\text{-}^4\text{He}$ ANALYSING POWER | 93 |
| A1-1 | Principle of Calculation | 94 |
| A1-2 | Description of the Computer Program | 103 |
| APPENDIX 2 | SOME SCHEMATIC DRAWINGS | 122 |
| REFERENCES | | 125 |

FIGURES

| | Page |
|---|------|
| 1-1 Geometrical arrangement in a polarization experiment | 4 |
| 1-2 The analysing powers of ^4He , ^{12}C and ^{16}O as calculated from the known phase shifts | 6 |
| 1-3 A schematic drawing of the liquid helium cryostat | 9 |
| 1-4 n - ^4He phase shifts | 14 |
| 2-1 Block diagram of the Van de Graaff accelerator and the Mobley magnet system | 16 |
| 2-2a A layout of the experimental arrangement | 18 |
| 2-2b Pictures of the polarization system | 20 |
| 2-3 A block diagram of the electronic arrangement of the polarization system | 21 |
| 2-4 A block diagram of the time-to-amplitude conversion system | 22 |
| 2-5 Anode time shift correction | 23 |
| 2-6 An electronic block diagram for the generation of a shift table | 25 |
| 2-7 A picture of the TWOD spectrum taken directly from the display unit of the on-line computer system | 27 |
| 2-8 Shift table | 31 |
| 2-9 Time resolution of the polarimeter by means of a neutron source | 32 |
| 2-10 Corrected and uncorrected neutron time-of-flight spectra | 33 |

Figures continued

| | | |
|------|---|----|
| 2-11 | Time resolution of the polarimeter using the .511 MeV γ -rays of ^{22}Na | 35 |
| 2-12 | Energy resolution of the polarimeter obtained from a linear channel against the position of a ^{239}Pu α -particle source | 36 |
| 2-13 | A picture of the $^{28}\text{Si}(d,n)^{29}\text{P}$ neutron time-of-flight spectra taken directly from the computer display unit | 40 |
| 2-14 | A block diagram for setting the threshold of the neutron detectors | 42 |
| 2-15 | ^{22}Na γ -ray spectrum | 42 |
| 2-16 | Time-of-flight spectra to show the effectiveness of the shadow bars | 46 |
| 3-1 | Polarization measurements of neutrons from the $\text{D}(d,n)^3\text{He}$ reaction around 45° (c.m.) | 50 |
| 5-1 | The energy level diagram of the nucleus ^{29}P | 69 |
| 5-2 | A neutron time-of-flight spectrum of the $^{28}\text{Si}(d,n)^{29}\text{P}$ reaction with $E_d=5.0$ MeV, $\theta = 60^\circ$ (lab) and flight path = 2m. | 70 |
| 5-3 | Angular distribution and polarization angular distribution of neutrons to the ground state of ^{29}P | 72 |
| 5-4 | The j-dependence effect as seen from the angular distributions of the 1.38 and 1.96 MeV states of ^{29}P at $E_d = 4.0, 5.0, 6.0, 7.0$ and 9.0 MeV | 76 |
| 5-5 | Angular distributions and polarization angular distributions of neutrons to the 1.38 and 1.96 MeV states of ^{29}P | 78 |
| 5-6 | A comparison between "JULIE" and the DWBA code written by Macefield | 82 |
| 5-7 | DWBA predictions for the angular distribution and polarization angular distribution of neutrons corresponding to the ground state of ^{29}P | 85 |

Figures continued

| | | |
|------|--|-----|
| 5-8 | DWBA predictions for the angular distribution and polarization angular distribution of neutrons corresponding to the 1.38 MeV state of ^{29}P | 86 |
| 5-9 | DWBA predictions for the angular distribution and polarization angular distribution of neutrons corresponding to the 1.96 MeV state of ^{29}P | 87 |
| 5-10 | Yield functions of neutrons corresponding to the ground state of ^{29}P | 89 |
| 5-11 | Yield functions of neutrons corresponding to the 1.38 MeV state of ^{29}P | 90 |
| 5-12 | Yield functions of neutron corresponding to the 1.96 MeV states of ^{29}P | 91 |
| A1-1 | A schematic drawing of the polarization configuration | 94 |
| A2-1 | A schematic drawing for mounting a RCA 8575 phototube to the tail section of the cryostat | 123 |
| A2-2 | A schematic drawing of the channel iron cart for mounting the polarization system | 124 |

TABLES

| | Page |
|--|------|
| 2-1 Shift Table and Time Resolution for the Polarimeter | 29 |
| 3-1 Neutron Polarization Measurements from the $D(d,n)^3\text{He}$ Reaction at $\theta=45^\circ$ (c.m.) | 55 |
| 5-1 Polarization Measurements of Neutrons to the ground state of ^{29}P | 74 |
| 5-2 Polarization Measurements of Neutrons to the 1.38 MeV state of ^{29}P | 79 |
| 5-3 Polarization Measurements of Neutrons to the 1.96 MeV state of ^{29}P | 80 |
| 5-4 Optical Model Parameters used in the $^{28}\text{Si}(d,n)^{29}\text{P}$ Reaction at Deuteron energy of 5.0 MeV | 84 |
| A1-1 An Alphabetic List of Definitions and Symbols used in the Helium Analysing Power Program | 104 |
| A1-2 Input Quantities of the Helium Analysing Power Program | 106 |
| A1-3 A Sample Output of the Helium Analysing Power Program | 107 |

INTRODUCTION

In the study of neutron producing reactions, although both the incident beam of particles and the target are unpolarized, the outgoing neutrons are in general found to be polarized. This is due to the spin-orbit coupling in nuclear reactions. Since the polarization vector of the outgoing neutrons is normal to the reaction plane and the neutron has an intrinsic spin of $1/2$, the neutron spin orientations can only be up or down. If in a beam of neutrons, the number with spins up is N_+ and those with spins down is N_- , the polarization of the beam can be defined as:

$$P = \frac{N_+ - N_-}{N_+ + N_-}$$

If N_+ is equal to N_- , the polarization is zero. If either N_- or N_+ is zero, the polarization is ± 1 .

Schwinger (Sc 46, Sc 48) was the first to indicate the importance of polarization studies in nuclear research. Lepore (Le 50) made detailed calculations based on Schwinger's suggestions and Wolfenstein (Wo 49, Wo 54, Wo 56) made extensive studies in the case of nucleon-nucleon scattering. Blin-Stoyle (Bl 51) was the first to make the observation that polarized neutrons should be a frequent product of nuclear reactions. Blatt and Biedenharn (Bl 52) were first to give a complete account of the polarization angular distribution.

The picture of particle polarization from a stripping reaction was first put forward by Newns (Ne 53) in terms of nuclear absorptive distortion. Since the Butler plane wave theory (Bu 51) does not account for polarization, the distorted wave Born approximation (Au 63) is introduced. Neglecting the spin-orbit term in the optical potentials, the upper limit for polarization is $33\frac{1}{3}\%$ and for the case where the orbital angular momentum transfer of the captured particle is zero, the prediction for polarization is zero (Hu 58, Bi 60). Since polarization measurements have shown these to be not true, spin-orbit potentials are introduced in the distorted wave Born approximation. It has been shown that to the first order the angular distribution is independent of, while polarization depends linearly on, the spin-orbit potentials (Jo 62), so polarization measurements should be a more sensitive way of testing the strength of spin-orbit potentials in a nuclear reaction. With the availability of high speed and large memory computers, programs (Ba 61, Sa 64, Ma 64, To 66) have been written for distorted wave Born approximation calculations with spin-orbit potentials.

The object of this thesis is to report on the construction and application of a liquid helium polarimeter and the comparison of neutron polarization measurements from the reaction $^{28}\text{Si}(d,n)^{29}\text{P}$ with the distorted wave Born approximation predictions.

There has been a conflict in sign convention in discussions of polarization. The Basel sign convention (Ba 60A) is adopted in this thesis. This prescribes a positive sign of polarization in the direction $\vec{k}_{\text{in}} \times \vec{k}_{\text{out}}$, where \vec{k}_{in} and \vec{k}_{out} are the momenta of the incident beam of particles and the outgoing particles, respectively.

CHAPTER I

LIQUID HELIUM POLARIMETER

1-1 Introduction

Since neutrons produced from a nuclear reaction are usually polarized and conventional detectors cannot distinguish the spin orientations of the neutrons detected, special arrangements have to be used to measure polarization. While experiments using a polarized beam of particles or a polarized target have been performed, elastic scattering from nuclei is most commonly used in the study of polarization. The various techniques in the measurement of polarization have been described by Haeberli in Chapter V.G. of Fast Neutron Physics Part II (Ha 63) and the following description will be devoted entirely to the system adopted at this laboratory.

Fig. 1-1 shows a typical arrangement in a polarization experiment. If an incident beam of particles with momentum \vec{k}_1 hits a target, the polarization, \vec{P}_1 , of the neutron emitted at an angle θ_1 is given by:

$$\vec{P}_1 = P_1 \vec{n}_1$$

where \vec{n}_1 is a unit vector normal to the reaction plane and along the direction defined by $\vec{k}_1 \times \vec{k}_2$. If now such a beam of neutrons is elastically scattered, the differential cross section of the scattered neutrons is given by:

$$\sigma(\theta_2, \phi) = \sigma(\theta_2) [1 + P_1 P_2 (\vec{n}_1 \cdot \vec{n}_2)] \quad (1-1)$$

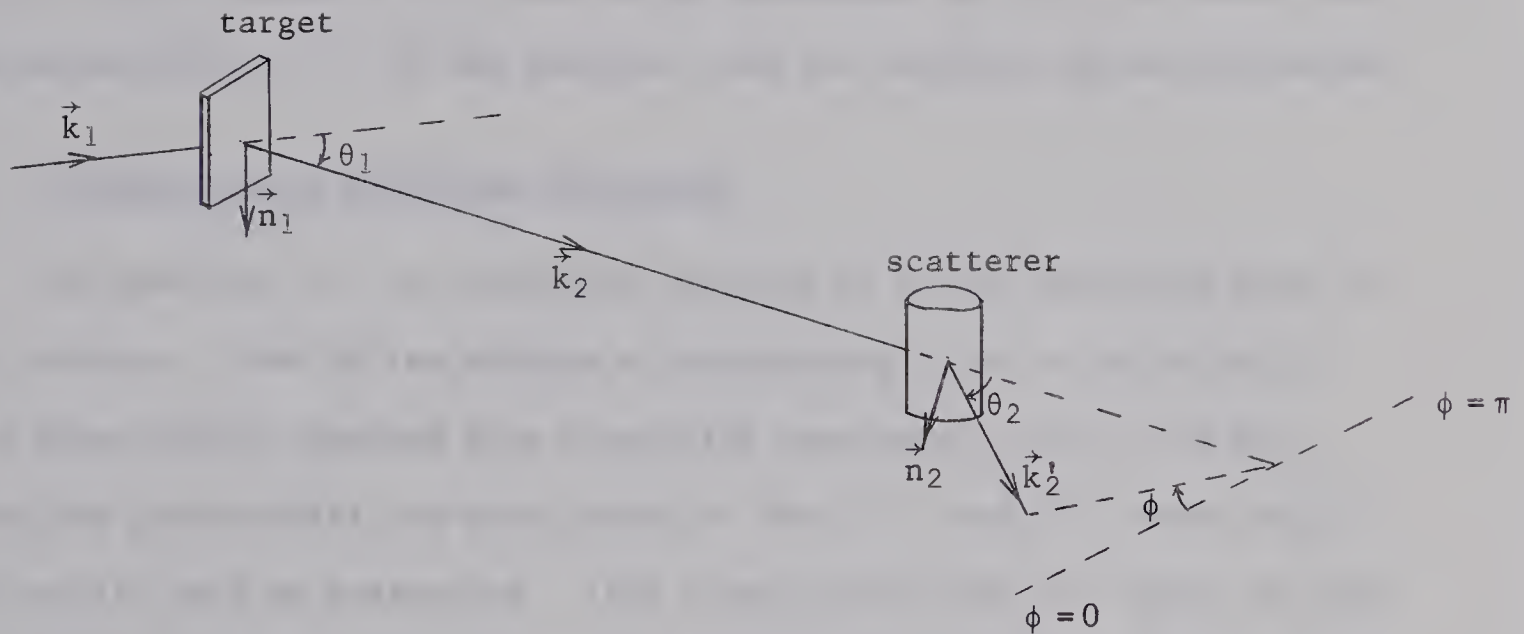


Fig. 1-1. Geometrical arrangement in a polarization experiment

where $\sigma(\theta_2)$ = the scattering cross section if the incident beam of neutrons were unpolarized

P_2 = polarization of the scattered neutrons if the incident beam of neutrons were unpolarized

\vec{n}_2 = a unit vector normal to the scattering plane and along the direction $\vec{k}_2 \times \vec{k}_2'$

and $\cos \phi = \vec{n}_1 \cdot \vec{n}_2$

If now a neutron detector is placed at $(\theta_2, 0)$ and another at (θ_2, π) , the right-left asymmetry, ϵ , is given by

$$\epsilon = \frac{\sigma(\theta_2, 0) - \sigma(\theta_2, \pi)}{\sigma(\theta_2, 0) + \sigma(\theta_2, \pi)}$$

$$= P_1 P_2$$

(1-2)

Since ϵ can be measured in a scattering experiment and if P_2 is known also, the polarization, P_1 , of the neutrons from the reaction can be determined.

1-2 A Comparison of Different Scatterers

The quantity, P_2 , is frequently referred to as the analysing power of the scatterer. One of the methods of determining P_2 is to calculate it from phase shifts obtained from scattering experiments (Se 53, Ho 66). Since the phase shifts are best known for ^4He , ^{12}C and ^{16}O , these nuclei are usually used as scatterers. Also these nuclei have zero spin, so that for a given incident orbital angular momentum, ℓ , there are only two partial wave phase shifts, δ_ℓ^\pm , corresponding to the total angular momenta, $J = \ell \pm \frac{1}{2}$ respectively. The analysing power can then be written as:

$$P = - \frac{2\text{Im}(g^*h)}{|g|^2 + |h|^2} \quad (1-3)$$

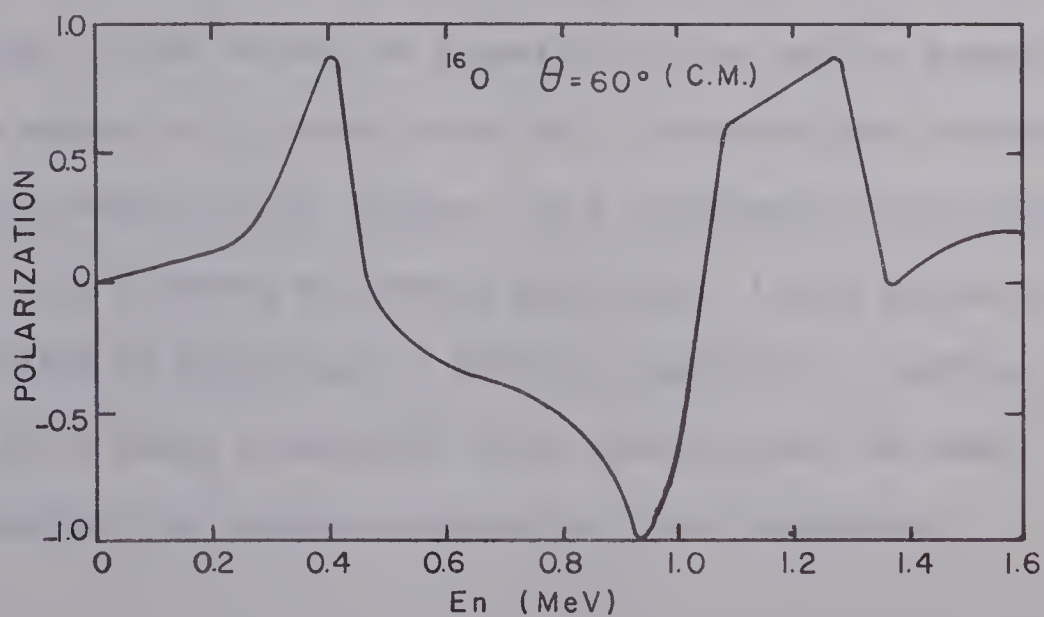
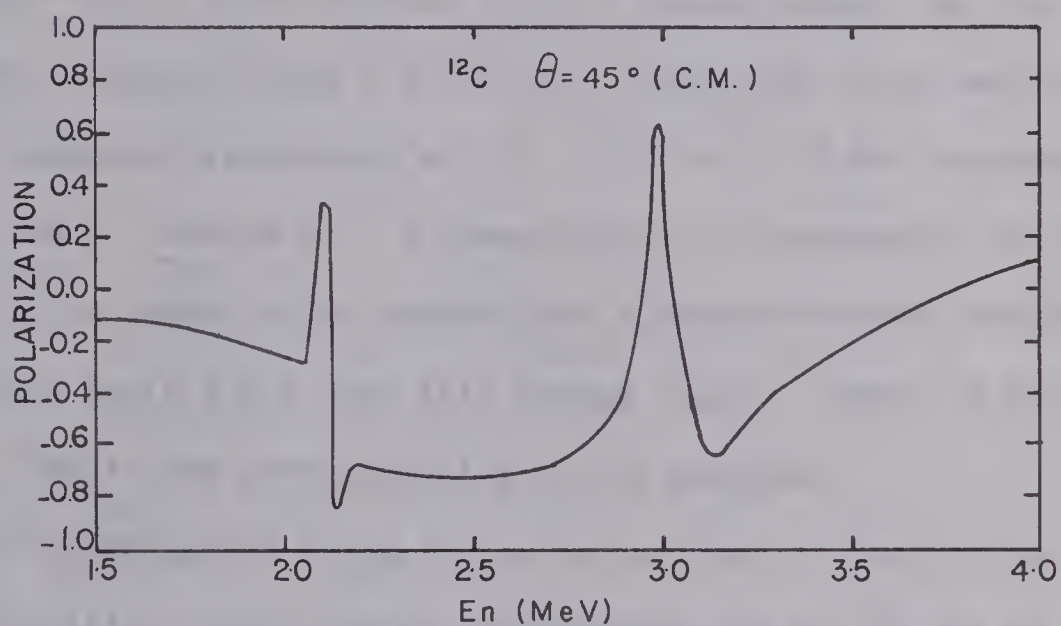
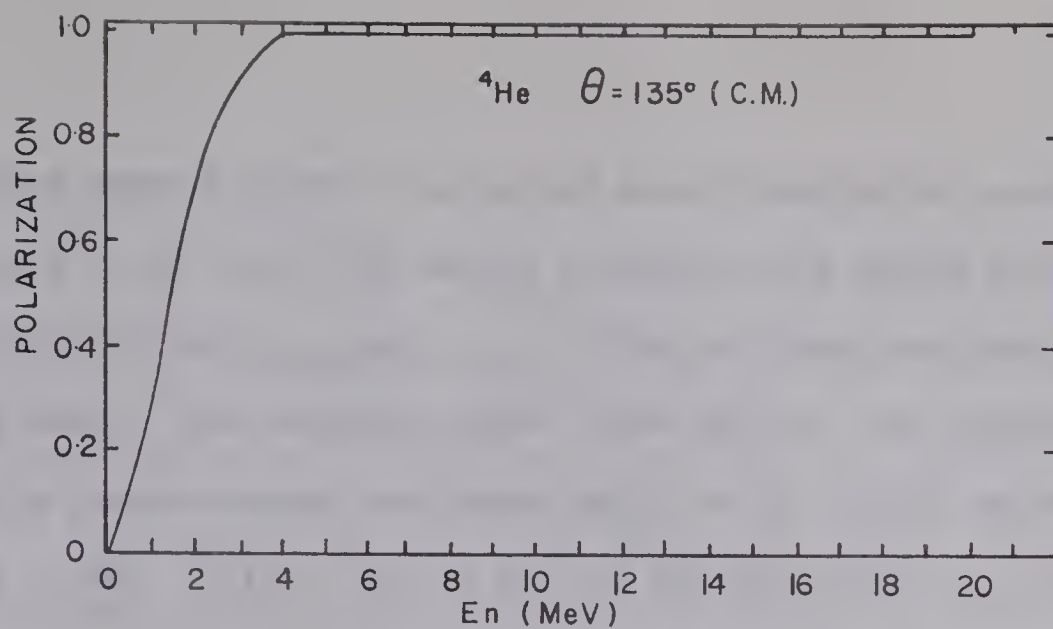
$$\text{where } g = (1/k) \sum_{\ell} P_{\ell}(\cos\theta) [(\ell+1) \sin \delta_{\ell}^+ e^{i\delta_{\ell}^+} + \ell \sin \delta_{\ell}^- e^{i\delta_{\ell}^-}]$$

$$h = (1/k) \sum_{\ell} P_{\ell}^{(1)}(\theta) \sin(\delta_{\ell}^+ - \delta_{\ell}^-) e^{i(\delta_{\ell}^+ + \delta_{\ell}^-)}$$

$P_{\ell}(\cos\theta)$ and $P_{\ell}^{(1)}(\theta)$ are the Legendre and associated Legendre polynomials and Im represents the imaginary part of the quantity inside the brackets. Hence the analysing power of the scatterer can be calculated from the phase shifts.

Fig. 1-2 shows the analysing powers of ^4He , ^{12}C and ^{16}O calculated from the known phase shifts (Ha 63). At a centre-of-mass scattering angle of 135° ,

Fig. 1-2. The analysing powers of ^4He , ^{12}C and ^{16}O as calculated from the known phase shifts (Ha 63)



the analysing power for ${}^4\text{He}$ is large and slowly-varying for neutrons of energy from 3 to 20 MeV. This smooth variation with energy is due to the two very broad states, $p_{3/2}$ and $p_{1/2}$, in ${}^5\text{He}$ and these two phase shifts contribute most to the analysing power below 20 MeV. The analysing power for ${}^{12}\text{C}$ at a centre-of-mass scattering angle of 45° varies drastically at 2.08 and 2.95 MeV. This is due to the two narrow states, $d_{5/2}$ and $d_{3/2}$, in ${}^{13}\text{C}$. Between 2.2 and 2.8 MeV the analysing power is large and slowly-varying, so ${}^{12}\text{C}$ is a good analyser in this energy range. As for ${}^{16}\text{O}$, even for neutrons of energy below 1.5 MeV, the scattering cross section shows three well separated resonances at .43, 1.00 and 1.31 MeV corresponding to $\frac{3^-}{2}$, $\frac{3^+}{2}$ and $\frac{3^-}{2}$ states in ${}^{17}\text{O}$ respectively. Consequently the analysing power of ${}^{16}\text{O}$, as shown in the diagram for a centre-of-mass scattering angle of 60° , varies quite a bit over this energy region. Hence of the three scatterers, ${}^4\text{He}$ is the most generally useful analyser.

Another advantage of using ${}^4\text{He}$ as an analyser is that it has been found to scintillate under neutron bombardment (Th 59, Fl 59, Si 61, To 61, Es 65). Since the scintillation signal is proportional to the helium recoil energy, it can be used as a measure of the neutron bombarding energy. Also such a signal can be used to set up a time-of-flight system, which is the technique adopted in our system. As a polarization experiment is essentially like a double scattering experiment, liquid helium is used in our case instead of helium gas in order to improve the counting rate. Since liquid helium is used, a specially built cryostat must be used. The following section describes the cryostat employed in this laboratory.

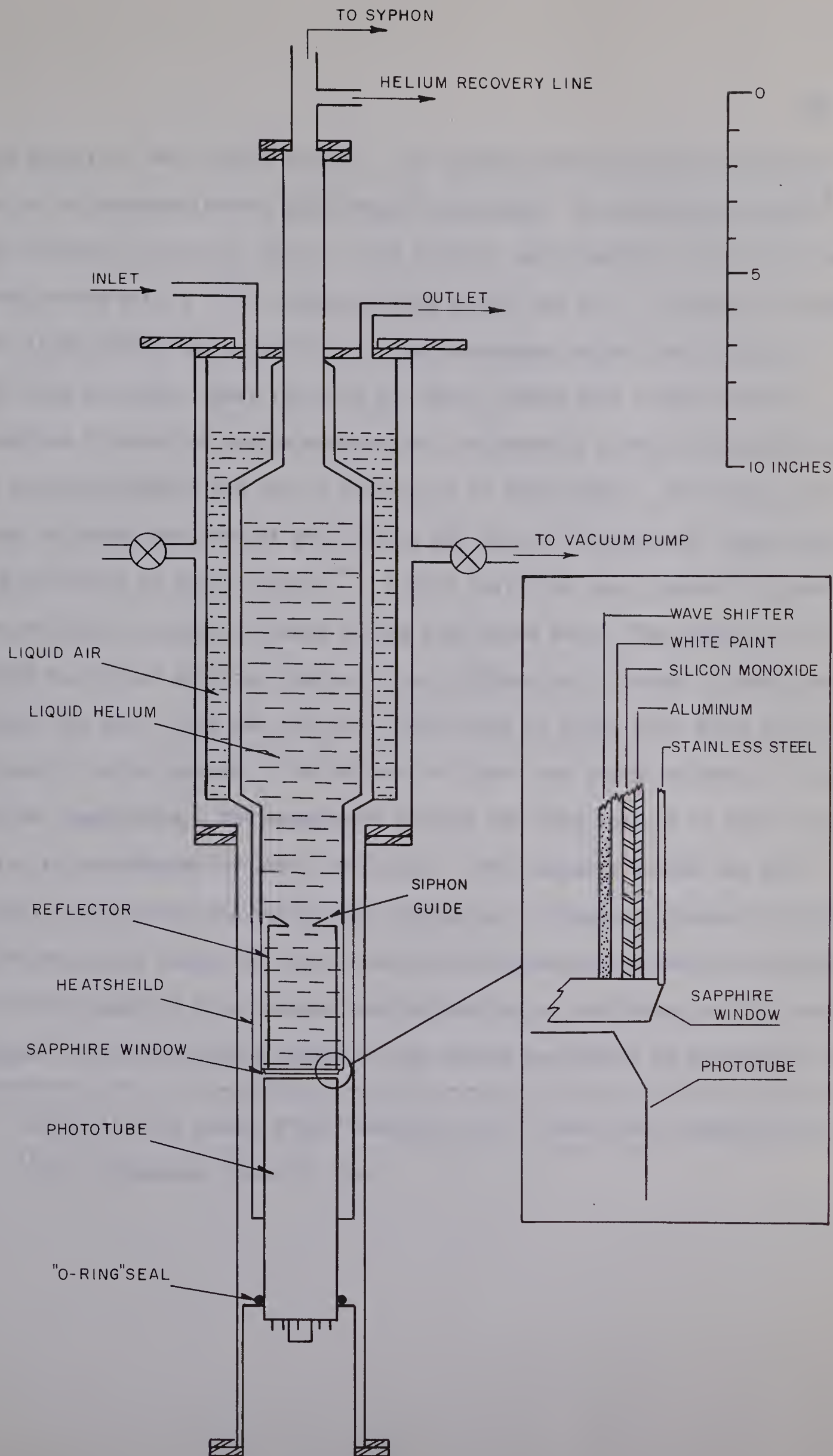
1-3 Liquid Helium Cryostat

Fig. 1-3 shows a schematic drawing of the liquid helium cryostat, which was manufactured by Hofman Cryogenics (Si 61, Ka 63). It is a stainless steel dewar, the central part of which is a liquid helium reservoir of 1 litre capacity. Surrounding it is a liquid air reservoir to reduce the temperature gradient between the liquid helium reservoir and the outside. The space in between the two reservoirs and the outer wall is under high vacuum. A copper heat shield extends from the bottom of the liquid air reservoir down to the thin section of the polarimeter. The scattering volume of the polarimeter is at the bottom end of the liquid helium reservoir, with a wall thickness of .010". It is defined by a .010" stainless steel cylinder of 2" in diameter and 4" in height. A hole 1/4" in diameter at the top of the cylinder allows liquid helium to pass through. An artificial sapphire window 2" in diameter allows the scintillation signal to be observed by a RCA8575 phototube placed 1/8" beneath the sapphire window. The phototube is sealed in vacuum by means of an O-ring at the base of the tube.[†] A vacuum of about 2×10^{-7} mm of mercury is attained by means of a 2" Edwards mercury diffusion pump and a mechanical rotary fore-pump.

Since the scintillation of the helium recoil is in the ultraviolet region ($\sim 1600 \text{ \AA}$), a wavelength shifter must be used on the scattering volume to bring

[†]Fig. A2-1 in Appendix 2 shows a schematic drawing of the mounting of the phototube.

Fig. 1-3. A schematic drawing of the liquid helium cryostat



the signal to the visible region. The commonly used wavelength shifters are pp'-diphenylstilbene, quaterphenyl and popop. pp'-diphenylstilbene[†] was chosen in our case, since it was found to give the best energy resolution when tested with a ²³⁹Pu alpha-particle source (Si 61). In order to improve the light-collecting properties of the scattering volume, the inside of the thin stainless steel cylinder was first coated with a thin layer of aluminum by means of vacuum evaporation, followed by a thin protective layer of silicon monoxide and then a fine layer of white paint. The paint was made by mixing one part of zinc oxide, one part of transparent Tygon paint^{††} and two parts of Tygon thinner^{††}. Coarse particles were removed by draining the paint through a funnel filled with glass wool. The paint so prepared was poured onto the inside of the cylinder and allowed to drain and dry before the next layer was put on. Four layers of paint were found sufficient to give a white surface; a thick layer of paint was found to crack at liquid helium temperature. The wavelength shifter was then applied by slow evaporation to a thickness of about 100 $\mu\text{g}/\text{cm}^2$. The sapphire window was also lightly coated with the wavelength shifter to a thickness of about 50 $\mu\text{g}/\text{cm}^2$. Since the pulse height of the helium scintillations was found to deteriorate if frozen gases or water vapour were collecting at the bottom of the scattering volume, the liquid helium reservoir was always kept under an atmosphere of

[†] Scintillation grade, Pilot Chemicals, Inc., Watertown, Massachusetts

^{††} U.S. Stoneware, Akron 9, Ohio

helium while not in use. Liquid helium was transferred at the top of the cryostat by means of a double-walled siphon. A brass cone was attached on top of the 1/4" hole of the thin stainless steel cylinder to act as a siphon guide (see Fig. 1-3) so that one arm of the siphon could be inserted into the scattering volume while transferring, as this would reduce the initial splashing of liquid helium.

Two carbon resistors of 16K each were suspended by means of fine electric wires from the top of the cryostat, so that one was 5" and the other 16" from the bottom of the scattering volume. These two resistors acted as a liquid helium level indicator, as their resistance increased to 2M when immersed in liquid helium. One fill of liquid helium used about 3 litres of liquid helium and lasted for about 3-1/2 hours. The helium gas was recovered through a brass pipe leading back to the storage tank of the liquefier.

1-4 The Analysing Power of Helium

Phase shifts for $n\text{-}^4\text{He}$ scattering have usually been derived from the more accurately known $p\text{-}^4\text{He}$ phase shifts by accounting for the difference in the Coulomb energies so that the corresponding energy levels in ^5He and ^5Li are matched. The Dodder-Gammel-Seagrave phase shifts (Do 52, Se 53) for neutrons of energy below 20 MeV have long been used to calculate the helium analysing power. Gammel, Thaler and Perkins determined another set of phase shifts for neutrons of energy above 10 MeV (Ga 58). However, these two sets of phase shifts do not connect smoothly nor do they fit the available

data above a neutron energy of 15 MeV (Ho 66). For this reason, Hoop and Barschall (Ho 66) determined another set of phase shifts covering the neutron energy range from .5 to 30 MeV. In their case, the n - ${}^4\text{He}$ phase shifts for neutron energy above 17 MeV were derived from the Weitkamp-Haeberli p - ${}^4\text{He}$ phase shifts (We 66) and the s - and p -wave phase shifts were joined smoothly to the Dodder-Gammel-Seagrave phase shifts at low energies. The analysing power calculated from this set agrees very well with polarization measurements using the polarized neutrons from the $T(p,n){}^3\text{He}$, $D(d,n){}^3\text{He}$ and $T(d,n){}^4\text{He}$ reactions, covering the neutron energy range 6 to 24 MeV.

For neutrons of energy below 8 MeV, which is the energy range of our interest, the s - and p -waves are most important in the partial wave analysis of the scattering data, as the d -waves are small and can be neglected. Since the s - and p -wave phase shifts can be determined accurately, the calculated analysing power can be used with confidence in this low energy range.

At a neutron energy of 22.16 MeV, the 17.669 MeV state of ${}^5\text{He}$ is reached. Since $J = \frac{3}{2}^+$ for this state, the $d_{3/2}$ phase shift varies drastically at this energy. Also with the onset of the ${}^4\text{He}(n,d)T$ reaction, the phase shifts become complex and uncertain. Hence the analysing power for helium was calculated only up to 20 MeV for our system. The Hoop-Barschall phase shifts were used, and since the highest neutron energy used was 20 MeV, partial waves above d -wave were neglected. For convenience in the computation of the analysing power, the phase shifts were expressed as a power series in neutron energy by means of a least squares fitting program[†]. The expressions are

[†]Written by W. G. Davies, Ph.D. thesis (1966), Department of Physics, University of Alberta.

given below:

$$\delta_0 = 180 - 21.7684E^{1/2} - 2.63613E + .68954E^{3/2}$$

for $E \leq 20$ MeV

$$\delta_1^- = 2.45763E + 3.55942E^2 - .505754E^3$$

for $E \leq 2$ MeV

$$\delta_1^- = -10.9749 + 14.8534E - .97544E^2 + .0197815E^3$$

for $2 < E \leq 20$ MeV

$$\delta_1^+ = 684.93 - 2312.49E^{1/2} + 2493.53E - 807.582E^{3/2}$$

for $E \leq 2$ MeV

$$\delta_1^+ = .0648862 + 180.513E^{1/2} - 92.6748E + 19.1394E^{3/2} - 1.43251E^2$$

for $2 < E \leq 20$ MeV

$$\delta_2^- = -.0725766E + .0133187E^2 \text{ for } 8 \leq E \leq 20 \text{ MeV}$$

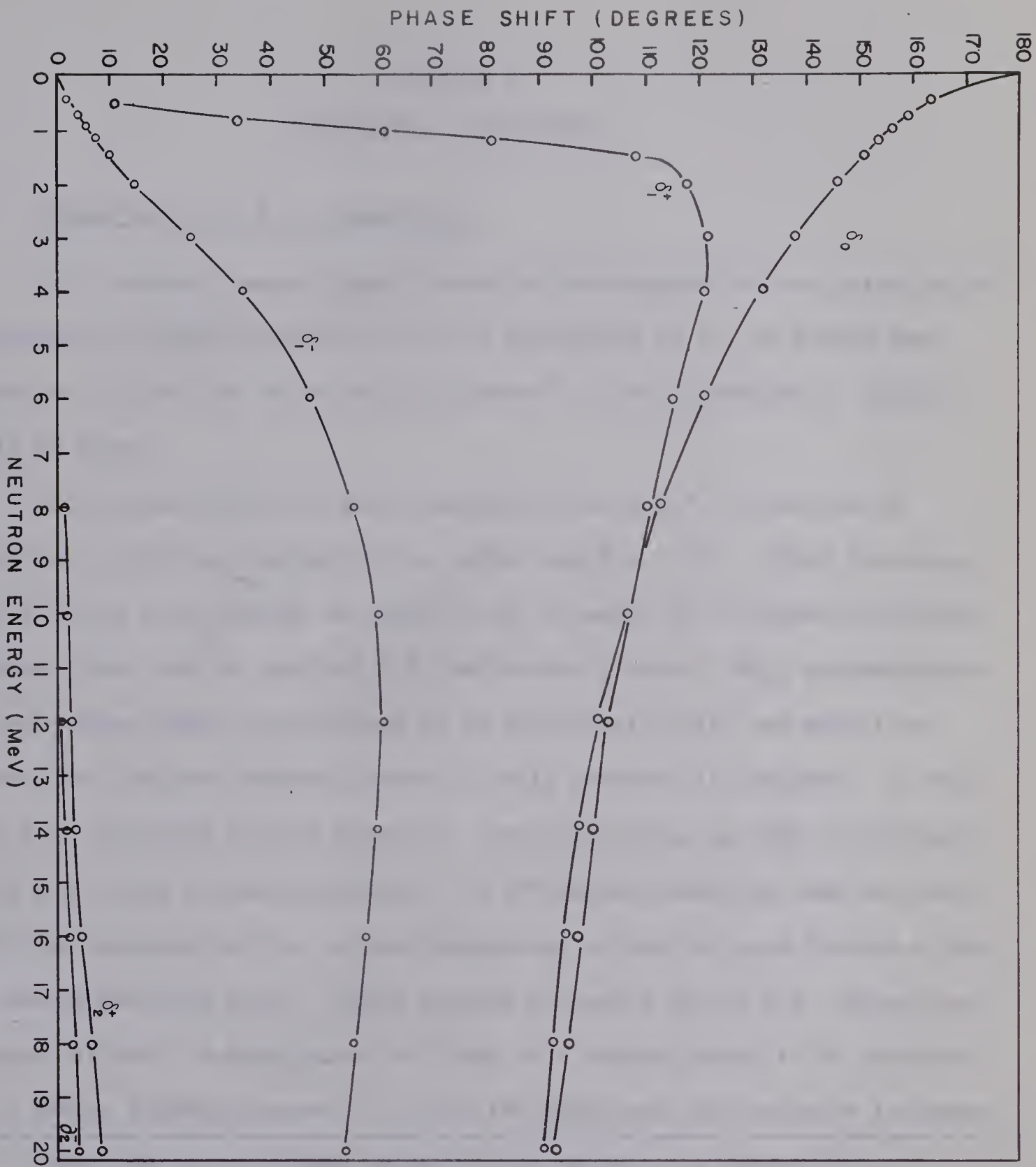
$$\delta_2^+ = .128117E - .0084296E^2 + .00110985E^3$$

for $8 \leq E \leq 20$ MeV

In Fig. 1-4 the points represent the Hoop-Barschall phase shifts while the curves represent the fitted values as calculated from the above expressions.

A computer program has been written to calculate the n-⁴He analysing power for a finite size scatterer and a finite size detector. A description and a listing of the program are given in Appendix 1.

Fig. 1-4. $n\text{-}^4\text{He}$ phase shifts



CHAPTER II

EXPERIMENTAL ARRANGEMENT

2-1 Production of a 1 ns Pulsed Beam

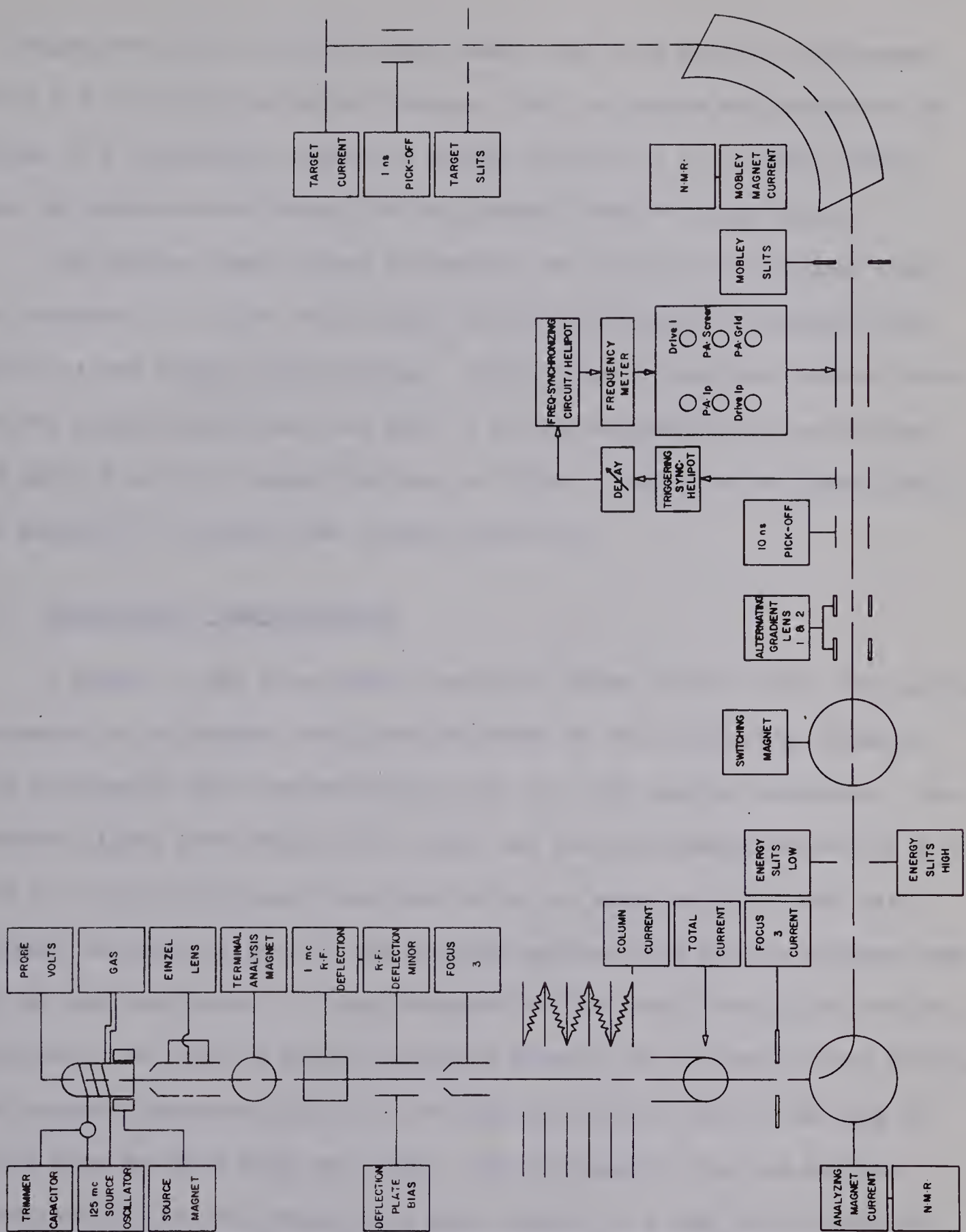
As a neutron time-of-flight technique was employed in the polarization experiment, a brief description of the production of a 1 ns pulsed beam with the 5.5 MeV Van de Graaff accelerator[†] at the University of Alberta will be given.

The ionized deuterium gas is expelled from a R.F. ion source by applying a positive voltage to the probe (see Fig. 2-1). After focussing, the ions are bent through an angle of 25° by means of a terminal analysing magnet. Two sets of parallel R.F. deflection plates (1 MHz) perpendicular to each other sweep the ion beam in an elliptical orbit, and only that portion of the beam sweeping across a small aperture is accepted. In this way a 10 ns pulsed beam is produced. The pulsed beam is then accelerated down the column of the accelerator. A 90° magnet bends the beam horizontally and deuterons of the correct energy are allowed to pass through a pair of energy defining slits. After passing through a set of R.F. deflection plates (10 MHz), a beam pulse is tilted to a correct angle to be accepted by a Mobley bunching magnet^{††}. Since the front part of the pulse traverses

[†]Model CN Van de Graaff, High Voltage Engineering Corporation, Burlington, Massachusetts.

^{††}Spectromagnetic Industries Ltd., Hayward, California

Fig. 2-1. Block diagram of the Van de Graaff accelerator and the Mobley magnet system



a longer orbit than the end of the pulse, the 10 ns pulse is compressed into a 1 ns or shorter pulse (Da 66A). The 1 ns pulses are picked off by means of a cylindrical capacitor placed in front of the target chamber and are used as stop pulses for the neutron time-of-flight system.

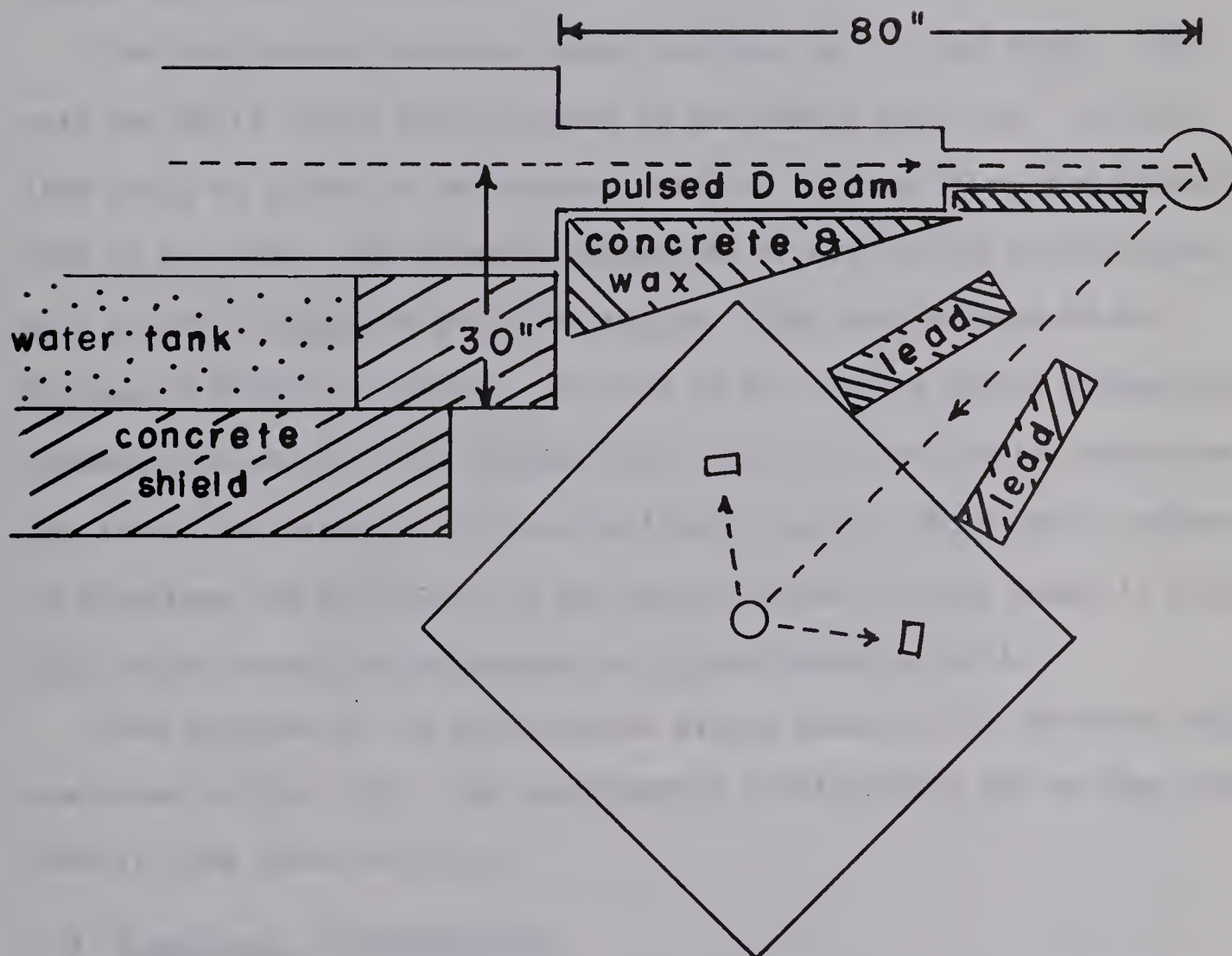
The average beam current is measured at the insulated target, which is connected to a +300 volt source, to prevent secondary electrons produced at the target from escaping. The maximum average beam current used in the present experiment was about 3 μ a corresponding to a peak current of about 3 ma for a repetition rate of 1 MHz. Damage to the target would be serious if a higher beam current were used.

2-2 Experimental Configuration

A layout of the experimental set-up is shown in Fig. 2-2a. The neutrons produced at the target were first scattered by the scattering volume of the polarimeter and then detected by the two side neutron detectors. The neutron flight path between the target and the polarimeter was set at 2 m. The two neutron detectors were each set at an angle of 123° (lab) with respect to the direction of the incident neutron beam and the distance was 25 cm from the centre of the polarimeter to the front face of the neutron detector. In order to prevent neutrons produced at the target from hitting the neutron detectors directly, two lead shadow bars each 60 cm long by 20 cm wide by 25 cm high were used. The polarimeter, the two neutron detectors and the two shadow bars were mounted on a cart[†] which could be

[†]A schematic drawing of the cart is shown in Fig. A2-2 in Appendix 2.

Fig. 2-2a. A layout of the experimental arrangement



rotated from -20° to $+120^\circ$ about the centre of the target chamber. Also the two neutron detectors could be rotated about the centre of the polarimeter from 75° to 130° .

The two neutron detectors were identical in size and shape. They were two NE213 liquid scintillators of the bubble free type[†], so that they could be placed at any position without worrying about the expansion bulb on the side. The internal dimensions of each of the scintillators were 3-1/2" in diameter and 2" in height. They were mounted on two Philips 5" XP1040 phototubes. As well as the μ -metal shield around the phototube provided by the manufacturer, another thick μ -metal shield was put around the assembly of the scintillator and the phototube to reduce to a minimum the gain shift of the phototube due to stray magnetic fields. This thick μ -metal shield served as a light shield as well.

Two pictures of the polarization system taken at two different angles are shown in Fig. 2-2b. The experimental configuration can be seen quite clearly from these pictures.

2-3 Electronic Configuration

Fig. 2-3 shows a block diagram of the electronics of the polarization system. A neutron time-of-flight technique is used to resolve neutrons of different energies. The scintillation signal from the scattering volume of the polarimeter is used as a start signal for the time-of-flight system, while the pulse from the Mobley capacitor pick-off is used as a stop signal. The electronics for the two side neutron detectors are identical. A fast coincidence is set between the polarimeter and each of the two side detectors

[†] Nuclear Enterprises Corporation, Winnipeg, Manitoba

Fig. 2-2b. Pictures of the polarization system

The top picture shows the whole assembly as viewed from the direction of the target chamber. At the bottom of the picture is the stainless steel target chamber; beyond that are the two neutron detectors marked A and B. The two lead shadow bars are in between the target chamber and the neutron detectors. The liquid helium polarimeter is seen straight ahead of the target chamber. The lower picture shows a side view of the assembly. In this picture the mercury diffusion pump and the rotary fore-pump are seen on the left-hand side.

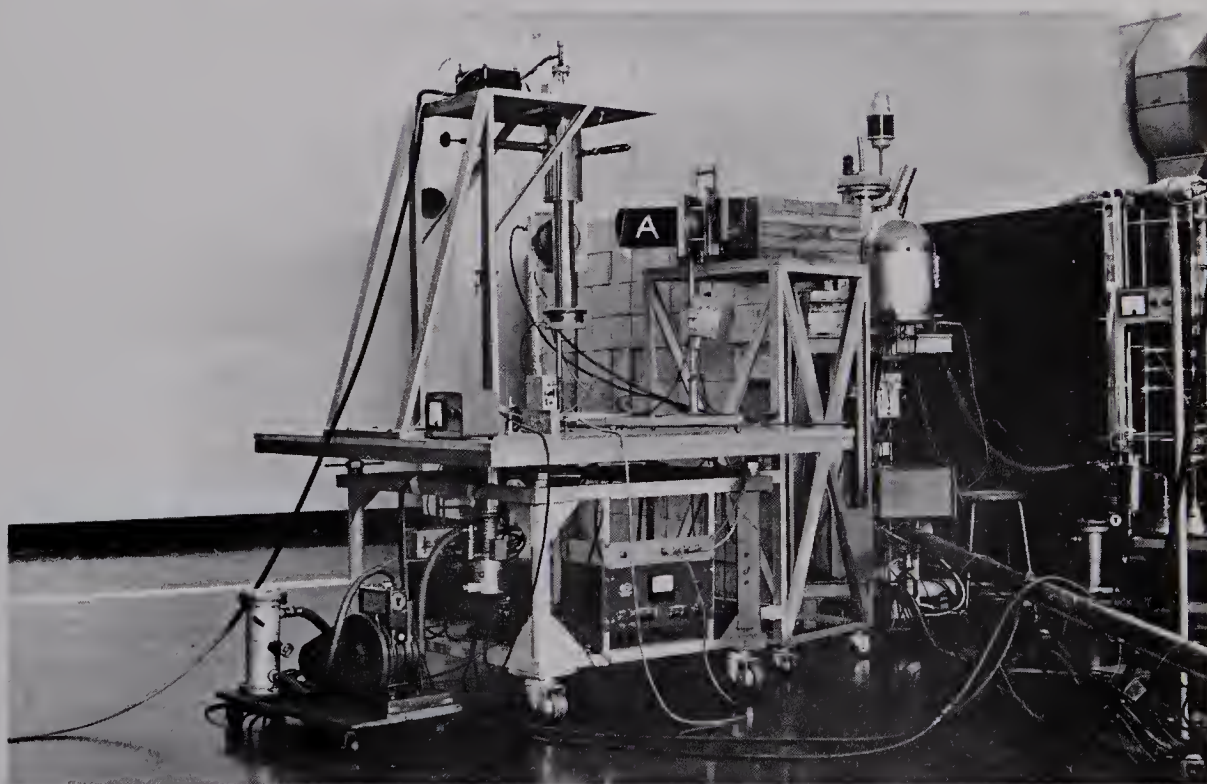
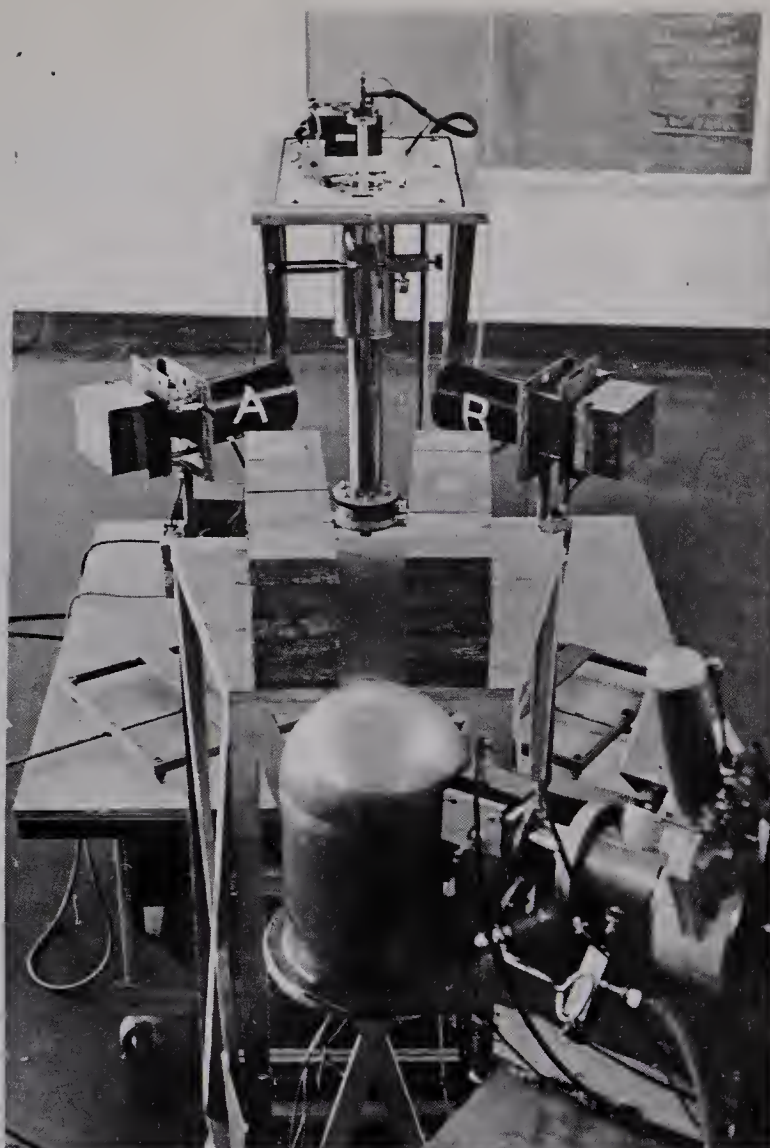
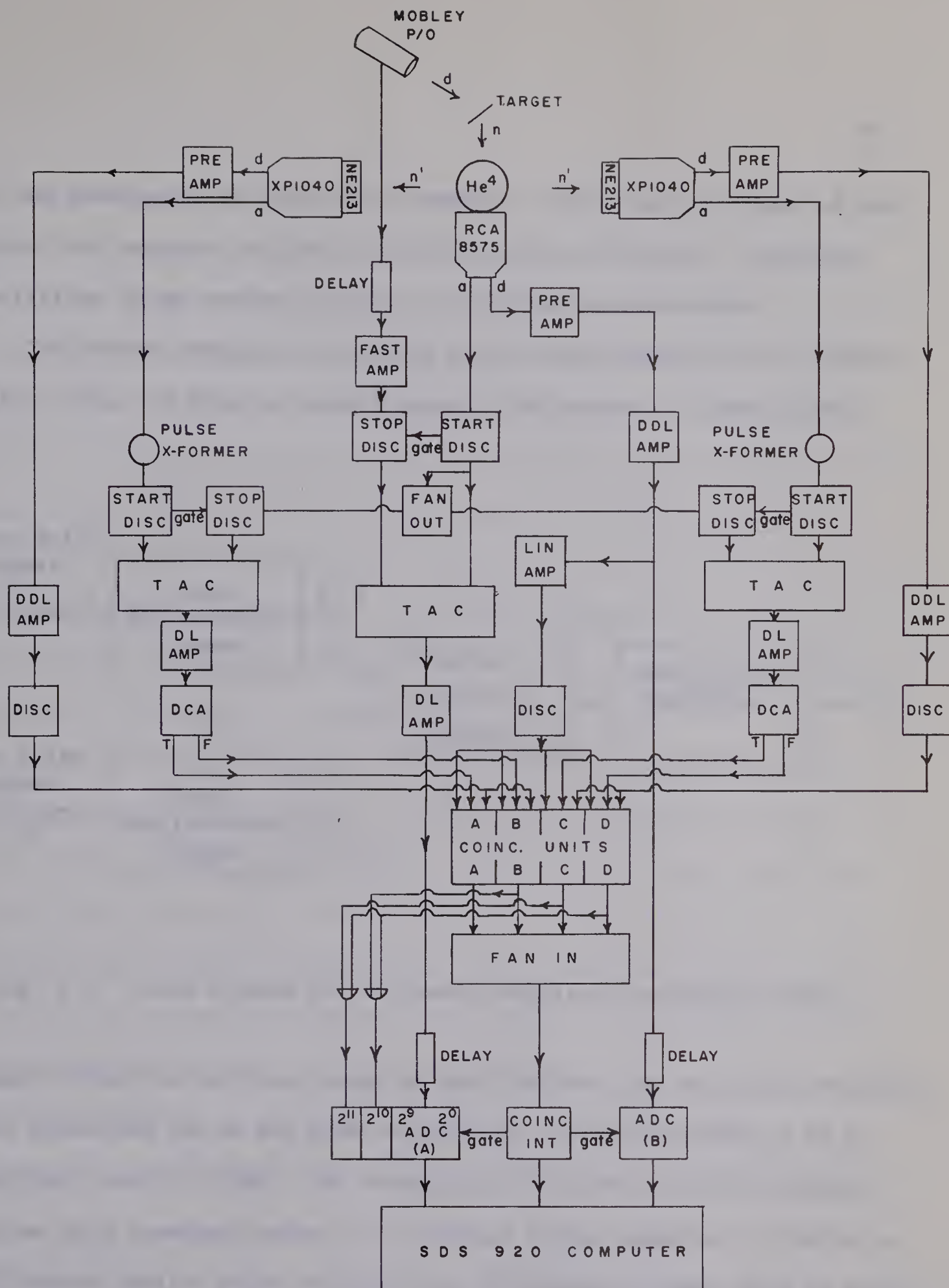


Fig. 2-3. A block diagram of the electronic arrangement of the polarization system



for the measurement of right-left asymmetry. The output of dynode 13 from each of the detectors is used to set the neutron threshold. A detailed description of the system is given in the following paragraphs.

The time-to-amplitude conversion system was designed by D. L. Wieber (Wi63). Fig. 2-4 shows a block diagram of the system. A tunnel diode

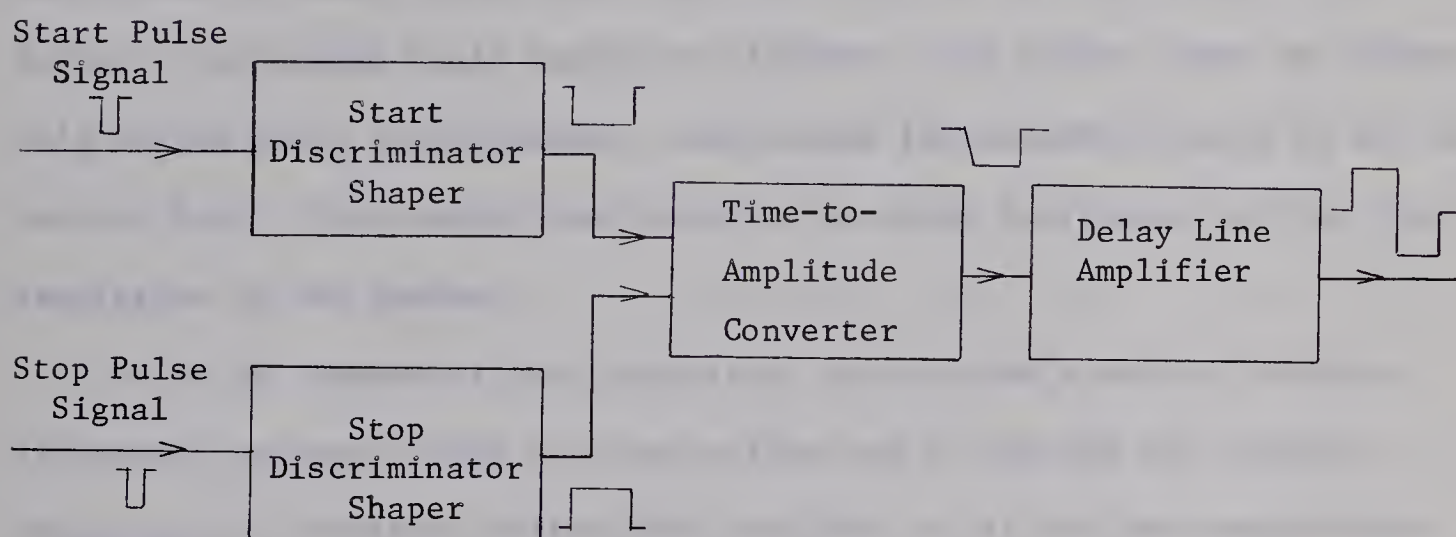


Fig. 2-4. Block diagram of the time-to-amplitude conversion system.

trigger is used at the input stage of both the start and stop discriminators, whose thresholds can be set from 10 to 600 mV. They are stable up to a repetition rate of 10 MHz. The output pulse from the start discriminator switches on a constant current, I , to charge a mica capacitor, C , which is kept charged until a pulse from the stop discriminator comes along to switch it off. If the time interval between the start and stop pulses is τ , the voltage, V_c , across the capacitor will be $V_c = \frac{I}{C} \tau$. Since I/C remains

constant, a time interval can be converted linearly into a related pulse height. The integral linearity of the system was found to be about 1%.

In the polarization experiment, a RCA8575 phototube is used to observe the scintillation signals in the scattering volume of the polarimeter and the anode pulses are used as start signals for the time-of-flight system. Even for a monoenergetic source of neutrons bombarding the polarimeter, the pulse height would still vary with the direction of the helium recoil. Hence a time spread would result as different size pulses cross the threshold of the start discriminator, even though the threshold could be set as low as 30 mV. This anode time shift is the chief limitation for the time resolution of the system.

Dr. W. K. Dawson of this laboratory has written a general purpose kicksorter program (GPKS) for the on-line use of the SDS 920 computer. There are two routines, called TWOD and TOFA, in it for the compensation of this anode time shift. The TWOD routine is to generate a shift table to be used for the TOFA routine, which gives a corrected time-of-flight spectrum for neutrons of different energy groups. A description of these two routines will be given in the next paragraph.

Fig. 2-5 shows the underlying principle in the TWOD routine. Pulses a, b and c represent events due to neutrons of the same energy but with

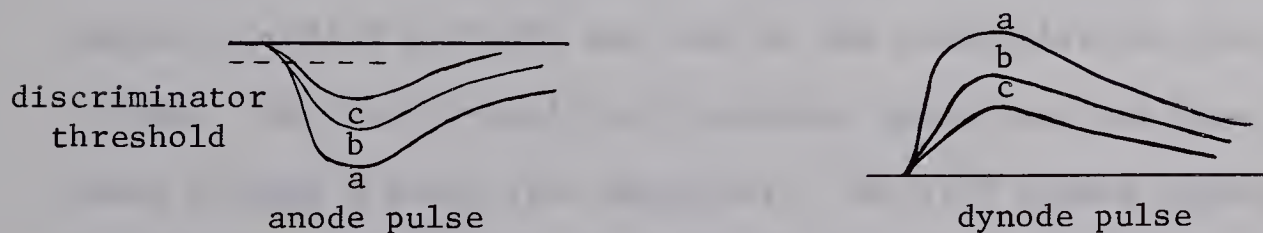
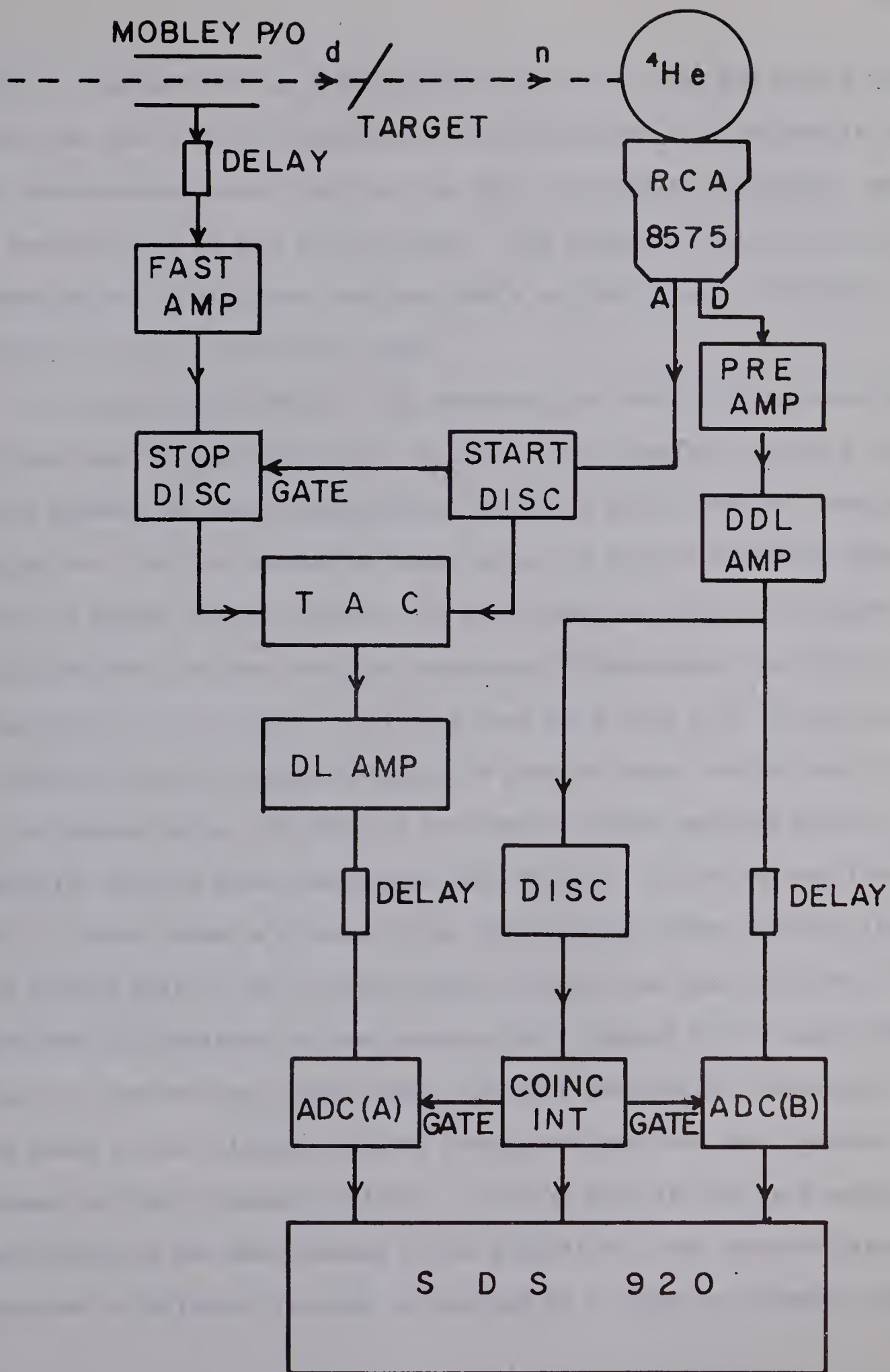


Fig. 2-5

different helium recoil directions. They should all be detected at the same time. Of these three pulses, pulse a crosses the discriminator threshold at an earlier time than both b and c. Consequently on the time-of-flight spectrum, events b and c would be treated as neutrons of lower energy and the peak corresponding to this neutron group would be quite broad. In order to compensate for this anode time shift, the corresponding pulses from a dynode output are examined. A two parameter correlation between the anode (time) pulse and the dynode (amplitude) pulse is recorded to determine the time shift as a function of pulse amplitude. In this way a shift table is generated to be used in the TOFA routine. In this routine the flight time of each event is shifted the right amount to give a corrected time-of-flight spectrum according to the amplitude of the dynode pulses.

A monoenergetic source of neutrons from the reaction $T(d,n)^4\text{He}$ was used to generate a shift table for the polarimeter. The deuteron bombarding energy was 3 MeV and the polarimeter was set at 0° with respect to the direction of the incident deuterons, so that the neutron energy was 19.58 MeV. The time-of-flight system for the neutrons was set between the target and the polarimeter with a flight path of 2m. A block diagram of the electronics employed is shown in Fig. 2-6. The anode output from the RCA8575 photomultiplier tube was used as the start pulse while the Mobley magnet capacitor pick-off was used as the stop pulse for the time-of-flight system. The time-to-amplitude converter output was fed into ADC(A) after going through a delay line amplifier. The 11th dynode output from the photomultiplier was fed into a double delay line amplifier and then into

Fig. 2-6. An electronic block diagram for the generation of a shift table

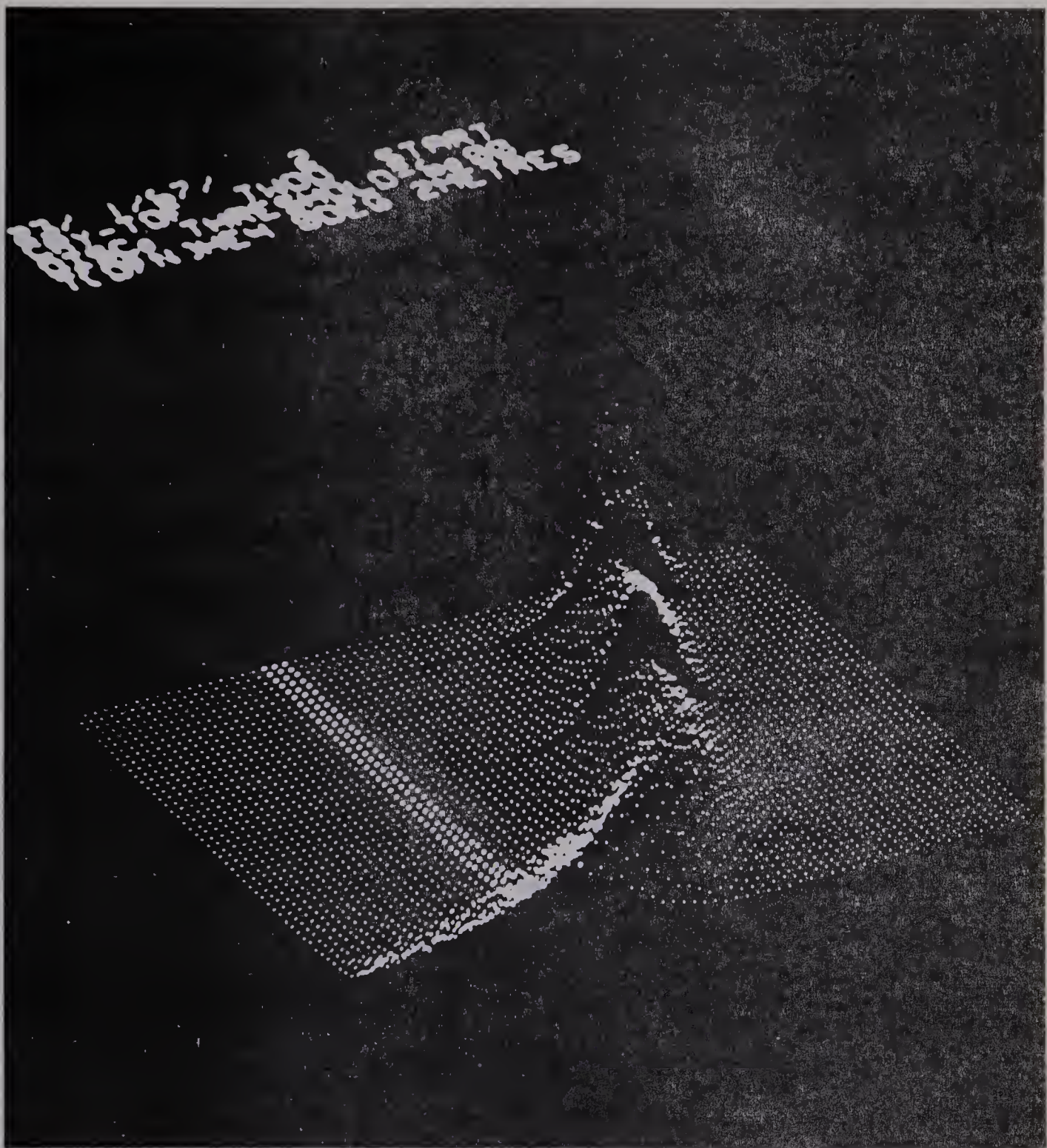


ADC(B). The double delay line amplifier output was also fed into a discriminator so that a lower threshold for the polarimeter could be set if desired. The discriminator output was then fed into a coincidence interrupt, which in turn was used to gate the two ADC's. The purpose of using the coincidence interrupt was to make sure that both ADC's and the computer would all accept or reject a particular event.

The range for ADC(B) was 1024 channels, and these 1024 channels were divided into 56 (amplitude) bins for the shift correction. Since a smaller pulse crosses the start discriminator threshold with a smaller slope than a larger one, the time spread is larger among the smaller amplitude group. For this reason the bin size for the lower bins was smaller than those for the upper bins, so that the time resolution of the neutron peak in the lower bins would not be too poor. Starting from bin 0, the first 32 bins were of 8 channels wide, the next 16 bins of 16 channels wide, and the next 8 bins of 64 channels wide. In this way the time-of-flight spectrum for this mono-energetic neutron group was divided into 56 bins. As can be seen from Fig. 2-7 which shows a picture of the TWOD spectrum taken directly from the display unit of the on-line computer system, the peak positions of the different bins shifted to lower channels with respect to the highest bin. Hence in constructing a shift table, the peak position of the highest bin was taken as the reference and the other peak positions were recorded with respect to this reference position. In order that all the peak positions would occur at the same channel as the highest bin, the time-of-flight spectrum in different bins was incremented by a number of channels equal to

Fig. 2-7. A picture of the TWOD spectrum taken directly from the display unit of the on-line computer system.

The time axis is along the X-axis with decrease in flight time along the positive direction of the X-axis. The amplitude axis is along the Y-axis.



the difference in peak positions between the reference peak and the peak in the bin. The shift table generated for the polarimeter is shown in Table 2-1 and a plot of this shift table is shown in Fig. 2-8. From the TWOD spectrum, the time resolution for the different bins was extracted. In Fig. 2-9, the time resolution has been converted from channels to nanoseconds and the bins have been converted into helium recoil energy (also see Table 2-1). The time resolution for helium recoil energy below 1 MeV was quite poor, while for the recoil energy range from 1 to 12 MeV, the time resolution improved gradually from about 2 ns to 1 ns. Fig. 2-10 shows a time-of-flight spectrum of the 19.58 MeV neutron group from the $T(d,n)^4\text{He}$ reaction. Without the anode time shift correction, the time resolution (FWHM) was 4.7 ns, while that with a time shift correction was 1.61 ns. The polarimeter threshold was set to accept pulses due to helium recoils of .5 MeV or higher in energy; this corresponds to an incident neutron energy of about 1 MeV. For best time resolution, it was found that the start discriminator had to be set just above the noise level of the phototube, unlike the case of a fast liquid scintillator, like NE213.

Since liquid helium also scintillates with γ -rays, the .511 γ from ^{22}Na was used to investigate the time resolution of the polarimeter for helium recoil energy below .5 MeV. A ^{22}Na γ -ray source was put between the polarimeter and a small NATON organic phosphor mounted on a Philips 56AVP phototube. The electronic arrangement was similar to that shown in Fig. 2-6 except that the anode signal from the 56 AVP was the source of the stop pulse instead of the Mobley capacitor pick-off and a narrow window was set

Table 2-1. Shift Table and Time Resolution for the Polarimeter

| Bin No. | Time Shift (Channels) | α -Recoil Energy (MeV) | Time Resolution (ns) |
|---------|--------------------------|----------------------------------|-------------------------|
| 0 | 62 | .049 | too wide |
| 1 | 57 | .147 | too wide |
| 2 | 52 | .245 | 4.36 |
| 3 | 47 | .343 | 4.18 |
| 4 | 42 | .441 | 3.90 |
| 5 | 39 | .538 | 3.45 |
| 6 | 35 | .636 | 2.91 |
| 7 | 33 | .734 | 2.63 |
| 8 | 31 | .832 | 2.27 |
| 9 | 30 | .930 | 2.09 |
| 10 | 29 | 1.028 | 2.09 |
| 11 | 27 | 1.126 | 1.91 |
| 12 | 27 | 1.224 | 1.82 |
| 13 | 25 | 1.322 | 1.82 |
| 14 | 25 | 1.420 | 1.54 |
| 15 | 24 | 1.517 | 1.63 |
| 16 | 23 | 1.615 | 1.63 |
| 17 | 23 | 1.713 | 1.54 |
| 18 | 23 | 1.811 | 1.45 |
| 19 | 22 | 1.909 | 1.45 |
| 20 | 21 | 2.007 | 1.45 |
| 21 | 21 | 2.105 | 1.54 |
| 22 | 20 | 2.203 | 1.36 |
| 23 | 20 | 2.301 | 1.54 |
| 24 | 19 | 2.399 | 1.27 |
| 25 | 19 | 2.496 | 1.45 |
| 26 | 19 | 2.594 | 1.18 |

Table 2-1 (continued)

| Bin No. | Time Shift (Channels) | α -Recoil Energy (MeV) | Time Resolution (ns) |
|---------|--------------------------|----------------------------------|-------------------------|
| 27 | 18 | 2.692 | 1.27 |
| 28 | 18 | 2.790 | 1.45 |
| 29 | 17 | 2.888 | 1.36 |
| 30 | 17 | 2.986 | 1.36 |
| 31 | 17 | 3.083 | 1.27 |
| 32 | 17 | 3.230 | 1.18 |
| 33 | 16 | 3.426 | 1.27 |
| 34 | 16 | 3.622 | 1.27 |
| 35 | 15 | 3.818 | 1.27 |
| 36 | 14 | 4.014 | 1.27 |
| 37 | 14 | 4.209 | 1.27 |
| 38 | 14 | 4.405 | 1.27 |
| 39 | 13 | 4.601 | 1.18 |
| 40 | 13 | 4.797 | 1.18 |
| 41 | 12 | 4.993 | 1.18 |
| 42 | 12 | 5.188 | 1.09 |
| 43 | 12 | 5.384 | 1.27 |
| 44 | 12 | 5.580 | 1.18 |
| 45 | 11 | 5.776 | 1.27 |
| 46 | 11 | 5.972 | 1.18 |
| 47 | 11 | 6.167 | 1.09 |
| 48 | 10 | 6.656 | 1.18 |
| 49 | 9 | 7.439 | 1.09 |
| 50 | 8 | 8.223 | 1.09 |
| 51 | 8 | 9.006 | 1.09 |
| 52 | 7 | 9.789 | 1.00 |
| 53 | 5 | 10.572 | 1.09 |
| 54 | 5 | 11.355 | 1.09 |
| 55 | 0 | 12.138 | 1.00 |

Fig. 2-8. Shift table

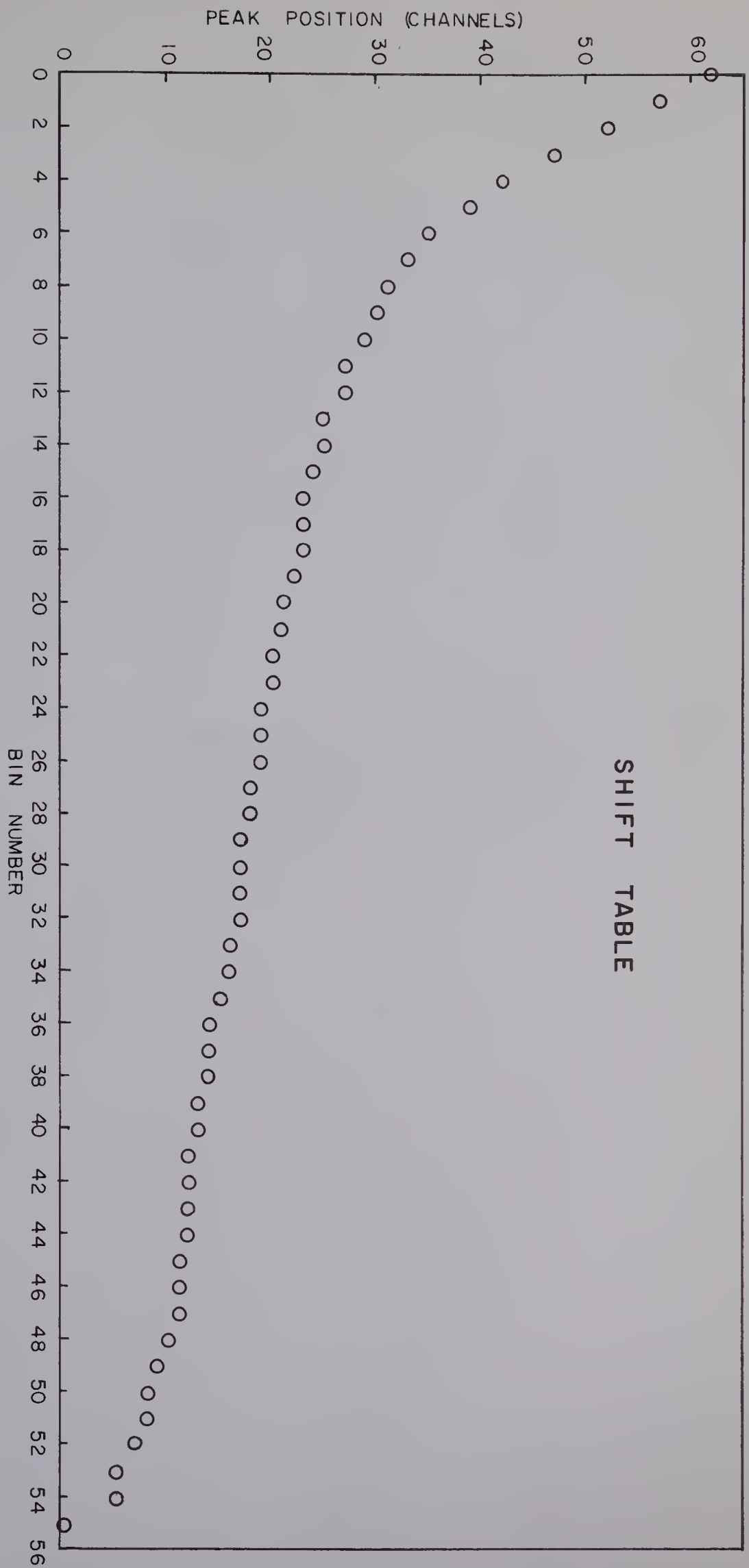


Fig. 2-9. Time resolution of the polarimeter against helium recoil energies, using the 19.58 MeV neutrons obtained from the $T(d,n)^4\text{He}$ reaction at $E_d = 3.0$ MeV and $\theta_n = 0^\circ$

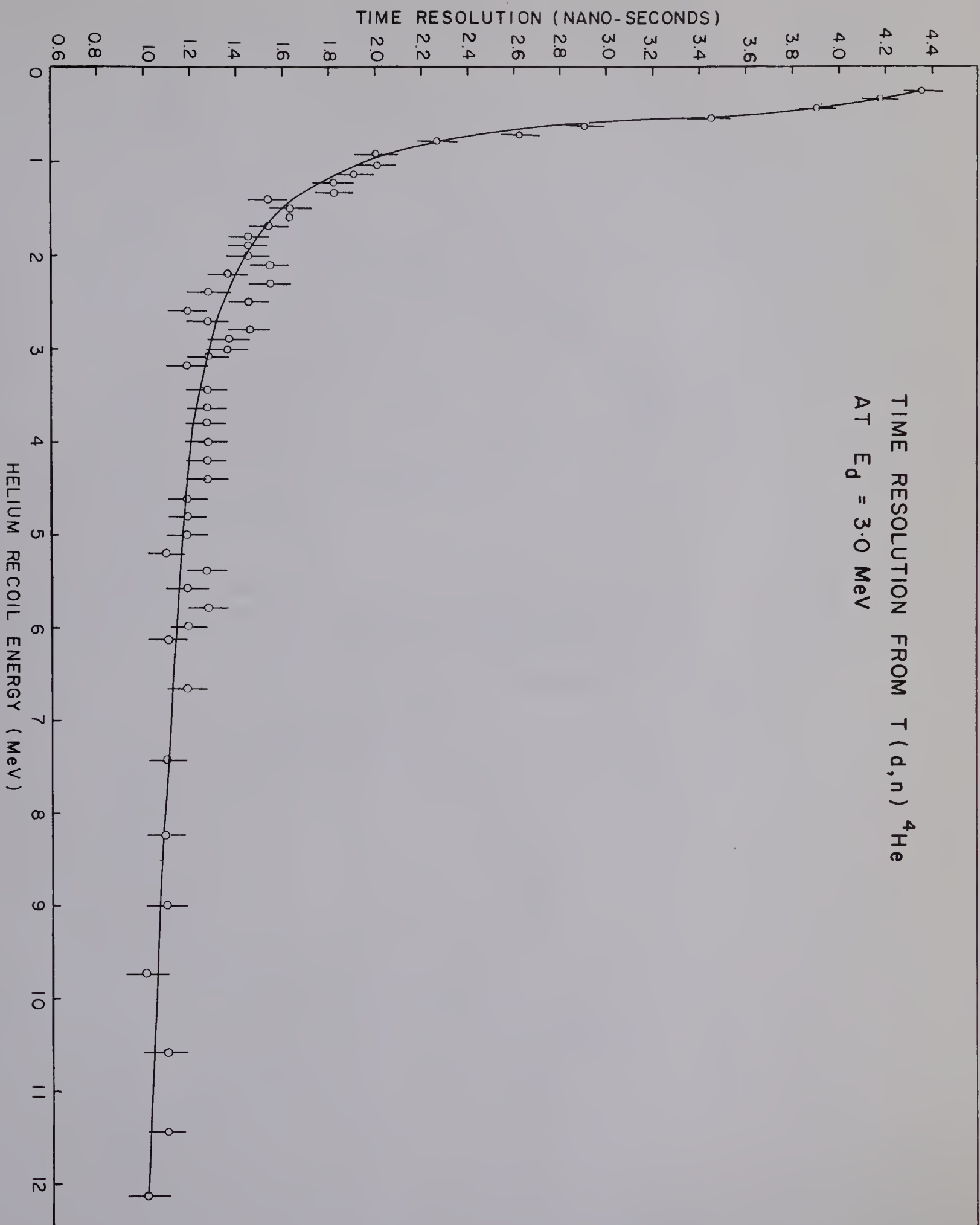
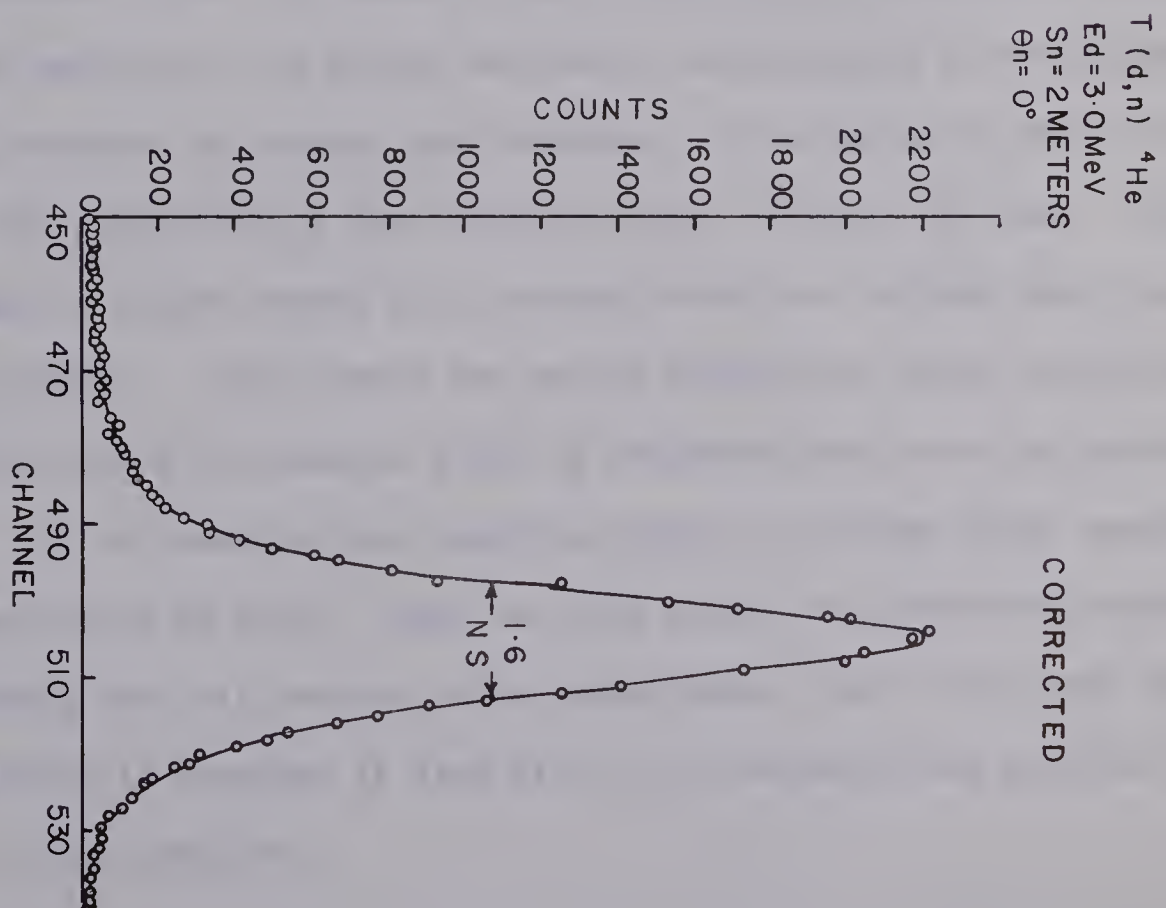
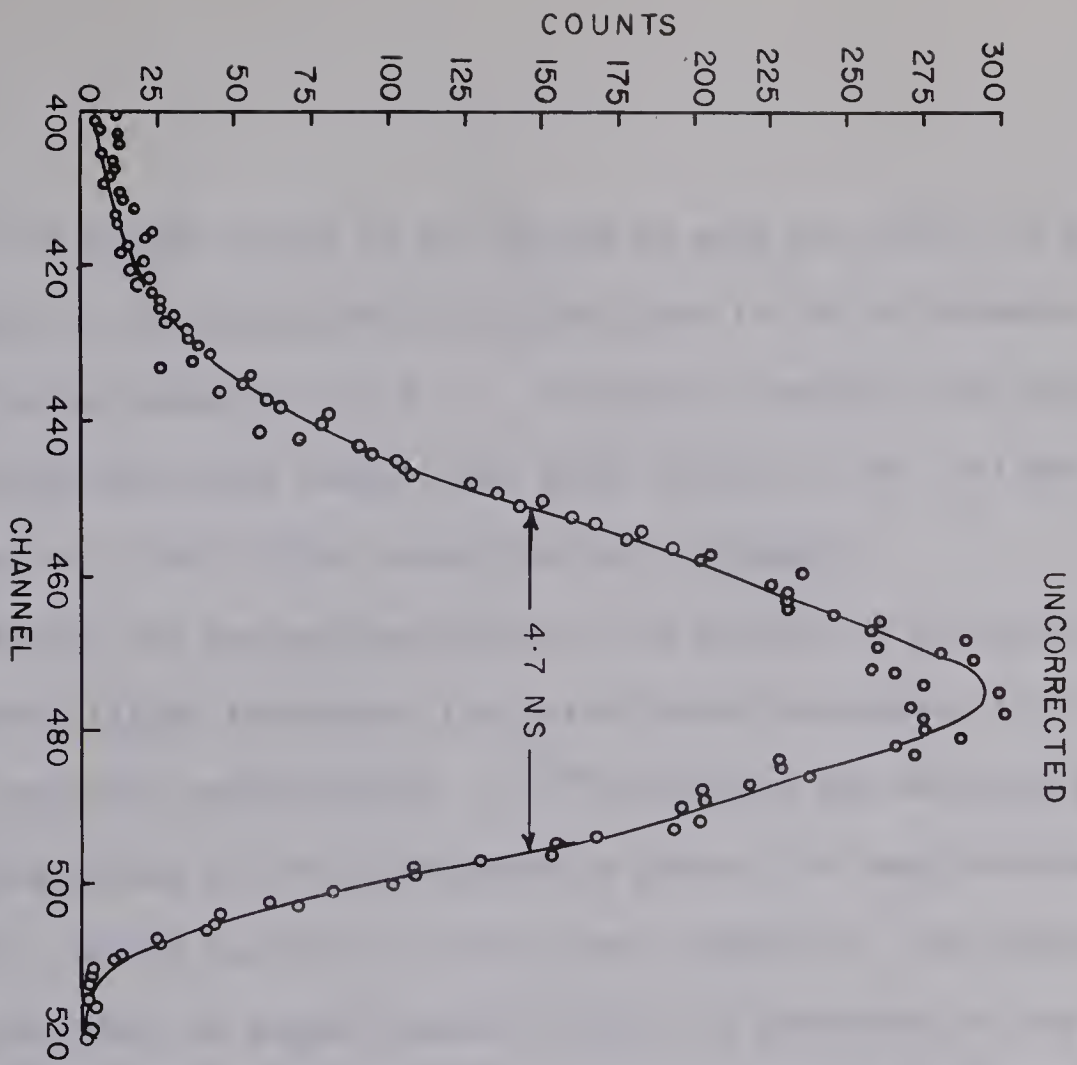


Fig. 2-10. Corrected and uncorrected neutron time-of-flight spectra from the $T(d,n)^4\text{He}$ reaction with $E_d = 3 \text{ MeV}$, $\theta_n = 0^\circ$ and a flight path of 2 metres.



on the 13th dynode output of the 56 AVP to gate the ADC's, so that the time resolution of the system would be mostly due to the polarimeter. The time resolution is shown in Fig. 2-11. In order to express the abscissa in terms of helium recoil energy, the pulse height of the .511 MeV γ -ray and that due to 5.1 MeV ^{239}Pu α -particles were compared.

Although the energy resolution of the system was achieved entirely by the time-of-flight technique, the pulse height resolution from a linear channel was also investigated. A ^{239}Pu α -source was introduced into the scattering volume of the polarimeter by means of a long stainless steel rod with a teflon section to reduce heat conduction. The energy resolution ($\Delta E/E$) was found to range between 25 and 35 % depending on the position of the α -source. Fig. 2-12 shows a plot of the energy resolution against the α -source position. The energy resolution deteriorated as the distance between α -source and window was increased. This indicates that the light collecting properties of the stainless steel cylinder are poor. Visually, the sapphire window seemed to be coated rather too thickly with the wavelength shifter. This affects the energy resolution, since considerable light from the scintillation event is reflected back into the scattering volume. It is possible that improving these two things might improve the time resolution as well. Since the only access to scattering volume is by unsoldering the tail section of the polarimeter, and it has been found to be difficult to resolder it leak tight, the reflector has not been changed since it was installed.

Fig. 2-11. Time resolution of the polarimeter using the .511 MeV γ -rays of ^{22}Na

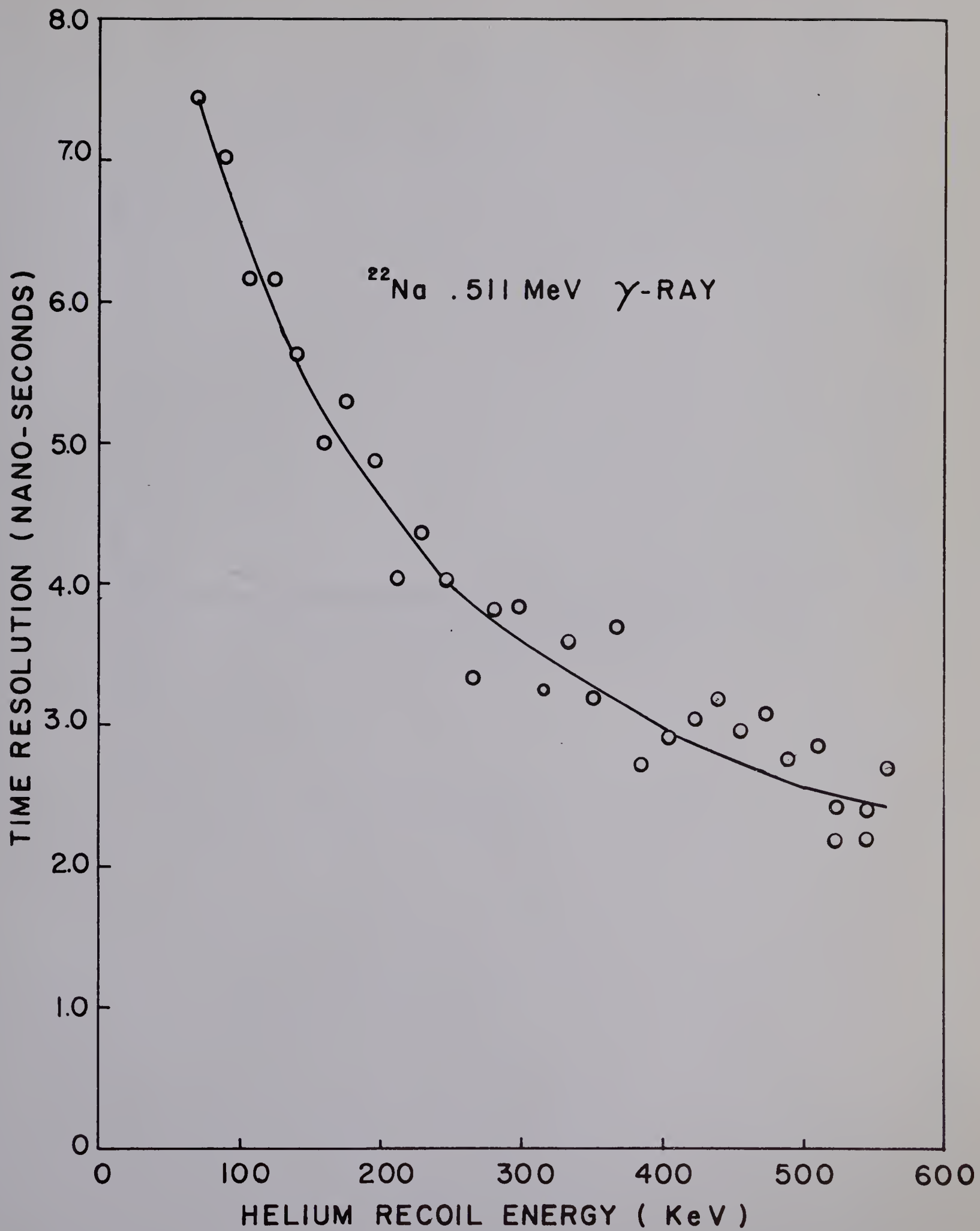
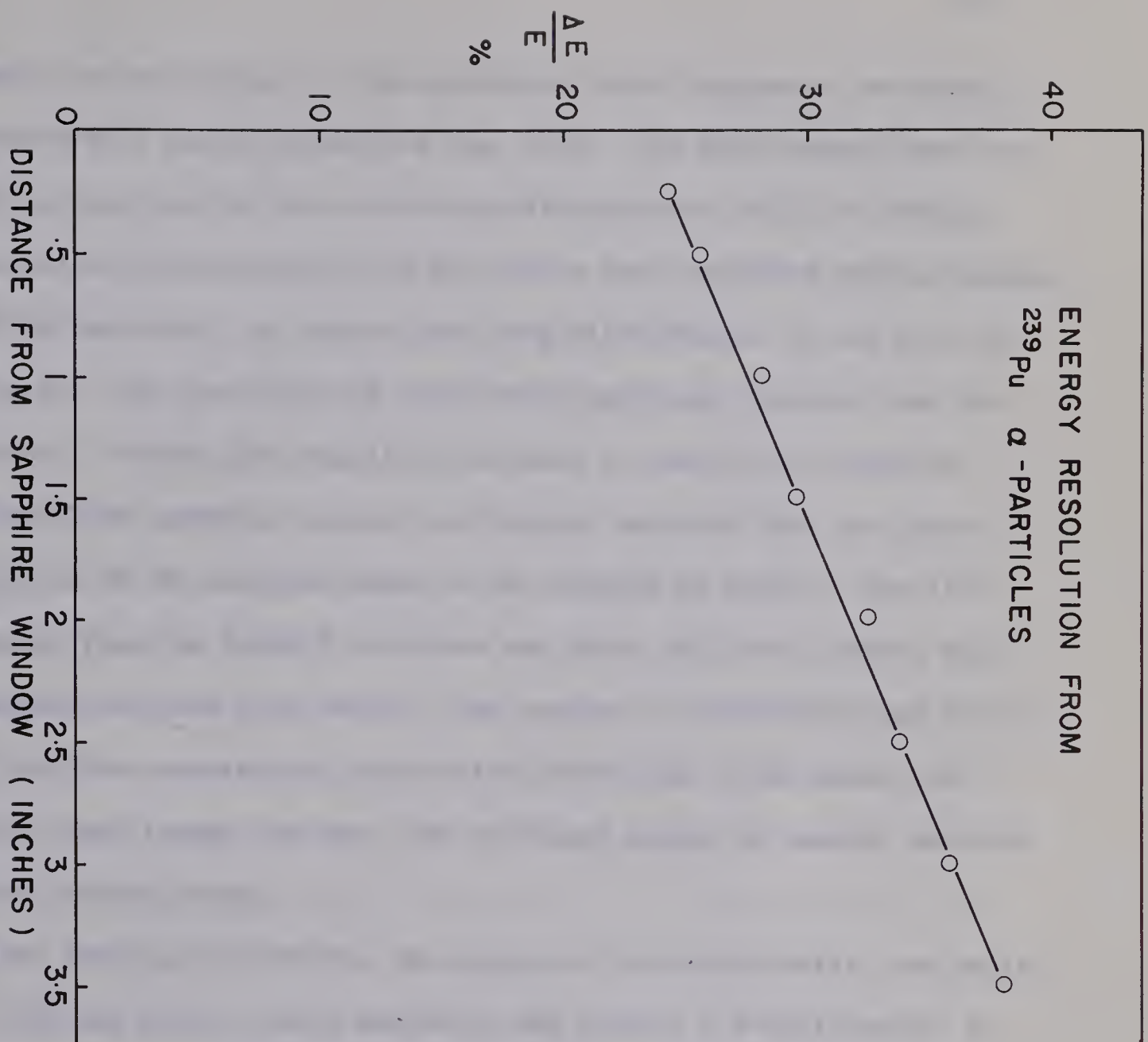


Fig. 2-12. Energy resolution of the polarimeter obtained from a linear channel against the position of a ^{239}Pu α -particle source



A detailed description of the electronic block diagram of the polarization system will now be given (see Fig. 2-3). The anode output from the RCA8575 phototube was fed into the start discriminator while the Mobley magnet capacitor pick-off was first fed into a fast amplifier system (Hewlett Packard 461A and 462A) and then to the stop discriminator of the time-of-flight system. The time range of the time-to-amplitude converter was 300 nano-seconds. A delay line amplifier was used to convert the negative time-to-amplitude converter output to a bipolar pulse so that the pulse shape would be of the required shape to be accepted by ADC(A). The 11th dynode output from the RCA8575 phototube was first fed into a double delay line amplifier and then into ADC(B). The outputs of both ADC(A) and ADC(B) were fed into the computer for the on-line correction of the anode time shift. All these formed the main time-of-flight system to resolve neutrons of different energy groups.

Besides feeding into ADC(B), the output of the double delay line amplifier was also fed into a linear amplifier and then to a discriminator, so that a neutron threshold could be set for the polarimeter. The purpose of using the linear amplifier was to achieve a lower threshold than that obtainable by feeding the double delay line amplifier output directly to the discriminator. The threshold set for the polarimeter corresponded to about 250 keV of helium recoil energy.

The electronic systems for the two neutron detectors were identical. The anode output of the XP1040 phototube was doubly RC differentiated, so that the amplitudes of the positive and the negative portions of the pulse

were about equal and of about 10 nanosecond width. The pulse was then inverted by a fast pulse transformer[†], so that the cross over of the pulse was used instead of the leading edge to trigger the start discriminator, since there was no anode time shift compensation done for the neutron detectors and using the cross over would result in a smaller anode time shift than using the leading edge. The stop signal for the fast coincidence was taken from the fast fan out of the polarimeter. The time-to-amplitude converter output was first fed into a delay line amplifier to obtain the correct pulse shape as required by the dual channel analyser. A window 50 nanoseconds wide was set to include all the neutron peaks and the γ -ray peak by means of the dual channel analyser, which also provided an adjacent upper window 50 nanoseconds wide to assess the time uncorrelated background. The 13th dynode output from the XP1040 was first fed into a double delay line amplifier and then to a discriminator so that the threshold of the two neutron detectors could be matched.

Four 3-fold coincidence units were used, so that the true and the random time-of-flight spectra for the neutrons scattered to the left and the right could be recorded all at one time. To 3-fold coincidence unit A, the discriminator output for setting the threshold of the polarimeter, the true fast coincidence for neutrons scattered to the right^{††} and the

[†]E H Research Laboratory, Inc. ZT9-9X pulse transformer

^{††}Since the Basel sign convention is used, the detector on the left hand side of the page is actually the right detector according to the sign convention.

discriminator output for setting a threshold for the right neutron detector were fed. For 3-fold coincidence unit B, two of the inputs were the same as in unit A and the third one was from the random fast coincidence windows for the right detector. 3-fold coincidence units C and D played the same roles for the left neutron detector. The outputs of the four 3-fold coincidence units were used to route ADC(A), so that the first and the second 1024 channels would correspond to the true and random time-of-flight spectra of neutrons scattered to the right, while the third and the fourth 1024 channels would correspond to the respective spectra of neutrons scattered to the left. Fig. 2-13 shows a picture of the four time-of-flight spectra taken directly from the computer display unit for the reaction $^{28}\text{Si}(d,n)^{29}\text{P}$.

2-4 False Asymmetry

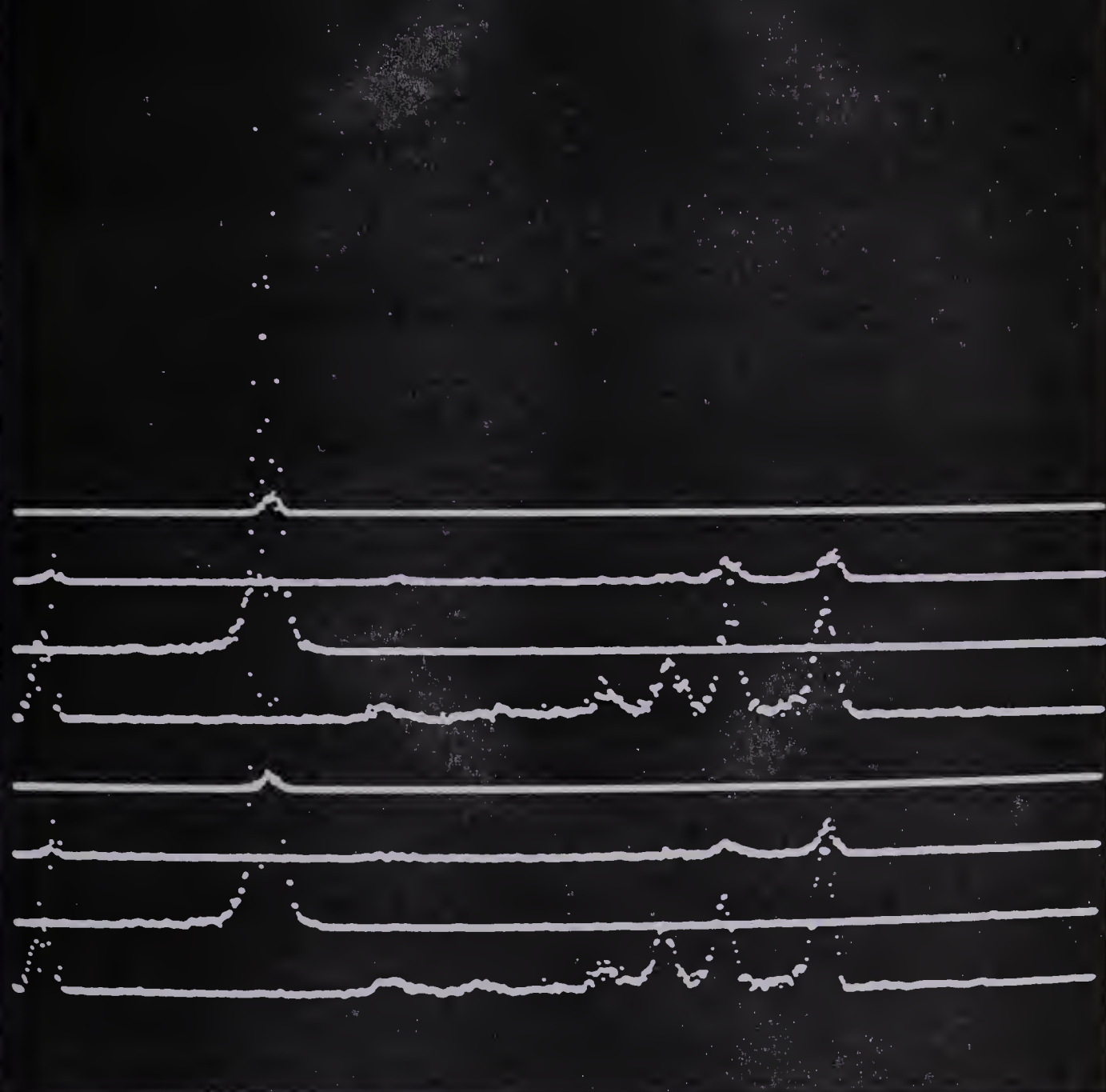
As the polarization of the neutrons from a reaction is measured in terms of the counts recorded by the right and the left detectors, any false asymmetry due to defects in the system would result in wrong values for the polarization. The two main sources of false asymmetry are called geometric asymmetry and electronic asymmetry. A thorough discussion on this subject was given by Haeberli in Chapter V.G. of Fast Neutron Physics, Part II, and the discussion below will be entirely concerned with the elimination of false asymmetry in our system.

Fig. 2-13. A picture of the $^{28}\text{Si}(\text{d},\text{n})^{29}\text{P}$ neutron time-of-flight spectra taken directly from the display unit of the on-line computer system.

The picture shows the four 1024 channels corresponding to the true and random time-of-flight spectra of neutrons scattered to the right and the left by the polarimeter.

See Fig. 5-2 on page 70 for the identification of the different peaks.

1926 12 26 9 55 AM 60000



(a) Geometrical Alignment

The whole assembly of the polarimeter, the two neutron detectors and the two lead shadow bars was mounted on a channel ironsteel cart (see Fig. 2-2 and Fig. A2-2). The centre about which the two neutron detectors were rotated was adjusted so that it was vertically below the centre of the scattering volume of the polarimeter. This was achieved by viewing the centre of the scattering volume by two transits set at about 90° apart. Adjustments were made on the position of the polarimeter until the two centres were in the same vertical line when the transits were tilted up and down to view the two centres.

In order to find the zero degree position of the polarimeter with respect to the incident beam of deuterons, an angular distribution of the neutrons from the $D(d,n)^3\text{He}$ reaction was measured from -20° to $+20^\circ$ at 5 MeV bombarding energy. Since the neutron angular distribution peaks very strongly at 0° , the 0° position for the polarimeter was determined accurately from the peak of the angular distribution. The 0° position was found to reproduce with $\pm 1^\circ$.

(b) Electronic Alignment

The .511 and the 1.28 MeV γ -rays from ^{22}Na were used to set the thresholds and gains of the two neutron detectors.

Fig. 2-14 shows a block diagram of the electronics. The shape of the γ -ray spectrum is shown in Fig. 2-15.

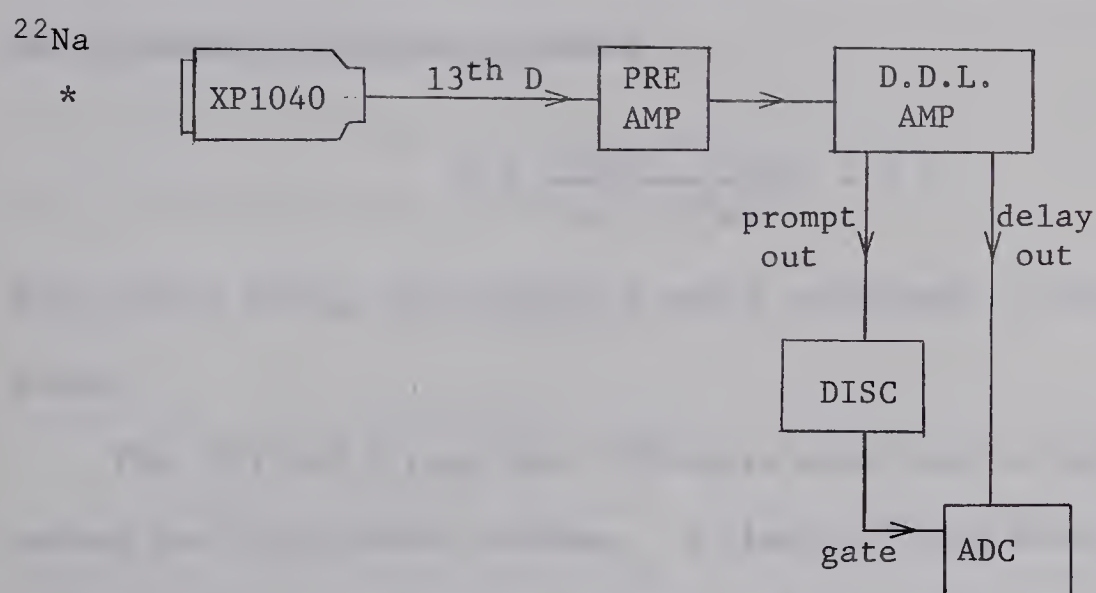


Fig. 2-14. A block diagram for setting the threshold of the neutron detectors.

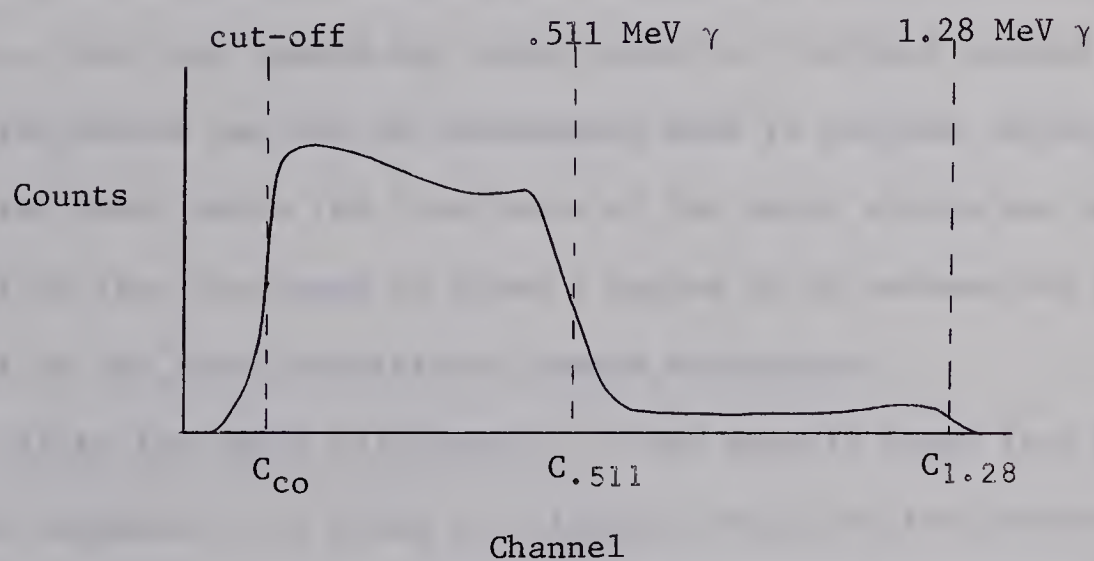


Fig. 2-15. ^{22}Na γ -ray spectrum

The discriminator level was adjusted to obtain the value of C_{co} so that the following ratio was obtained

$$R = \frac{C_{1.28} - C_{.511}}{C_{.511} - C_{co}} = 3.2$$

With such a ratio, the threshold would correspond to about .5 MeV of neutron energy.

The .511 MeV γ -rays from ^{22}Na were also used in setting up the 50 nanosecond fast coincidence windows. A time-of-flight spectrum was recorded by putting the γ -ray source between the polarimeter and one of the neutron detectors. The peak corresponding to the .511 MeV γ -rays gives essentially zero time, since γ -rays travel much faster than any neutron group of interest. Since the distance between the polarimeter and the neutron detector was only 25 cm, the time-of-flight spectrum for neutrons of a few MeV overlapped with γ -ray peak. For this reason the lower window of the dual channel analyser for the true events was set 50 nanoseconds wide to include the upper tail of the γ -ray peak, while the lower edge of the upper window was set at the upper tail of the γ -ray peak to cover a region of 50 nanoseconds for the assessment of the time uncorrelated random background.

Even after the above adjustments, it was usually found that there was some false asymmetry. In order to eliminate this, the two neutron detectors and the electronics associated with each of them were interchanged in their left and right positions. The underlying principle is illustrated in the following paragraph.

Suppose the two neutron detectors are marked A and B. Let R and L be the numbers of neutrons scattered to the right and the left by the polarimeter and detected by the right and the left detectors respectively, then ideally the right-left ratio, r , is

$$r = R/L .$$

If, however, the efficiencies, which are affected by both the detector threshold and the fast coincidence window, of the detectors are not exactly the same, R/L is not equal to r . Let the number of neutrons detected by detector A when situated at right be R_A and that by detector B situated at left be L_B , then instead of the true right-left ratio, one measures

$$R_A/L_B = r\delta$$

where δ is due to the difference in efficiencies. If now the two detectors are interchanged in their positions, the counts recorded by them will be R_B and L_A and we have

$$R_B/L_A = r/\delta .$$

Hence the true right-left ratio is obtained if the geometrical mean of the observed right-left ratios is taken, i.e.

$$r = \sqrt{\frac{R_A}{L_B} \cdot \frac{R_B}{L_A}}$$

This is a very powerful way of eliminating not only the electronic asymmetry, but also the false asymmetry due to the two detectors not being placed with

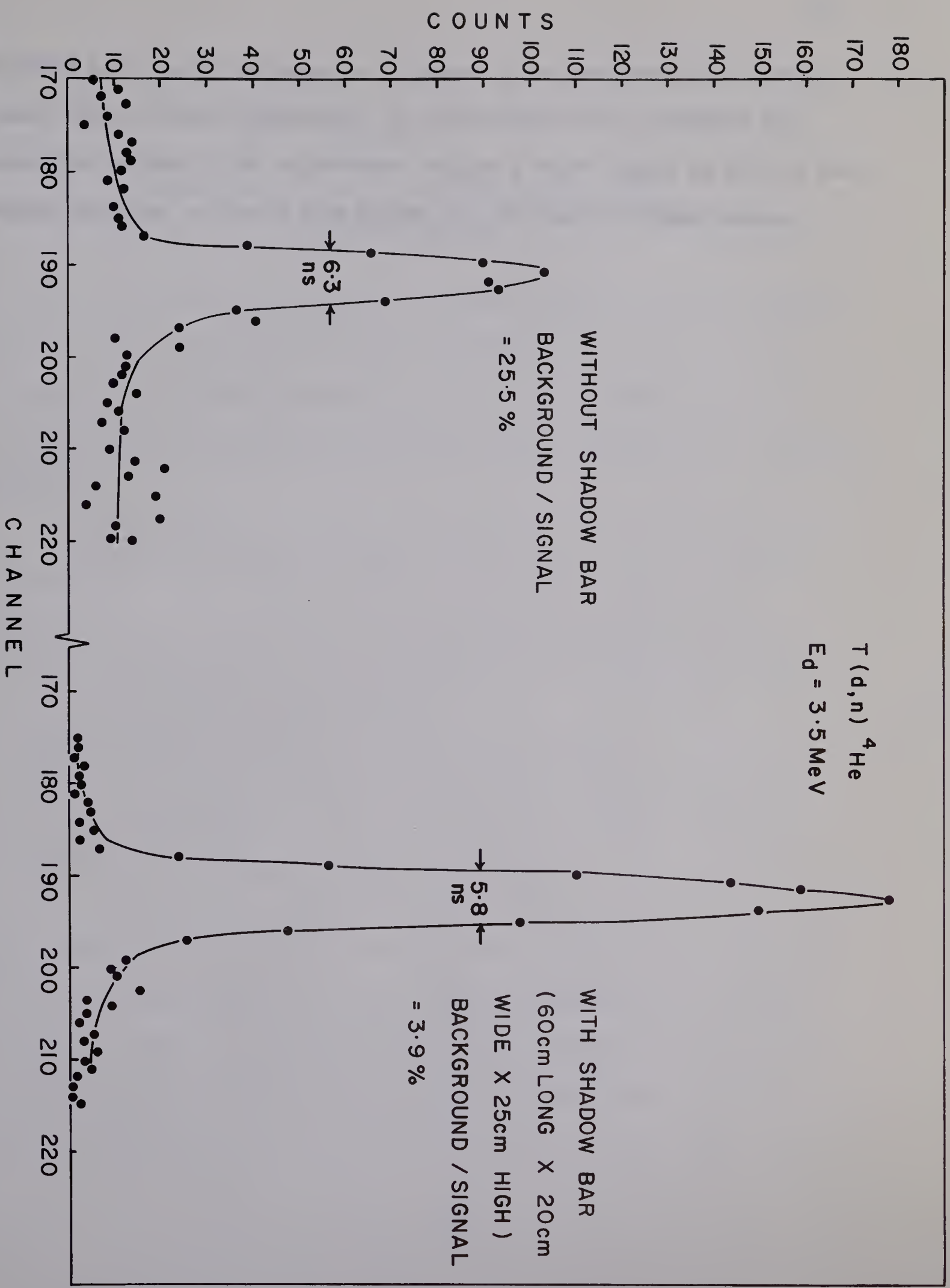
perfect symmetry about the polarimeter, provided the right and the left positions of the detectors remain fixed.

Instead of changing the two detectors, the same effect is attained if the polarimeter angle is changed from θ to $-\theta$, since the two detectors change role according to the sign convention. For θ equal or less than 20° , measurements were done in this way instead of moving the detectors. Measurements from both methods agreed to within 2 % in most cases.

2-5 The Effectiveness of the Shadow Bars

In order to investigate the effectiveness of the lead shadow bars (60 cm long by 20 cm wide by 25 cm high), neutrons from the reaction $T(d,n)^4\text{He}$ at a deuteron bombarding energy of 3.5 MeV were used. The polarimeter was set at 0° with respect to the direction of the incident beam of deuterons and at a distance of 1.5 metres away from the target. A time-of-flight spectrum was recorded between the polarimeter and one of the neutron detectors, which was set at 90° with respect to the direction of the incident neutrons and at a distance of 55 cm away from the polarimeter. Time-of-flight spectra for neutrons with and without the shadow bar are shown in Fig. 2-15. Without the shadow bar the background to signal ratio was found to be 25.5 %, while with the shadow bar between the target and the neutron detector, this ratio was reduced to 3.9 %. It was also noticed that in the presence of the shadow bar, the width of the peak (FWHM) improved from 6.3 to 5.8 nanoseconds. It should be mentioned that there was no anode time shift compensation for the time-of-flight system and the time uncertainty at which the neutrons were

Fig. 2-16. Time-flight-spectra to show the effectiveness of the shadow bars



detected was roughly increased by a factor of two over that of a conventional time-of-flight experiment, as the neutrons had to traverse the scattering volume of the polarimeter to give a start signal as well as the neutron detector to give a stop signal for the time-of-flight system.

CHAPTER III

CALIBRATION OF THE POLARIZATION SYSTEM WITH
D(d,n) ^3He NEUTRONS

The study of the polarization of neutrons from the D(d,n) ^3He reaction has long been of interest. Blin-Stoyle (Bl 51) analysed the reaction by the method of partial waves and arrived at the following expression for the prediction of polarization for the outgoing particles in a nuclear reaction:

$$P(\theta)\sigma(\theta) = \sum_{L=1}^{L_{\max}} A_L P_L^{(1)}(\cos\theta) \quad (3-1)$$

where $P(\theta)$ = polarization of the outgoing particles emitted at an angle θ

$\sigma(\theta)$ = differential cross section

L_{\max} = highest partial wave used in the reaction

A_L = a coefficient depending on the matrix elements describing the reaction

and $P_L^{(1)}(\cos\theta)$ = associated Legendre polynomial.

If the largest effective values of the incident orbital angular momentum, final orbit angular momentum and total angular momentum are ℓ , ℓ' and J , then L_{\max} in equation (3-1) must be less than or equal to 2ℓ , $2\ell'$ and $2J$. In addition, if the interfering states have the same parity, all the L -values must be even.

In the $D(d,n)^3\text{He}$ reaction, since both the incident particles and the target nuclei are identical and only even L-values contribute, equation (3-1) can be written as:

$$P(\theta)\sigma(\theta) = \sum_n a_n \sin(2n\theta) \quad (3-2)$$

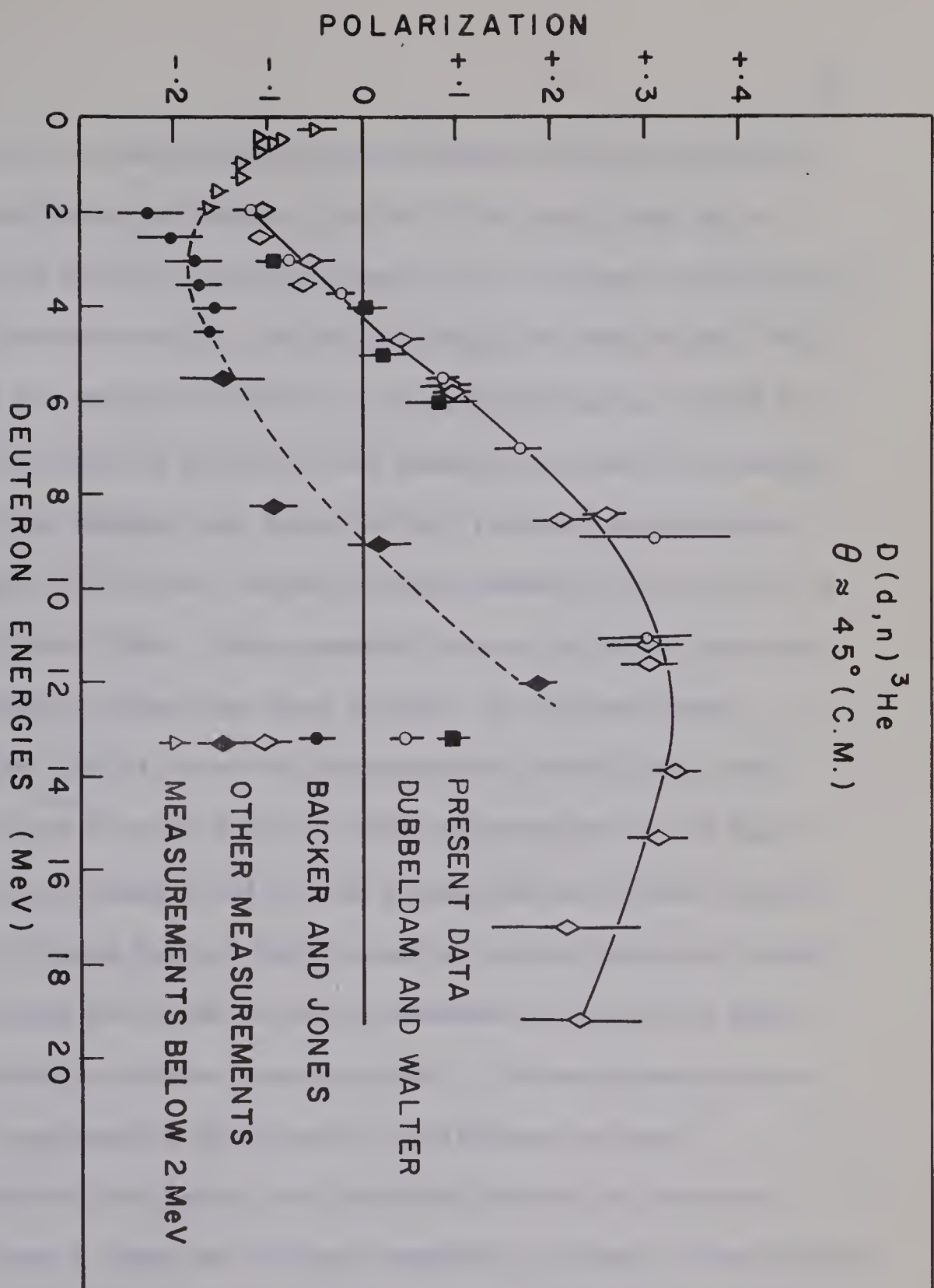
The determination of the coefficients a_n gives the strength of the spin-orbit coupling in the reaction. Apart from the determination of these coefficients, polarization experiments have been performed to investigate the possibility of using this mono-energetic neutron source as a polarized neutron source.

In 1961 Dubbeldam and Walter (Du 61) made a survey of the polarization measurements from this reaction. As seen from equation (3-2), $P(\theta)\sigma(\theta)$ is largest for $\theta = 45^\circ(\text{c.m.})$. For this reason most of the polarization measurements were performed near this angle. Dubbeldam and Walter found that for deuteron energies above 2 MeV their measurements at $45^\circ(\text{c.m.})$ were in disagreement with the previous measurements around this angle. Since that time, more data have been obtained in different laboratories. In 1965 Purser, Sawers and Walter (Pu 65) made another survey of the situation. A summary of their survey is given in the next paragraph.

Fig. 3-1 presents the results of most of the polarization measurements of neutrons from the $D(d,n)^3\text{He}$ reaction around $45^\circ(\text{c.m.})$. Below deuteron energies of 2 MeV, all measurements agree quite well (Me 54, Le 57, Pa 58), while above 2 MeV, the measurements separate into two

Fig. 3-1 Polarization measurements of neutrons from the $D(d,n)^3\text{He}$ reaction around $45^\circ(\text{c.m.})$.
(Pu 65)

$D(d,n)^3\text{He}$
 $\theta \approx 45^\circ (\text{C.M.})$



groups. The first reported polarization measurement for this reaction above 2 MeV was performed by Daehnick (Da 59). He found that for a deuteron energy of 8.2 MeV, at reaction angles $\theta = 47^\circ(\text{c.m.})$ and $59^\circ(\text{c.m.})$, the polarization was near -0.10. By extrapolating the data below 2 MeV, he predicted that for angles near $55^\circ(\text{c.m.})$ the polarization from 2 to 8 MeV was negative, small in amplitude and smoothly varying with energy. In the following year Baicker and Jones (Ba 60B) reported measurements at a reaction angle of $40^\circ(\text{lab})$, which is approximately $55^\circ(\text{c.m.})$ for an energy range of 2 to 4.5 MeV. Their results lie on the curve predicted by Daehnick (hereafter called the lower curve). In the next year Dubbeldam and Walter (Du 61) reported measurements at $45^\circ(\text{c.m.})$ over an energy range from 1.9 to 11.0 MeV. Their measurements do not agree with the previous measurements and lie on a curve which is also a smooth extrapolation of the data below 2 MeV (hereafter called the upper curve). Measurements have been performed in other laboratories near this angle and support for either curve has been reported. The measurements above 2 MeV in Fig. 3-1 are results obtained by 14 different groups.

Since both Baicker and Jones, and Dubbeldam and Walter measured the polarization over a range of deuteron energies, a closer investigation of the difference of the two sets of measurements was carried out by Purser, Sawers and Walter (Pu 65). They used a system similar to the one used by Dubbeldam and Walter and measured the neutron polarization at a reaction angle of $45^\circ(\text{c.m.})$ over a deuteron energy range of 1.9 to 3.7 MeV. Their data are in good agreement with the upper curve. Since Baicker and

Jones measured the neutron polarization at $40^\circ(\text{lab})$, Purser, Sawers and Walter measured the polarization at this angle to see if the difference in angles would account for the discrepancy. Their measurements at this angle are slightly more negative than their own measurements at $45^\circ(\text{c.m.})$, and statistically are still in better agreement with the upper curve.

In order to explain the discrepancy between these two sets of measurements, a comparison of the experimental arrangements employed by both groups will be discussed. In both cases, a deuterium gas target was used. Baicker and Jones used a liquid helium polarimeter and a neutron time-of-flight spectrometer set between the target and the neutron detector. The time resolution ranged from 5 to 10 nano-seconds. Scintillations in the helium scattering volume were not used to require a coincidence with the neutron detector in order to reduce the random background. The background reported in their case ranged from 40 to 60% of the total counts. Also, only one neutron detector was used, with a closed geometry shielding consisting of a combination of iron, lead, paraffin and boric acid between the target and the polarimeter and around the neutron detector. Because of the large bulk of the shielding materials, no monitor detector was used and the counts when the neutron detector was placed in the right and left positions were normalized to the total charge collected at the target.

Dubbeldem and Walter, on the other hand, employed a gas scatterer of 54 atmospheres of helium and 5 atmospheres of xenon. The energy resolution as obtained from the helium recoil scintillation signals was 8% for

polonium α -particles. A fast and slow coincidence was set between the polarimeter and each of the side neutron detectors. The background reported in most cases was not more than 20%. A solenoid was used to change the orientation of the neutron spins instead of moving the detectors in the elimination of false asymmetry. Open geometry shielding was employed in this case. The only shielding material in front of the target was a brass collimator for the outgoing neutrons aside from the solenoid.

In comparing the two systems, the most significant point is that the background in the system employed by Baicker and Jones was about three times as high as in the system employed by Dubbeldam and Walter. Since the background was so high, an over estimation of the background in the experiment of Baicker and Jones could result in the magnitude of the neutron polarization being too large. If this were the case, the set of measurements obtained by Baicker and Jones would be more negative than those of Dubbeldam and Walter. As the measurements of Baicker and Jones are more negative than those of Dubbeldam and Walter, their discrepancy can be explained on account of the high background of the system employed by Baicker and Jones. In the deuteron energy range of 4 to 9 MeV, the polarization measurements on the lower and upper curves are opposite in sign, so there must be a serious systematic difference in the systems employed by the different groups in this energy range to obtain measurements opposite in sign.

In spite of the discrepancy in the neutron polarization measurements in the $D(d,n)^3\text{He}$ reaction, this reaction was chosen as a calibration of our

system, because this is the reaction on which most polarization measurements have been performed. Since we also wanted to investigate the discrepancy, the polarization of the neutrons from the reaction was measured at 45° (c.m.) and at deuteron energies of 3.0, 4.0, 5.0, and 6.0 MeV.

A solid target[†] (1" diameter) was used in this experiment. It was a thin layer of zirconium ($\approx 500 \mu\text{g}/\text{cm}^2$) deposited on a tungsten backing. The deuterium was absorbed in the zirconium layer.

In order to have an unbiased estimate of the total number of counts under a neutron time-of-flight peak, a computer program^{††} written by J. T. Tepel (Te 66) was used. Since a Gaussian distribution is not always the correct shape in defining a peak obtained from an experiment, this program allows the input of any desired reference peak shape. The reference peak is defined by a discrete set of (x,y) co-ordinates and scaling is adjusted by the program to fit peaks (or overlapping peaks) of different heights. This program also gives an assessment of the time dependent background under the peaks of the spectrum. Linear and quadractic functions are provided for background fitting.

Our measurements of the polarization of neutrons from the $\text{D(d,n)}^3\text{He}$ reaction at a reaction angle, θ , of 45° (c.m.) and at deuteron bombarding

[†] Isotope Target Centre, Oak Ridge National Laboratory, Oak Ridge, Tennessee.

^{††} Adapted to run with the IBM 7040 computer at the University of Alberta by T. B. Grandy and D. A. Gedcke.

energies of 3.0, 4.0, 5.0, and 6.0 MeV are shown in Fig. 3-1, as well as many other measurements. They agree well with the measurements by Dubbeldam and Walter (Du 61) and clearly support the measurements lying on the upper curve. Our results are also tabulated in Table 3-1 together with the background estimation at different deuteron energies. The increase in background with increase in deuteron energy is due to deuteron disassociation.

Table 3-1. Neutron Polarization Measurements from the $D(d,n)^3\text{He}$ Reaction at $\theta = 45^\circ$ (c.m.)

| E_d (MeV) | $\langle P_2 \cos\phi \rangle$ | Polarization | Background |
|-------------|--------------------------------|--------------------|------------|
| 3.0 | .9589 | $-(.091 \pm .026)$ | 1.3% |
| 4.0 | .9437 | $+(.004 \pm .020)$ | 2.7% |
| 5.0 | .9336 | $+(.023 \pm .021)$ | 3.5% |
| 6.0 | .9313 | $+(.083 \pm .038)$ | 5.4% |

NOTE: $\langle P_2 \cos\phi \rangle$ is the average value of $P_2 \cos\phi$, taking into account the finite geometry of the polarimeter and the neutron detectors.

CHAPTER IV

POLARIZATION PREDICTIONS FROM DIRECT REACTION THEORY

Two extreme models are usually employed to explain the mechanism of a nuclear reaction. The direct reaction mechanism depicts the transition from the incident to the exit channel to take place in one step without the formation of an intermediate state. Also only a few degrees of freedom are employed in the description of the colliding systems. This is in contrast with the compound nuclear process, which assumes the reaction to take place in two steps. The incident particle is first captured by the target nucleus to form an intermediate compound nuclear state, which then disintegrates to yield the reaction products. The distorted wave Born approximation (DWBA) has been most commonly used in the direct reaction calculation and many articles have been written on this aspect. The description of the theory in this chapter is based on the articles written by W. Tobocman (To 61), N. Austern (Au 63), G. R. Satchler (Sa 64, Sa 65) and R. H. Bassel (Ba 64).

The DWBA theory of a nuclear reaction $A(a,b)B$ is based on the assumption that elastic scattering between a and A in the incident channel and b and B in the exit channel predominates over the reaction amplitude. Hence the reaction can be treated by perturbation theory and the transition amplitude is given by

$$T = \int d\vec{r}_a \int d\vec{r}_b \chi_b^{(-)*}(\vec{k}_b, \vec{r}_b) \langle B, b | V_{int} | A, a \rangle \chi_a^{(+)}(\vec{k}_a, \vec{r}_a) \quad (4.1)$$

In equation (4.1), V_{int} is the interaction potential responsible for the transition. \vec{r}_a is the displacement of a from A, and \vec{r}_b the displacement of b from B, while J is the Jacobian of the transformation to these relative coordinates. The functions χ_a and χ_b are the distorted waves, which describe the relative motion of the pair a, A (asymptotically with relative momentum \vec{k}_a) before the collision, and of the pair b, B (with \vec{k}_b) after the collision. The superscript (+) or (-) denotes the outgoing - or incoming - wave boundary conditions. If the particles a and b have spins \vec{s}_a and \vec{s}_b , and the target and residual nuclear spins are \vec{J}_A AND \vec{J}_B , respectively, we define:

$$\begin{aligned}\vec{J} &= \vec{J}_B - \vec{J}_A \\ \vec{s} &= \vec{s}_a - \vec{s}_b \\ \text{and} \quad \vec{L} &= \vec{J} - \vec{s}\end{aligned}$$

A partial wave expansion is used to describe the distorted waves χ . In the presence of spin-orbit coupling, they can be written as:

$$\begin{aligned}\chi_{m'm}^{(+)}(\vec{k}, \vec{r}) &= (4\pi/kr) \sum_{JLM} \langle L, s, M, m | J, M+m \rangle \langle L, s, M+m-m', m' | J, M+m \rangle \\ &\times i^L \chi_{LJ}(k, r) Y_L^{M*}(\theta_k, \phi_k) Y_L^{M+m-m'}(\theta_r, \phi_r) \quad (4.2)\end{aligned}$$

The resultant angular momentum, $\vec{J} = \vec{L} + \vec{s}$, and its z-component (M+m) are conserved during scattering by the spin-orbit potential, whereas the individual z-components of \vec{L} and \vec{s} are not. (Note that the spin \vec{s} used in the distorted waves is either \vec{s}_a or \vec{s}_b and should not be confused with the

spin \vec{s} of the captured particle as defined previously.) The terms for which $m \neq m'$ allow for spin-flips in the reaction. The partial waves, χ_{LJ} , are solutions of the Schrödinger equation:

$$[d^2/dr^2 + k^2 - L(L+1)/r^2 - (2\mu/h^2)U(r)] \chi_{LJ}(k,r) = 0 \quad (4.3)$$

where $U(r)$ represents the optical potentials. For large r , beyond the range of nuclear potentials, these radial waves have the form:

$$\chi_{LJ}(k,r) = \frac{1}{2} i [H_L^*(kr) - \eta_L^J H_L(kr)] \exp(i\sigma_L) \quad (4.4)$$

where $H_L = G_L + iF_L$, and G_L and F_L are the regular and irregular functions. σ_L is the Coulomb phase shift and η_L^J is the scattering matrix element for the (L,J) partial wave. The η_L^J is computed by numerical integration of equation (4.3) and then matching the logarithmic derivative of the wave function to that of equation (4.4) at a distance, r , outside the nuclear field.

The optical model potentials are usually expressed as:

$$U(r) = V_{\text{coul}}(r) - V f_1(r) - iW f_2(r) - V_{\text{so}} f_3(r) \quad (4.5)$$

$V_{\text{coul}}(r)$ is the Coulomb potential. Assuming that a and b are point charges (ze) and A and B are uniformly charged spheres ($z'e$), it is given by:

$$\begin{aligned} V_{\text{coul}}(r) &= \frac{zz'e^2}{r} & r > R_c \\ &= \frac{zz'e^2}{2R_c} (3 - r^2/R_c^2) & r \leq R_c \end{aligned} \quad (4.6)$$

where R_C is the charge radius of the nucleus and is given by $r_{\text{coul}} A^{1/3}$.
 A is the mass number of the nucleus.

V , W and V_{so} are the real, imaginary and spin-orbit well-depth parameters respectively. Quite a variety of shapes has been used for the radial functions f_1 , f_2 , f_3 though the Saxon-Woods form has been most commonly used. They are:

$$f_1(r) = \frac{1}{1 + \exp\left(\frac{r-R_R}{\alpha_R}\right)} \quad (4.7)$$

$$f_2(r) = \frac{d}{dr} \left[\frac{4\alpha_I}{1 + \exp\left(\frac{r-R_I}{\alpha_I}\right)} \right] \quad (4.8)$$

$$f_3(r) = - \left(\frac{\hbar}{m_\pi c}\right)^2 \frac{1}{r} \frac{d}{dr} [f_1(r)] \vec{\ell} \cdot \vec{s} \quad (4.9)$$

where $R_R = r_R A^{1/3}$

and $R_I = r_I A^{1/3}$

Let us now consider the nuclear matrix element responsible for the reaction. It can be written as:

$$\begin{aligned} J \langle B, b | V_{\text{int}} | A, a \rangle &= J \langle J_B^{M_B}, s_b^{m_b} | V_{\text{int}} | J_A^{M_A}, s_a^{m_a} \rangle \\ &= \sum_{\ell s j} i^{-\ell} G_{\ell s j, m}(r_b, r_a; bB, aA) \cdot (-1)^{s_b - m_b} \\ &\times \langle J_A, j, M_A, M_B - M_A | J_B, M_B \rangle \langle s_a, s_b, m_a, -m_b | s, m_a - m_b \rangle \\ &\times \langle \ell, s, m, m_a - m_b | j, M_B - M_A \rangle \end{aligned} \quad (4.10)$$

where $m = M_B - M_A + m_b - m_a$. The symbols bB, aA in the argument of G denote the dependence of G on the various nuclear quantum numbers other than the z -components of the spins. The function G can be defined by the inverted form of expansion (4.10)

$$\begin{aligned}
 G_{\ell sj, m} &= i^{\ell} J \frac{2\ell+1}{2J_B+1} \sum_{M_B M_A m_b m_a} \langle J_B M_B, s_b m_b | V_{int} | J_A M_A, s_a m_a \rangle \\
 &\times (-1)^{s_b - m_b} \langle J_A, j, M_A, M_B - M_A | J_B, M_B \rangle \langle s_a, s_b, m_a, -m_b | s, m_a - m_b \rangle \\
 &\times \langle \ell, s, m, m_a - m_b | j, M_B - M_A \rangle \\
 &= A_{\ell sj} f_{\ell sj, m}(\vec{r}_b, \vec{r}_a)
 \end{aligned} \tag{4.11}$$

The separation of G into a spectroscopic coefficient A and a form factor f is a matter of convenience in numerical computation, so that standard form factors and normalization can be used. For example, in the study of neutron hole states by the (p, d) or $(^3\text{He}, \alpha)$ reactions, the form factor is the same in both reactions but the spectroscopic coefficient, $A_{\ell sj}$, is different.

In a (d, n) stripping reaction, $a = p+n$, $b = n$ and $B = A+p$. The interaction potential can then be written as:

$$\begin{aligned}
 V_{int} &= V_{bB} - U_{bB} \\
 &= V_{np} + (V_{nA} - U_{nB}) \\
 &\approx V_{np}
 \end{aligned} \tag{4.12}$$

where U_{bB} (or U_{nB}) is the optical potential describing the scattering of particle b (or n) by the residual nucleus B . It is customary to take the neutron-proton interaction term, V_{np} , as the dominant term in the interaction potential and assume there is a cancellation between the neutron-target interaction and the optical potential in the exit channel.

Let us now consider the nuclear matrix element of equation (4.1) once more. It can be written explicitly as:

$$\begin{aligned} \langle J_B^{M_B}, s_b m_b | V_{int} | J_A^{M_A}, s_a m_a \rangle &= \int \psi_{J_B^{M_B}}^* (\xi_A \xi_p, \vec{r}_{pA}) \psi_{1/2, m_n}^* (\xi_n) \\ &\cdot V_{np}(\xi_n \xi_p, r_{np}) \psi_{1, m_a}(\xi_n \xi_p, r_{np}) \psi_{J_A^{M_A}}(\xi_A) d\xi_n d\xi_p d\xi_A \end{aligned} \quad (4.13)$$

where ξ_i represents the spin variables and the internal coordinates of particle i ; and r_{pA} and r_{np} are respectively the distances between the centres of mass of the proton and the target nucleus, and of the neutron and the proton. In the above expression, the interaction, V_{np} , is taken to be scalar, that is only the S-state of relative motion between the neutron and the proton is taken into consideration, while the D-state is neglected. Since the interaction is independent of ξ_A , these internal coordinates of the target can be integrated over immediately. The consequent overlap with the residual nucleus B defines the wave function ϕ for the captured proton,

$$\int \psi_{J_B^{M_B}}^* (\xi_A \xi_p, \vec{r}_{pA}) \psi_{J_A^{M_A}}(\xi_A) d\xi_A = \sum_j \langle J_A, j, M_A, m | J_B^{M_B} \rangle \phi_{j\mu}^* (\xi_p, \vec{r}_{pA}) \quad (4.14)$$

$\phi_{j\mu}$ can be expanded further as:

$$\phi_{j\mu}(\xi_p, \vec{r}_{pA}) = \sum_m \left\langle \ell, \frac{1}{2}, m, \mu-m | j\mu \right\rangle R_{\ell j}(r_p) i^\ell Y_\ell^m(\theta_p, \phi_p) \psi_{1/2, \mu-m}(\xi_p) \quad (4.15)$$

It has been customary to regard $\phi_{j\mu}$ as proportional to the shell model single-particle wave function for the orbit $(n\ell j)$ so that

$$R_{\ell j}(r_p) = \sqrt{S_{\ell j}} U_{n\ell j}(r_p) \quad (4.16)$$

where $U_{n\ell j}(r)$ is the normalized radial wave function of the captured proton and $S_{\ell j}$ is the spectroscopic factor.

Putting equations (4.14), (4.15) and (4.16) into equation (4.13), the nuclear matrix element can now be written as:

$$\begin{aligned} \langle J_B M_B, s_b m_b | V_{int} | J_A M_A, s_a m_a \rangle &= \sum_{\ell s j} i^\ell (-1)^{s_b - m_b} \langle J_A, j, M_A, M_B - M_A | J_B M_B \rangle \\ &\times \langle s_a, s_b, m_a, -m_b | s, m_a - m_b \rangle \langle \ell, s, m, m_a - m_b | j, M_B - M_A \rangle \sqrt{\frac{2s_a + 1}{2s + 1}} \\ &\times \sqrt{S_{\ell j}} U_{\ell s j}(r_p) Y_\ell^{m*}(\theta_p, \phi_p) V_{np} \phi_d(r_{np}) \end{aligned} \quad (4.17)$$

where $\phi_d(r_{np})$ is defined by:

$$\begin{aligned} \psi_{1m_d}(\xi_n, \xi_p, r_{np}) &= \phi_d(r_{np}) \sum_{m_p} \left\langle \frac{1}{2}, \frac{1}{2}, m_p, m_d - m_p | 1, m_d \right\rangle \\ &\times \psi_{1/2, m_p}(\xi_p) \psi_{1/2, m_d - m_p}(\xi_n) \end{aligned}$$

In the zero range approximation, one gets

$$V_{np} \phi_d(r_{np}) = D_0 \delta(r_{np}) \quad (4.18)$$

where

$$D_0 = -\frac{\hbar^2}{M} \int (\nabla^2 - \alpha^2) \phi_d(r) dr$$

M is the deuteron reduced mass and α is related to the deuteron binding energy, ϵ , by the expression

$$\epsilon = \hbar^2 \alpha^2 / M$$

The Hulthén wave function is usually chosen for $\phi_d(r)$.

Substituting equations (4.11) to (4.10) and comparing equations (4.10) and (4.17), the spectroscopic coefficient, $A_{\ell sj}$ and the form factor, $f_{\ell sj, m}$ can be written as:

$$A_{\ell sj} = \sqrt{\frac{2s_a+1}{2s+1}} \sqrt{S_{\ell j}} D_0 \quad (4.19)$$

and
$$f_{\ell sj, m} = U_{\ell sj}(r_p) \quad (4.20)$$

Note that the Jacobian, J in equation (4.10) cancels out when the zero range approximation is carried out.

The transition amplitude [equation (4.1)] can now be written as:

$$T = \sum_{\ell sj} (2j+1)^{1/2} A_{\ell sj} \langle J_A, j, M_A, M_B - M_A | J_B M_B \rangle \beta_{\ell sj}^{\ell m m_B m_A}(\vec{k}_b, \vec{k}_a) \quad (4.21)$$

where $m = M_B - M_A + m_b - m_a$.

The reduced amplitude, β , is given by:

$$\begin{aligned}
 (2j+1)^{1/2} \beta_{sj}^{\ell m m_b m_a}(\vec{k}_b, \vec{k}_a) &= \sum_{m'_a m'_b m'} \langle \ell, s, m', m'_a - m'_b | j, m - m_b + m_a \rangle \\
 &\times \langle s_a, s_b, m'_a, -m'_b | s, m'_a - m'_b \rangle (-1)^{s_b - m'_b} \int d\vec{r}_a \int d\vec{r}_b \chi_{m'_b m_b}^{(-)*}(\vec{k}_b, \vec{r}_b) \\
 &\times f_{\ell s j, m'}(r_b, r_a) \chi_{m'_a m_a}^{(+)}(\vec{k}_a, \vec{r}_a) \quad (4.22)
 \end{aligned}$$

The differential cross section of the reaction is then given by:

$$\frac{d\sigma}{d\omega} = \frac{\mu_a \mu_b}{(2\pi\hbar^2)^2} \frac{k_b}{k_a} \frac{\sum |T|^2}{(2J_A+1)(2s_a+1)} \quad (4.23)$$

where μ_a and μ_b are the reduced masses of the respective particles and the sum is over the substates M_A , m_a , M_B and m_b .

The vector polarization, \vec{P}_b , of the outgoing particle is defined as:

$$\vec{P}_b = \frac{\langle \psi_{\text{final}} | \vec{s}_b | \psi_{\text{initial}} \rangle}{s_b}$$

where ψ_{initial} and ψ_{final} are the initial and final wave functions defining the systems respectively. For convenience in numerical computation, the spectroscopic coefficient A and the reduced amplitude, β are combined into a single symbol B ,

$$B_{sj}^{\ell m m_b m_a} = A_{\ell s j} \beta_{sj}^{\ell m m_b m_a}$$

Using the Basel sign convention, the polarization of the outgoing particle can now be written as:

$$P_b(\theta) = \frac{\sum [(s_b - m_b)(s_b + m_b + 1)]^{1/2} \text{Im}[B_{sj}^{\ell m m_b m_a} B_{s'm}^{\ell', m+1, m_b+1, m_a*}]}{s_b \sum [B_{sj}^{\ell m m_b m_a} B_{s'j}^{\ell', m m_b m_a*}]} \quad (4.24)$$

where the sums in both the numerator and denominator are over $s, s', \ell, \ell', j, m_a, m_b$, and m . In a (d,n) reaction, $P_b(\theta)$ is the neutron polarization at an emission angle of θ .

In the absence of spin-orbit coupling, the distorted waves, $\chi_{mm'}$, of equation (4.2) become diagonal, since $m=m'$. For a deuteron stripping reaction, equation (4.24) can be reduced to:

$$P_b(\theta) = \frac{4}{3} \sum_j a_j \pi_\ell(\theta) \ell(j-\ell)/(2j+1) \quad (4.25)$$

where

$$a_j = \frac{|A_{\ell s j}|^2}{\sum_j |A_{\ell s j}|^2}$$

and

$$\pi_\ell(\theta) = \frac{\sum_m [(\ell+m+1)(\ell-m)]^{1/2} \text{Im}[\beta_{sj}^{\ell m} \beta_{sj}^{\ell, m+1*}]}{\ell \sum_m |\beta_{sj}^{\ell m}|^2}$$

The spin dependent effect due to the captured particle can now be seen from equation (4.25), if spin-orbit coupling in forming the distorted waves is neglected. From equation (4.25) one gets,

$$P_b(\theta) = \frac{1}{3} \pi_\ell(\theta) \frac{\ell}{\ell+1} \quad \text{for } j = \ell + \frac{1}{2} \quad (4.26a)$$

and
$$= -\frac{1}{3}\pi_\ell(\theta) \quad \text{for } j = \ell - \frac{1}{2} \quad (4.26b)$$

π_ℓ is just the expectation value of the projection of the vector ℓ on $\vec{k}_a \times \vec{k}_b$, i.e.

$$\pi_\ell = \frac{\langle \ell_y \rangle}{\ell}$$

and thus cannot exceed unity. Since a_j as defined in equation (4.25) is also less than unity, equation (4.26) gives the limitation $|P_b(\theta)| \leq \frac{1}{3}$ in the absence of spin-orbit coupling. For the case when $\ell=0$ for the captured particle, equation (4.25) predicts the polarization $P_b(\theta)$ to be zero. Experimentally, it has been found that the above polarization predictions from DWBA calculations without spin-orbit coupling are not true. Hence spin-orbit coupling must be included in the calculation.

A DWBA code (Ma 64) written by B.E.F. Macefield of Oxford University, England was used in the analysis of the neutron polarization measurements obtained from the $^{28}\text{Si}(d,n)^{29}\text{P}$ reaction. A discussion on this reaction is given in the next chapter.

The computer code was originally written in Fortran II language and used with an IBM 7030 (STRETCH) computer. It computes the differential cross section and the polarization angular distribution for the outgoing particles in a deuteron stripping reaction. Zero range and local potentials are employed in the calculation; while spin-orbit coupling in the incident and exit channels, as well as for the captured nucleon is included. The bound state radial wave functions $U_{n\ell j}(r)$ of the captured

nucleon are the normalized eigenfunctions of the Schrödinger equation with a well of the Saxon-Woods shape giving the correct binding energy. The logarithmic derivative of this internal wave function is then matched to that obtained from the external wave function (the Coulomb function) outside the nucleus. The depth of the Saxon-Woods well is then adjusted successively until the logarithmic derivatives are joined smoothly (Bu 60, Bu 61).

The shape of the real part of the optical potential is of the Saxon-Woods form. There are three choices for the shape of the imaginary part of the potential. The volume absorption is of the Saxon-Woods form, While for surface absorption it can be either Gaussian or derivative of the Saxon-Woods form. As for the spin-orbit potential, the shape is of the Thomas kind (see equation 4.9). Also the charge distribution of the nucleus is taken as that of a uniformly charged sphere.

The computer code was translated into Fortran IV and used with the IBM 7040 computer at the University of Alberta. Since the memory core of the computer is only 32 K words of 32 bits each, the program was divided into three links. Also the maximum number of partial waves used in the analysis was reduced from 50 to 30.

CHAPTER V

NEUTRON POLARIZATION FROM THE $^{28}\text{Si}(\text{d},\text{n})^{29}\text{P}$ REACTION

The polarization angular distributions of neutrons to the ground, 1.38 and 1.96 MeV states of ^{29}P from the reaction $^{28}\text{Si}(\text{d},\text{n})^{29}\text{P}$ were measured at a deuteron bombarding energy of 5.0 MeV. The energy level diagram of the nucleus ^{29}P is shown in Fig. 5-1.

5.1 Experimental Details

The silicon target was made by evaporating a piece of natural silicon onto a piece of gold backing (.005" thick) in vacuum. An electron gun[†] was used in the evaporation process. The thickness of silicon in the target was about 250 $\mu\text{g}/\text{cm}^2$. An average pulsed deuteron beam current of about 2.5 μA was used. The target assembly was cooled by a rapid flow of air.

In order to eliminate false asymmetry, the two neutron detectors were interchanged in their right-left positions for the measurement at every angle. Typically it took 3-1/2 hours to accumulate 400 counts under the smallest time-of-flight peak of interest. Hence for the measurement at one angle, it took about 7 hours of counting time.

Fig. 5-2 shows a neutron time-of-flight spectrum of the $^{28}\text{Si}(\text{d},\text{n})^{29}\text{P}$ reaction at a neutron emission angle of 60° (lab). The neutron flight path was 2 metres. A scale of the neutron flight time is shown as a

[†]Model CP-500, Andar Corporation, Mountain View, California

Fig. 5-1 The energy level diagram of the nucleus ^{29}P

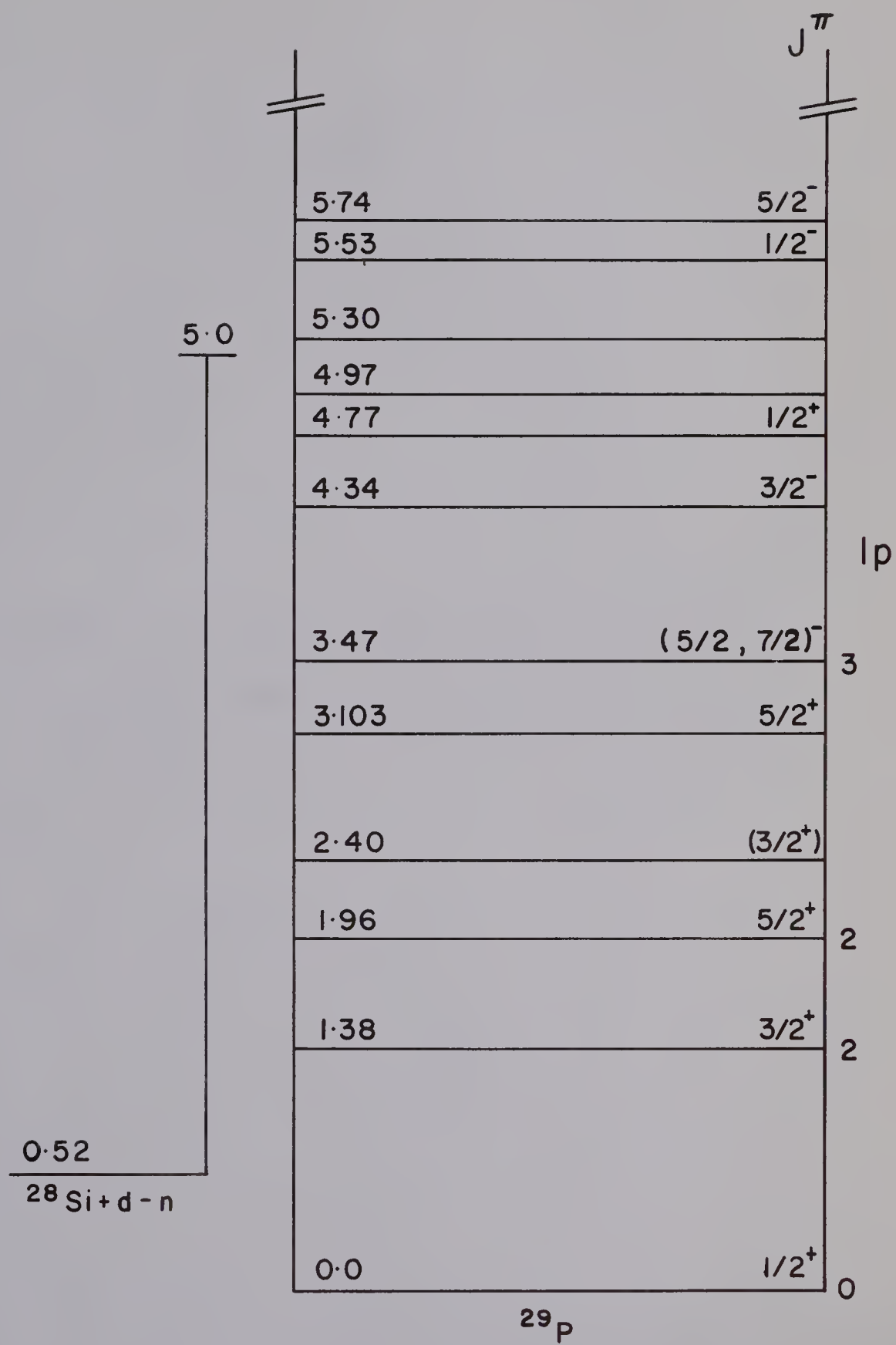
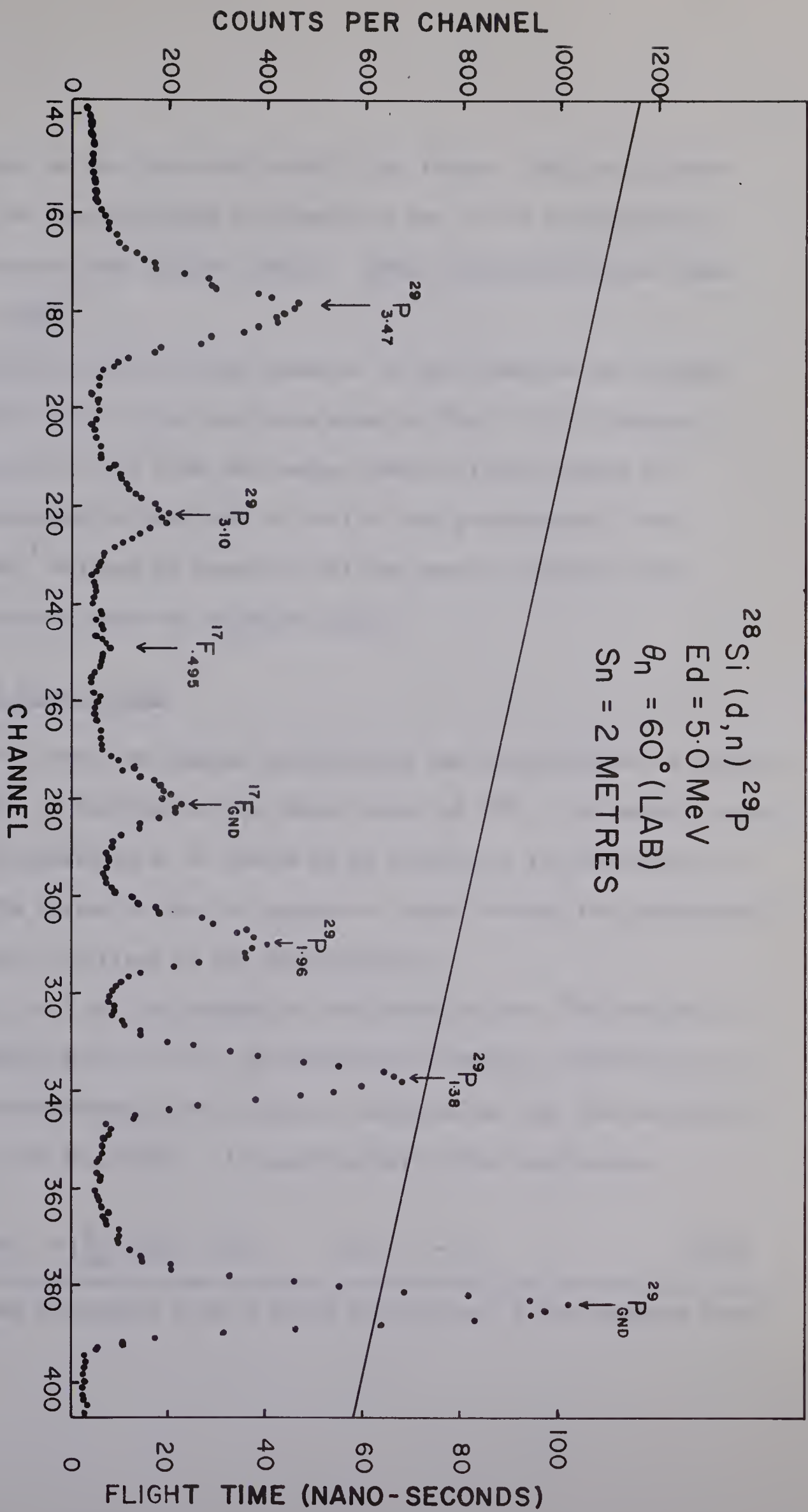


Fig. 5-2 A neutron time-of-flight spectrum of the $^{28}\text{Si}(\text{d},\text{n})^{29}\text{P}$ reaction with $E_{\text{d}}=5.0$ MeV, $\theta=60^{\circ}(\text{lab})$ and flight path =2m.



vertical axis on the right-hand side of the figure. The two fluorine states in the time-of-flight spectrum were due to ^{16}O contamination on the surface of the silicon target. Carbon contamination was found to be very small.

The neutron time-of-flight spectra of this reaction as recorded by the polarization system have been shown in Fig. 2-13 of chapter 2. They correspond to the true and random time-of-flight spectra of neutrons scattered to the right or left by the polarimeter. The computer code[†] written by Tepel (Te 66) was used to find the total number of counts under the different peaks.

5.2 Ground State of ^{29}P

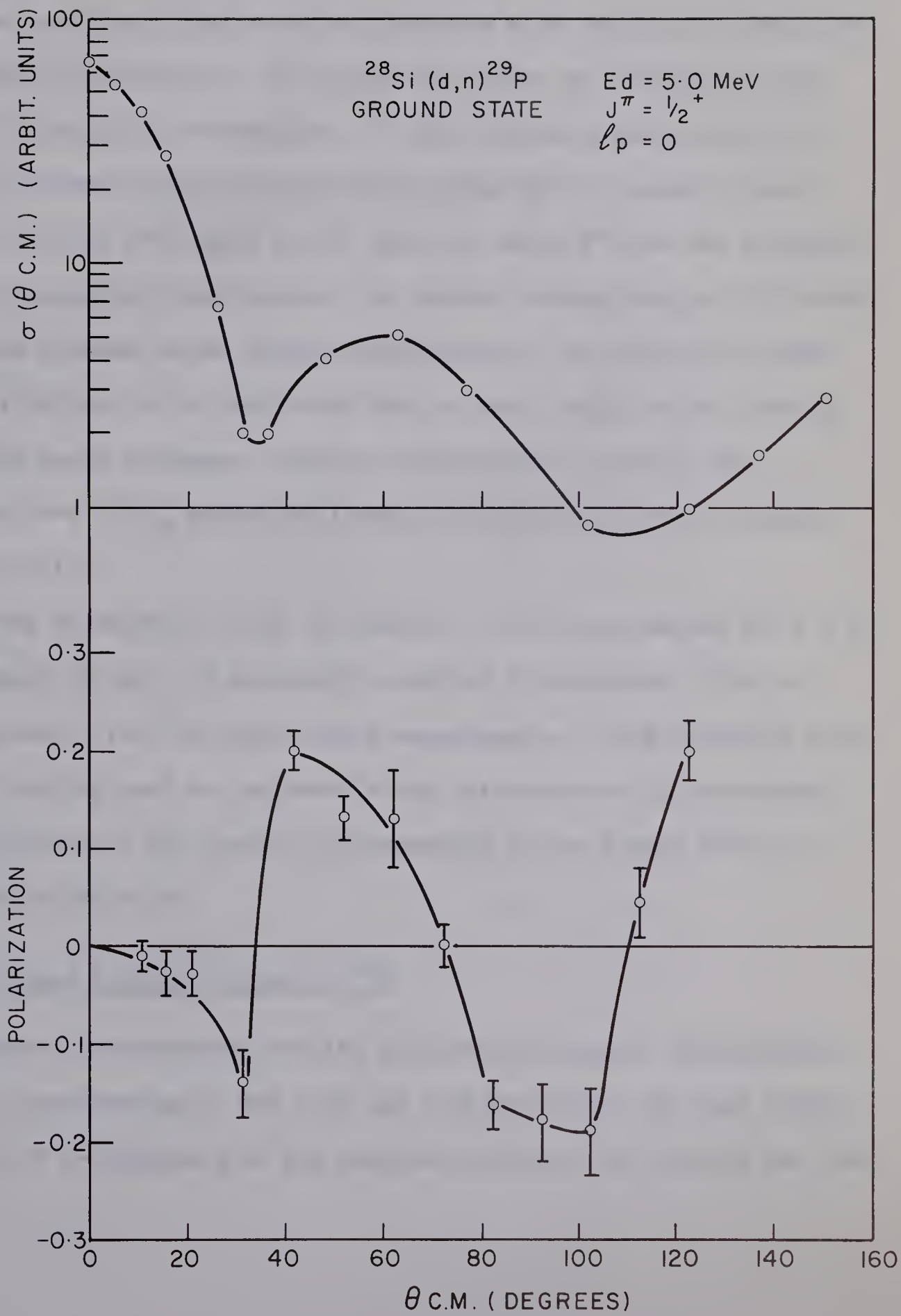
Fig. 5-3 shows the angular distribution and the polarization angular distribution of neutrons to the ground state of ^{29}P . The angular distribution was measured by W. G. Davies et al (Da66 A) at the University of Alberta. The curves in the two graphs are drawn through the experimental points to show the trend of the distributions.

Since $\ell_p = 0$ for the capture of the proton by the ^{28}Si nucleus to form the ground state of ^{29}P , the polarization angular distribution of neutrons corresponding to this state is expected to obey the derivative rule (Ro 59, Bi 60, Jo 62). In equation form, this rule states:

$$P(\theta) \propto \left[\frac{d}{d\theta} \sigma(\theta) \right] / \sigma(\theta) \quad \text{for } \ell = 0 \quad (5.1)$$

[†] See end of chapter 3 for a brief description of the computer code.

Fig. 5-3 Angular distribution and polarization angular distribution of neutrons to the ground state of ^{29}P



The behaviour of the polarization angular distribution from our measurements as compared to the derivative rule can be seen from Fig. 5-3. It increases negatively from zero in accordance with the sign of the slope of the angular distribution. It crosses zero first at 35° which is the minimum of the angular distribution. It then increases positively and is again in agreement with the sign of the slope of the angular distribution. It crosses zero again at 72° which is about 8° from the secondary maximum of the angular distribution. It finally crosses zero at 110° which is the second minimum of the angular distribution. As for the magnitude of the polarization, it is also clear that it gets larger at the turning points as the angle increases. Hence, qualitatively at least, the distribution from $^{29}\text{P}_{\text{gnd}}$ agrees well with the derivative rule as defined by equation (5-1).

According to equation (4-25) in chapter 4, the polarization for $\ell = 0$ should be equal to zero, if spin-orbit coupling is neglected. This is surely not true in the ^{29}P ground state measurements. This indicates that spin-orbit coupling must be included in the calculation of polarization.

A tabulation of the results corresponding to the ground state of ^{29}P is shown in Table 5-1.

5.3 The 1.38 and 1.96 MeV States of ^{29}P

The angular distributions and the polarization angular distributions of neutrons corresponding to the 1.38 and 1.96 MeV states are very useful in the study of j -dependence of the captured nucleon. The ℓ -value for the

Table 5-1. Polarization of neutrons from the $^{28}\text{Si}(\text{d},\text{n})^{29}\text{P}_{\text{gnd}}$ reaction at $E_{\text{d}} = 5.0$ MeV

| $\theta(\text{lab})$ deg. | $\theta(\text{c.m.})$ deg. | $\langle P_2 \cos \phi \rangle$ | Polarization |
|------------------------------|-------------------------------|---------------------------------|--------------------|
| 10 | 10.47 | .9519 | $-(.010 \pm .017)$ |
| 15 | 15.70 | .9563 | $-(.038 \pm .024)$ |
| 20 | 20.93 | .9583 | $-(.028 \pm .022)$ |
| 30 | 31.36 | .9605 | $-(.139 \pm .037)$ |
| 40 | 41.75 | .9619 | $+(.204 \pm .022)$ |
| 50 | 52.08 | .9631 | $+(.133 \pm .018)$ |
| 60 | 62.36 | .9641 | $+(.130 \pm .051)$ |
| 70 | 72.56 | .9651 | $+(.002 \pm .023)$ |
| 80 | 82.65 | .9659 | $-(.163 \pm .028)$ |
| 90 | 92.72 | .9666 | $-(.178 \pm .040)$ |
| 100 | 102.68 | .9672 | $-(.190 \pm .047)$ |
| 110 | 112.56 | .9677 | $+(.045 \pm .034)$ |
| 120 | 122.36 | .9681 | $+(.209 \pm .029)$ |

captured proton is 2 in these two states. For the 1.38 MeV state

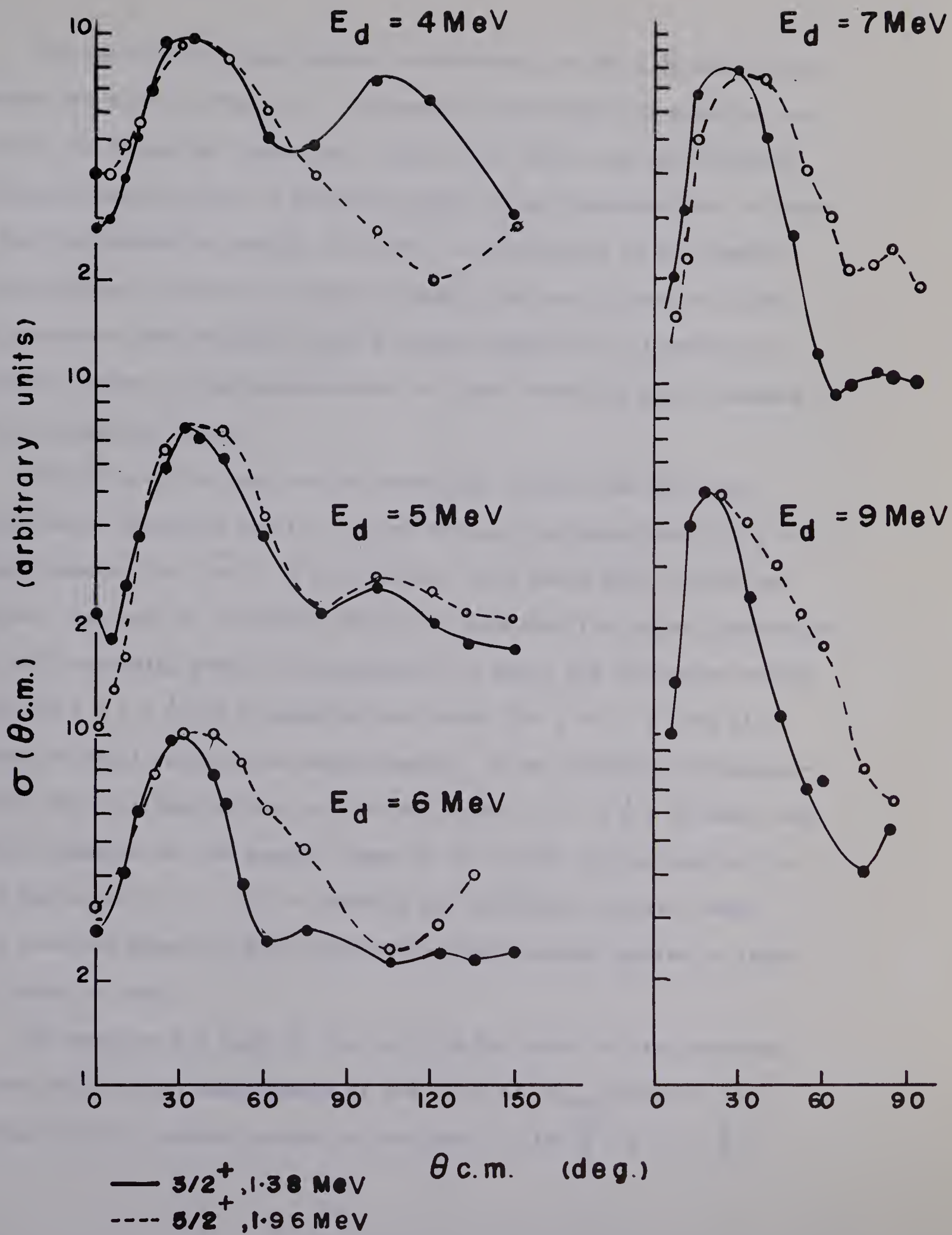
$$j = \ell - \frac{1}{2} = \frac{3}{2}, \text{ while for the 1.96 MeV state } j = \ell + \frac{1}{2} = \frac{5}{2}.$$

Lee and Schiffer (Le 64A) noticed in their survey of (d,p) stripping reactions that for $\ell_n = 1$ and $j = \frac{1}{2}^-$ states the angular distribution shows a minimum between 100° and 135° (c.m.), while that for $\ell_n = 1$ and $j = \frac{3}{2}^-$ does not show a minimum in this angular region. They attribute this difference to the j -dependence of the captured neutron, and suggest that such an indication in the angular distribution might be useful in assigning j -values.

On the basis of DWBA calculations, the spin-orbit interaction of the captured nucleon is attractive for the $j = \ell + \frac{1}{2}$ transition, while the opposite effect occurs in the $j = \ell - \frac{1}{2}$ transition. However, such effects have been estimated to be too small to change the shape of the angular distribution, although the magnitude of the cross section is affected (Le 64B).

The j -dependence for the 1.38 and 1.96 MeV states of ^{29}P is shown in Fig. 5-4. The 4.0, 5.0 and 6.0 MeV angular distributions were measured by W. G. Davies et al (Da 66B), while the 7.0 and 9.0 MeV angular distributions were measured by S. G. Buccino et al (Bu 66). The curves are drawn through the experimental points to show the trends of the distributions and they are normalized at the peak to show the j -dependence of the two states. For angles beyond the main stripping peak, the angular distribution for the 1.38 MeV state ($j = \ell - \frac{1}{2}$) drops faster than that for the 1.96 MeV state ($j = \ell + \frac{1}{2}$), except at $E_d = 4$ MeV, where compound nucleus effects may play a major role. This difference is observed to be more prominent at higher deuteron energies.

Fig. 5-4 The j-dependence effect as seen from the angular distributions of the 1.38 and 1.96 MeV states of ^{29}P at $E_d=4.0, 5.0, 6.0, 7.0$ and 9.0 MeV

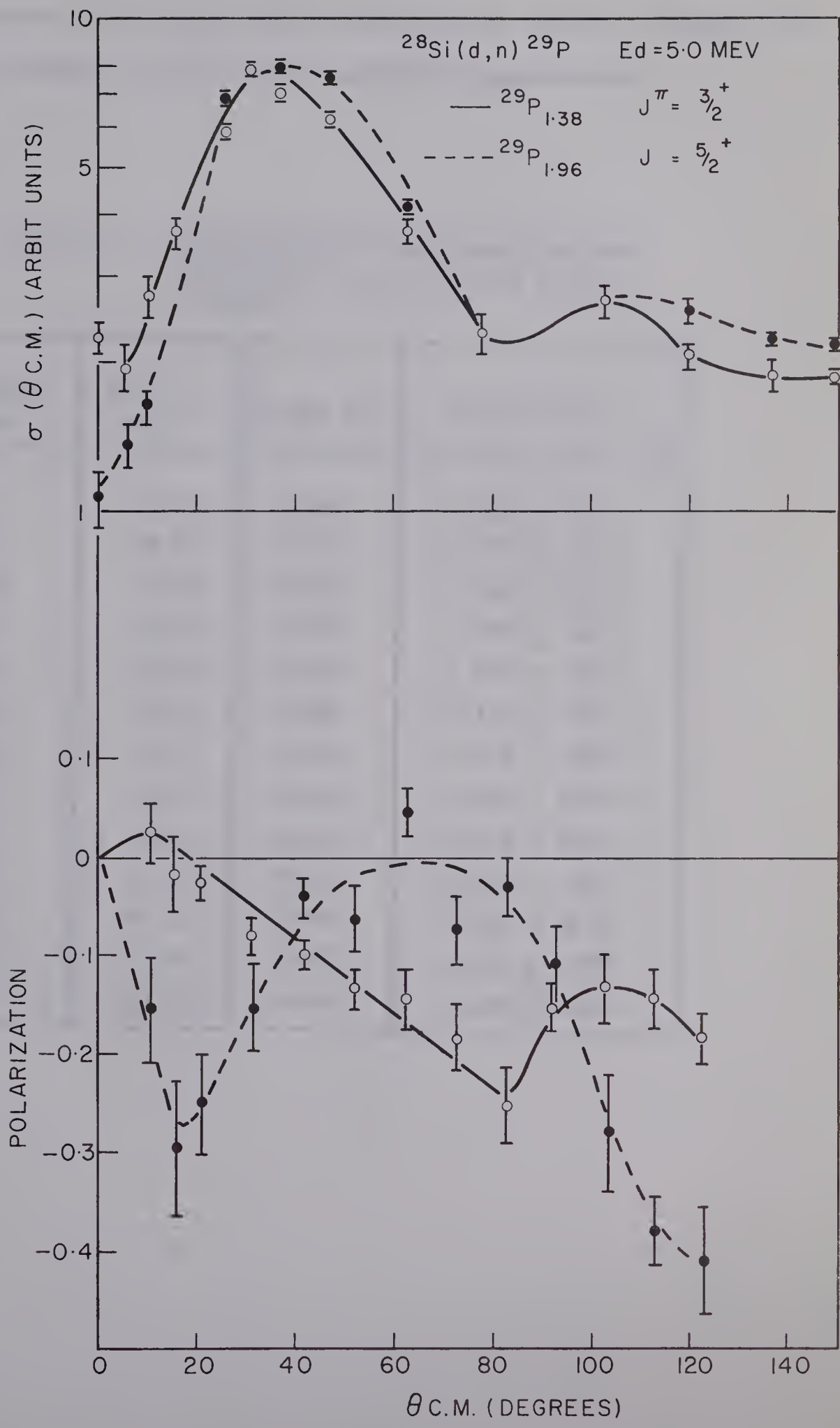
$\text{Si}^{28}(\text{d}, \text{n})\text{P}^{29}$


The polarization measurements corresponding to the 1.38 and 1.96 MeV states are shown in Fig. 5-5. The angular distribution is shown on the top of the figure for comparison. Again, the curves are drawn through the experimental points to show the trends of the distributions. At such a deuteron bombarding energy (5.0 MeV), the difference in the angular distributions of these two states is small, but the difference in the polarization distributions is quite large, especially at forward and backward angles. Hence polarization is a more sensitive way of showing this j -dependent effect.

According to the sign rule as predicted by Newns (Ne 53), the polarization should be positive around the main stripping peak for $j = \ell + \frac{1}{2}$ and negative for $j = \ell - \frac{1}{2}$ transitions. Very often this rule is not obeyed. Instead, D. W. Miller (Mi 65) noticed that for angles just beyond the main stripping peak, the polarization is small and fluctuates around zero for $j = \ell + \frac{1}{2}$ and is negative and larger for $j = \ell - \frac{1}{2}$ from his survey of (d,p) polarization measurements. In our polarization measurements, the polarization for the 1.96 MeV state ($j = \ell + \frac{1}{2}$) is small and mostly negative for the angular range of 40° to 70° , while that for the 1.38 MeV state ($j = \ell - \frac{1}{2}$) is negative and definitely larger. Hence this observed trend in (d,p) polarization measurements applies to these two levels as well.

The negative dip near 15° for the 1.96 MeV state is also observed in our polarization measurements of the $^{16}\text{O}(d,n)^{17}\text{F}_{\text{gnd}}$ reaction. The j -value for the captured proton in this case is also $\frac{5}{2}^+$ ($j = \ell + \frac{1}{2}$).

Fig. 5-5 Angular distributions and polarization angular distributions of neutrons to the 1.38 and 1.96 MeV states of ^{29}P



Hence it would be interesting to see if other measurements for $j = \frac{5}{2}^+$ transitions would follow this trend.

Tabulations of the polarization measurements for the 1.38 and 1.96 MeV states are shown in Tables (5-2) and (5-3) respectively.

Table 5-2. Polarization of neutrons from the $^{28}\text{Si}(d,n)^{29}\text{P}_{1.38}$ reaction at $E_d = 5.0$ MeV

| $\theta(\text{lab})$ deg. | $\theta(\text{c.m.})$ deg. | $\langle P_2 \cos \phi \rangle$ | Polarization |
|------------------------------|-------------------------------|---------------------------------|------------------|
| 10 | 10.55 | .9526 | $+.024 \pm .032$ |
| 15 | 15.82 | .9567 | $-.175 \pm .041$ |
| 20 | 21.09 | .9583 | $-.028 \pm .022$ |
| 30 | 31.59 | .9595 | $-.083 \pm .019$ |
| 40 | 42.04 | .9595 | $-.099 \pm .013$ |
| 50 | 52.43 | .9589 | $-.136 \pm .022$ |
| 60 | 62.75 | .9579 | $-.146 \pm .032$ |
| 70 | 72.99 | .9564 | $-.185 \pm .034$ |
| 80 | 83.13 | .9545 | $-.253 \pm .042$ |
| 90 | 93.18 | .9523 | $-.153 \pm .027$ |
| 100 | 103.13 | .9499 | $-.133 \pm .035$ |
| 110 | 112.99 | .9473 | $-.146 \pm .029$ |
| 120 | 122.75 | .9466 | $-.186 \pm .023$ |

Table 5-3. Polarization of neutrons from the $^{28}\text{Si}(\text{d},\text{n})^{29}\text{P}_{1.96}$ reaction at $E_d = 5.0$ MeV

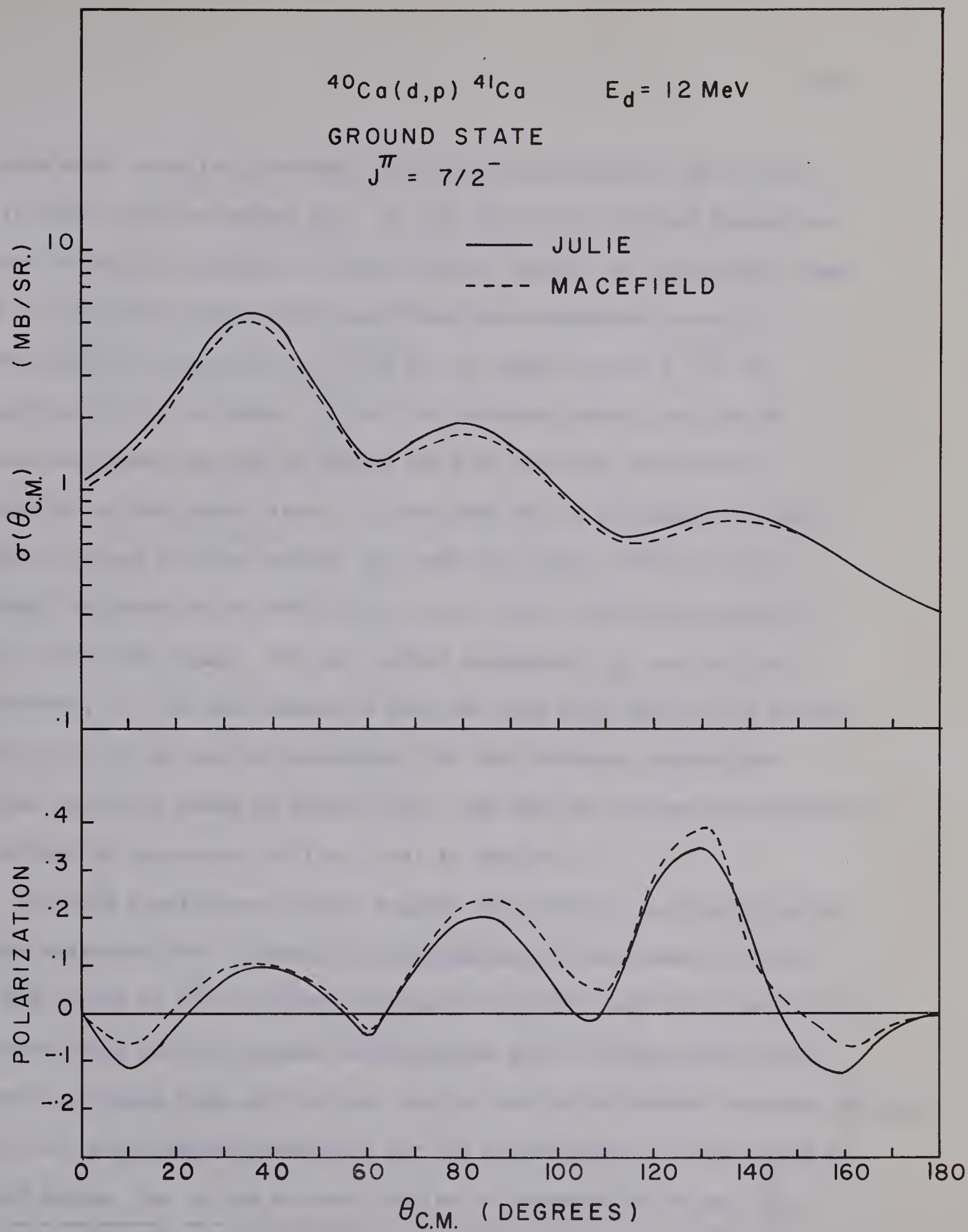
| $\theta(\text{lab})$ deg. | $\theta(\text{c.m.})$ deg. | $\langle P_2 \cos \phi \rangle$ | Polarization |
|------------------------------|-------------------------------|---------------------------------|--------------------|
| 10 | 10.60 | .9350 | $-(.155 \pm .058)$ |
| 15 | 15.89 | .9388 | $-(.296 \pm .070)$ |
| 20 | 21.18 | .9401 | $-(.249 \pm .051)$ |
| 30 | 31.73 | .9403 | $-(.153 \pm .048)$ |
| 40 | 42.22 | .9390 | $-(.043 \pm .022)$ |
| 50 | 52.64 | .9366 | $-(.064 \pm .035)$ |
| 60 | 62.99 | .9335 | $+(.045 \pm .028)$ |
| 70 | 73.24 | .9295 | $-(.075 \pm .037)$ |
| 80 | 83.40 | .9250 | $-(.030 \pm .031)$ |
| 90 | 93.45 | .9198 | $-(.111 \pm .040)$ |
| 100 | 103.40 | .9143 | $-(.280 \pm .060)$ |
| 110 | 113.24 | .9085 | $-(.381 \pm .036)$ |
| 120 | 122.99 | .9028 | $-(.410 \pm .056)$ |

5-4 DWBA Predictions

A comparison was made between the DWBA code written by Macefield (Ma 64) and the code "JULIE" written by Bassel, Drisko and Satchler (Ju 66). The output data for the $^{40}\text{Ca} (d,p) ^{41}\text{Ca}_{\text{gnd}}$ reaction at $E_d=12$ Mev from the two codes are shown in Fig (5-6). The shape of the angular distributions compares very well. "JULIE" estimates the cross section at the main stripping peak to be about 10% higher than that estimated by Macefield. The polarization outputs do not compare as well. However, with the present statistical accuracy in polarization measurements, one curve is as useful as the other in comparing theory with experiment for the present, though of course the question of accuracy of the Macefield program must be investigated more thoroughly when the new University of Alberta computer is operational.

The code written by Macefield has been used to calculate the polarization of neutrons corresponding to the ground, 1.38 and 1.96 MeV states of ^{29}P emitted in the $^{28}\text{Si}(d,n)^{29}\text{P}$ reaction. The deuteron optical parameters are taken from the results of Perey and Perey (Pe 66). They analysed the elastic scattering angular distributions of deuterons on ^{28}Si over an energy range of 10.0 to 11.8 MeV. They noticed that the inclusion of a spin-orbit potential improved the fits at large angles. From the automatic search code, they arrived at two sets of optical parameters, one with the real well depth at 65.95 MeV and the other at 188.5 MeV. These

Fig. 5-6 A comparison between "JULIE" and the DWBA code written by
Macefield



two sets were used in an attempt to fit our measurements, and a better fit is found with the second set. As for the neutron optical parameters, the set of optical parameters found by Rosen (Ro 65) for the energy range of 0.2 to 24 MeV is used. Buck and Perey[†] also suggested a set of neutron optical parameters, but this set is found to give a fit not as good as the set by Rosen. As for the captured proton, the set of optical parameters as used by Davies (Da 66A) has been used in the calculation of the ground state. If the same set of parameters is used for the 1.38 and 1.96 MeV states, the real well depth, which is automatically adjusted by the DWBA code, is more than 100 MeV for these two states. For this reason, the real radial parameter, r_R , and the real diffuseness, α_R , are made larger to keep the real well depth below 100 MeV. A tabulation of the optical parameters for the deuteron, neutron and captured proton is shown in Table (5-4). The form of the optical potentials are defined by equations (4-5) to (4-9) in Chapter 4.

The DWBA predictions for the angular distributions and polarization angular distributions of neutrons corresponding to the ground, 1.38 and 1.96 MeV states of ^{29}P are shown in Figs.(5-7), (5-8) and (5-9) respectively. The predictions for the angular distributions give the right shape near the main stripping peak and they are too low for angles beyond the main stripping peak. The polarization prediction for the ground state is fairly good at forward angles, but at the backward angles, it becomes too large. For

[†]reported in reference Ro 65.

Table (5-4) OPTICAL MODEL PARAMETERS USED IN THE $^{28}\text{Si}(d,n)^{29}\text{Si}$ REACTION
AT DEUTERON ENERGY OF 5.0 MeV

| | Deuteron | Neutron |
|-------------------|----------|---------|
| V | 188.05 | 47.07 |
| W | 16.06 | 5.75 |
| V _{SO} | 11.21 | 5.05 |
| r _R | .651 | 1.25 |
| r _I | 1.518 | 1.25 |
| r _{coul} | 1.3 | -- |
| a _R | 1.047 | .65 |
| a _I | 0.564 | .7 |

| | CAPTURED PROTON | | |
|-------------------|------------------------------|------------------------|------------------------|
| | $^{29}\text{p}_{\text{gnd}}$ | $^{29}\text{p}_{1.38}$ | $^{29}\text{p}_{1.96}$ |
| V | 51.8 | 73.0 | 67.3 |
| V _{so} | -- | 5.0 | 5.0 |
| r _R | 1.25 | 1.5 | 1.5 |
| r _{coul} | 1.25 | 1.25 | 1.25 |
| a _R | .5 | 1.0 | 1.0 |

NOTE: All potentials are in MeV and all lengths are in fermis.

Fig. 5-7 DWBA predictions for the angular distribution and polarization
angular distribution of neutrons corresponding to the ground
state of ^{29}P

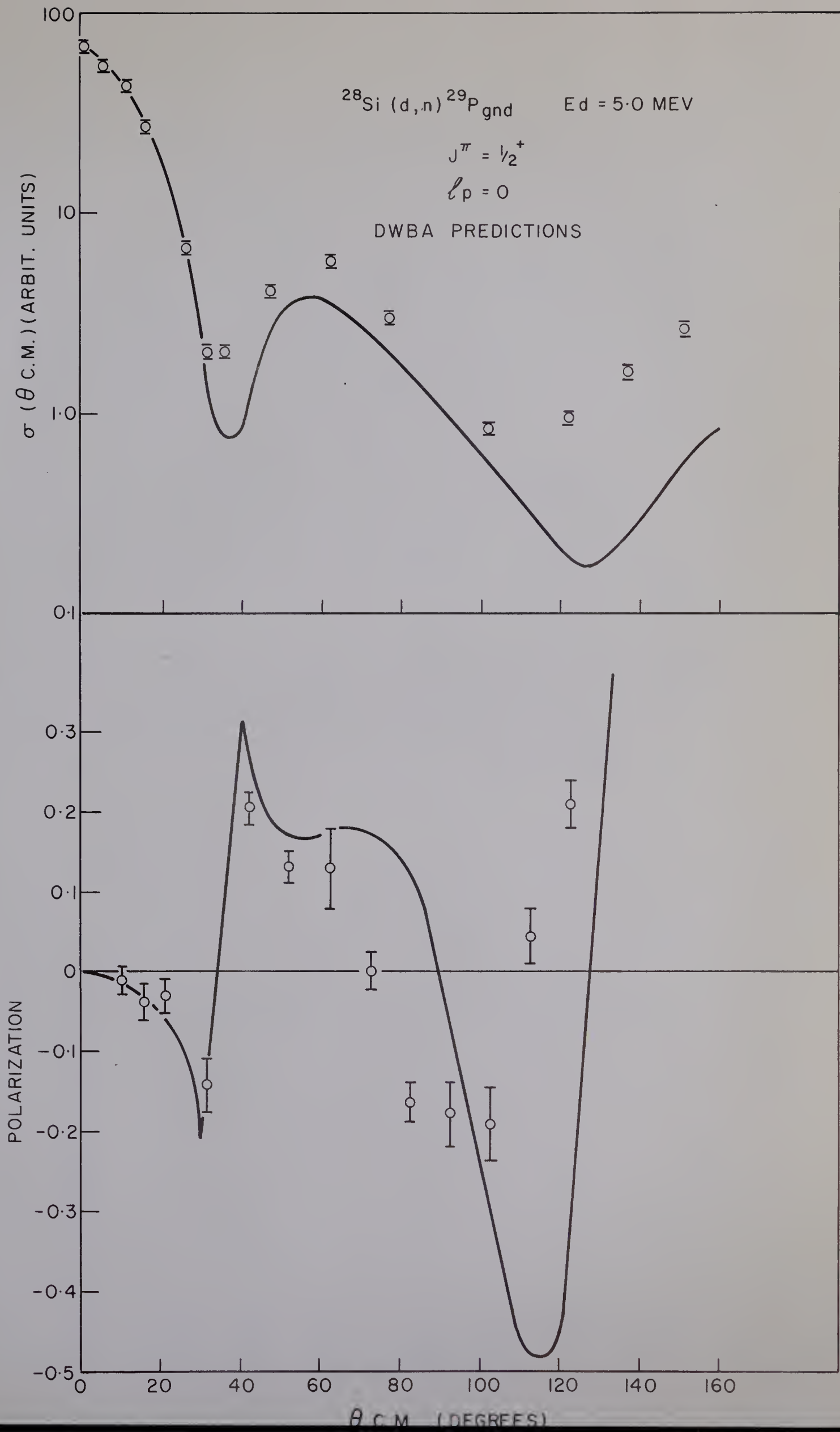


Fig 5-8 DWBA predictions for the angular distribution and polarization
angular distribution of neutrons corresponding to the 1.38 MeV
state of ^{29}P

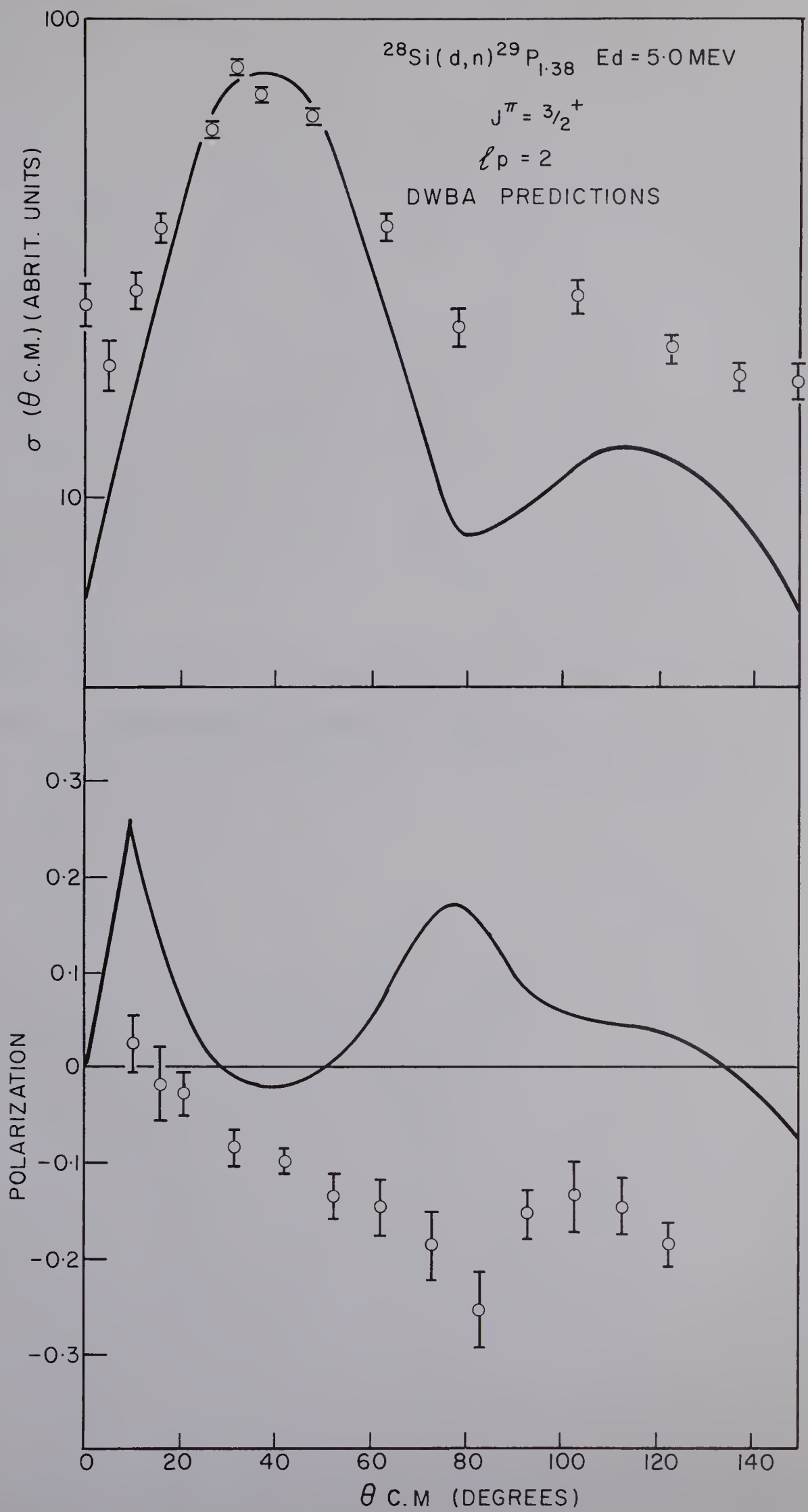
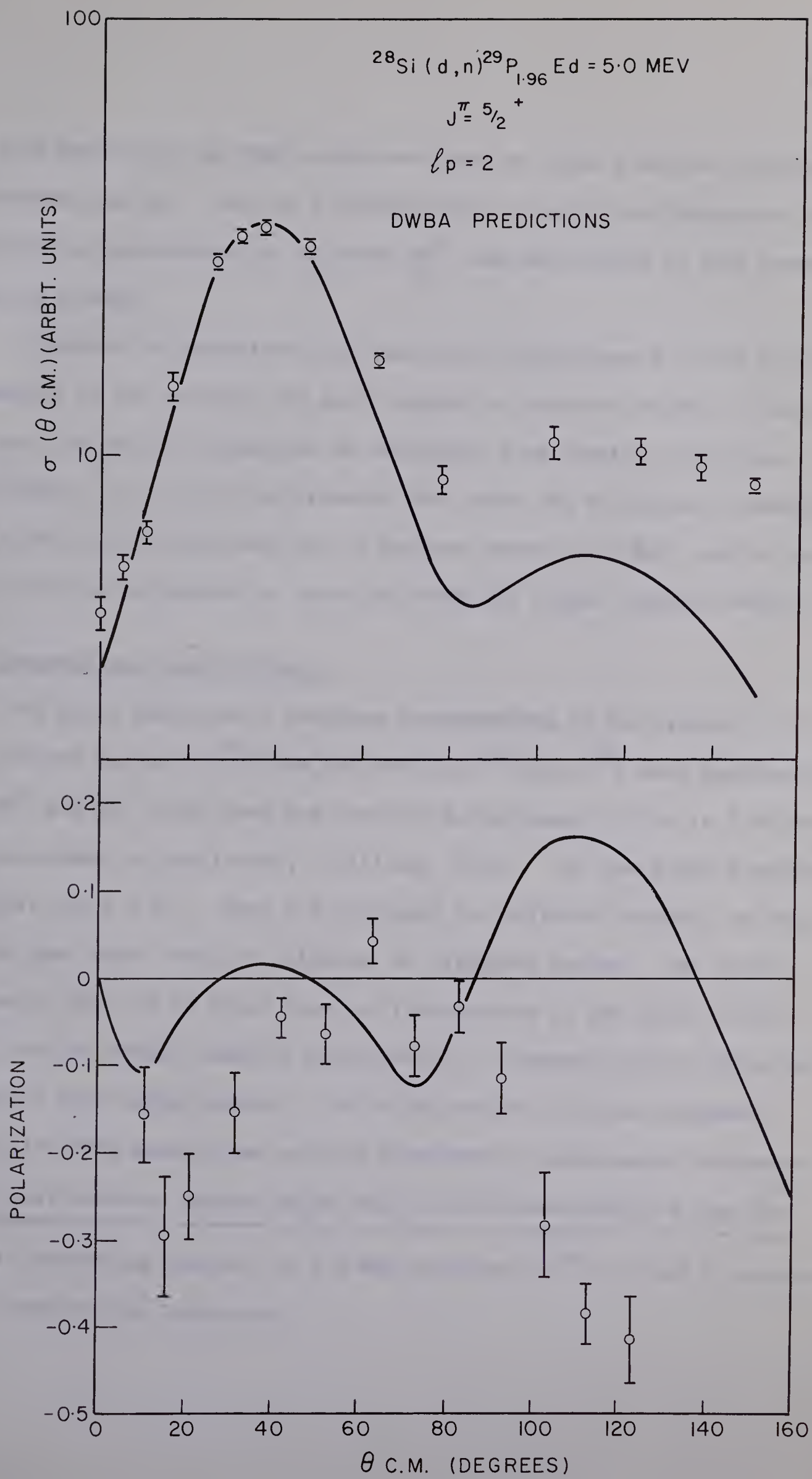


Fig. 5-9 DWBA predictions for the angular distribution and polarization
angular distribution of neutrons corresponding to the 1.96 MeV
state of ^{29}P



the 1.38 MeV state, the DWBA prediction does not agree with the polarization measurements at all. For the 1.96 MeV state, it gives the features of the polarization measurements up to about 80° , and beyond that it even becomes opposite in sign.

It should be emphasized that there are no adjustments in the optical parameters of the incident and exit channels to improve the fits. They are just the optical parameters as determined from elastic scattering experiments. It is quite unfortunate that there are no optical parameters from elastic scattering data near a deuteron energy of 5 MeV[†] and we have had to use the parameters of Perey and Perey for higher deuteron energy.

5-5 Compound and Direct Effects

The yield functions of neutrons corresponding to the ground, 1.38 and 1.96 MeV states of ^{29}P from the reaction $^{28}\text{Si}(d,n)^{29}\text{P}$ were measured at 20° , 60° and 120° (lab) over the deuteron energy range of 4.64 to 5.50 MeV. They are shown in Figs. (5-10), (5-11) and (5-12). All the yield functions fluctuate quite a bit. They are different for different states, and even for the same state they are different at different angles. One obvious conclusion that can be drawn from the fluctuations in the yield is that apart from the direct reaction contribution, a compound nuclear effect is present in this energy region. This might explain the poor agreement between the DWBA predictions and the experimental measurements discussed in the last section. Another point that is worth mentioning is that the

[†] Elastic scattering analysis of 5.0 MeV deuteron on ^{28}Si is now in process by D. Gurd of this laboratory.

Fig. 5-10 Yield functions of neutrons corresponding to the ground state of ^{29}P

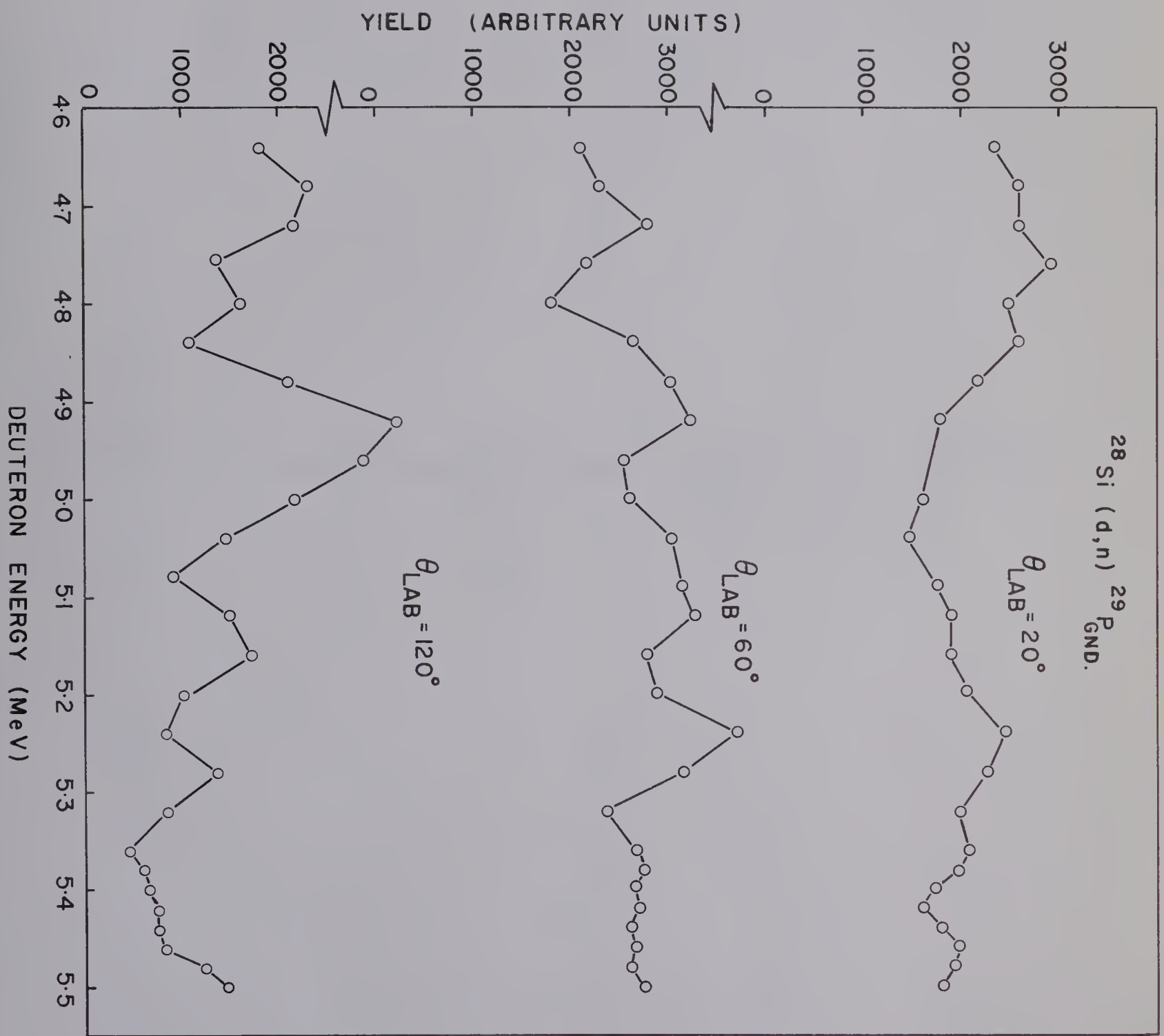


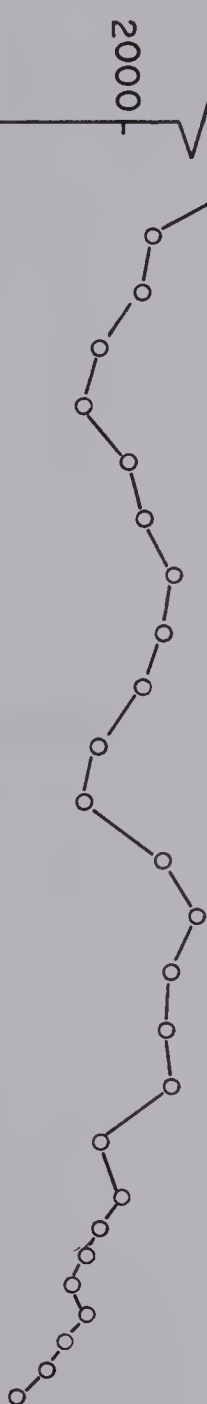
Fig. 5-11 Yield functions of neutrons corresponding to the 1.38 MeV
state of ^{29}P

$^{28}\text{Si} (d, n) ^{29}\text{P}_{1.38}$

$\theta_{\text{LAB}} = 20^\circ$



$\theta_{\text{LAB}} = 60^\circ$



$\theta_{\text{LAB}} = 120^\circ$

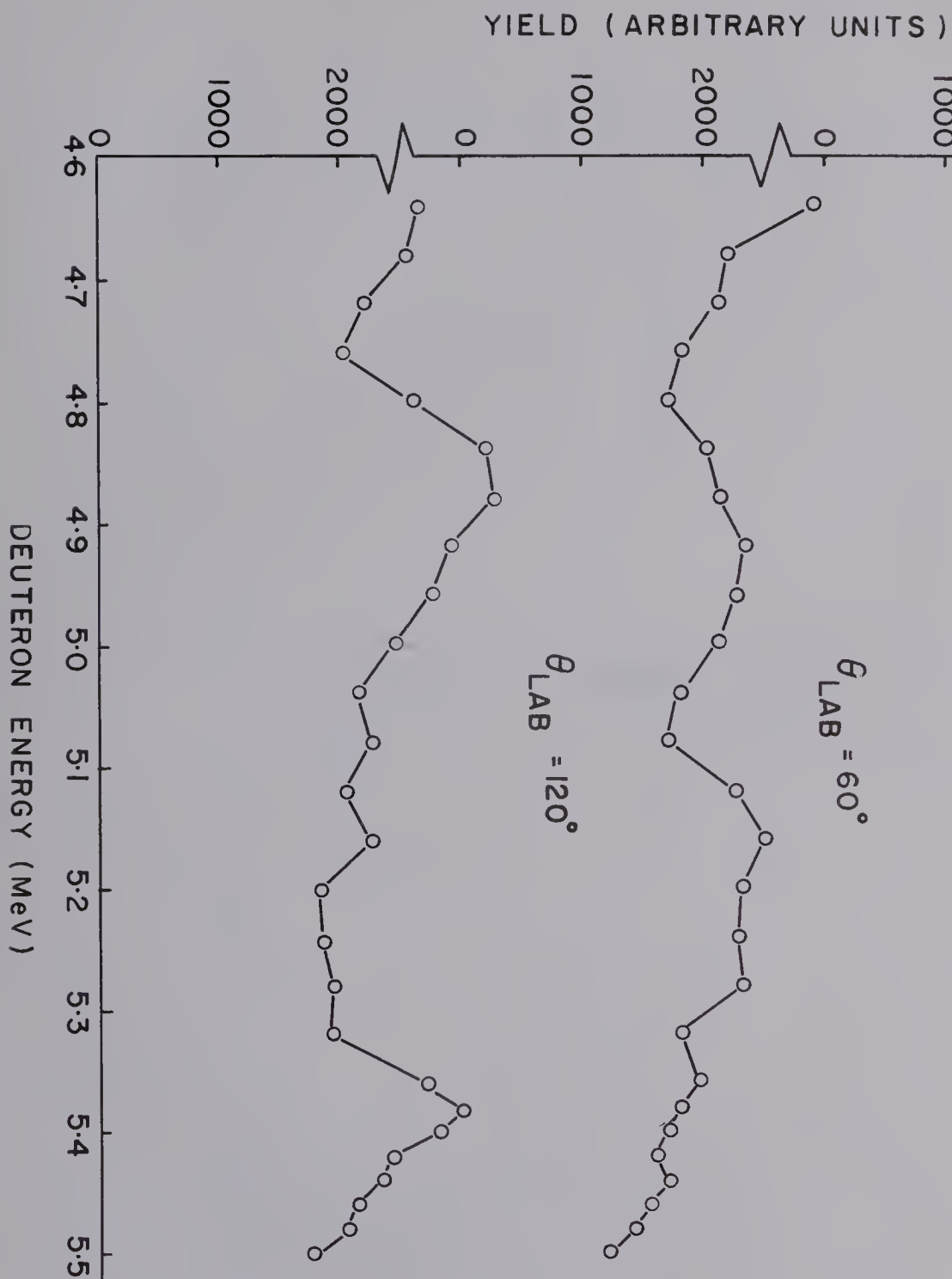
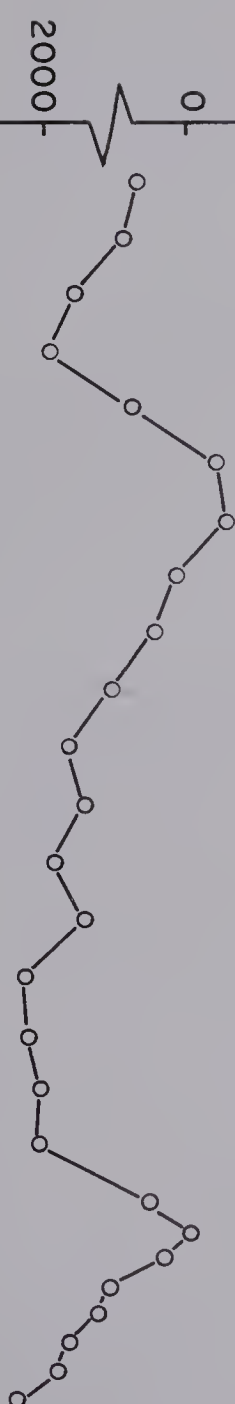
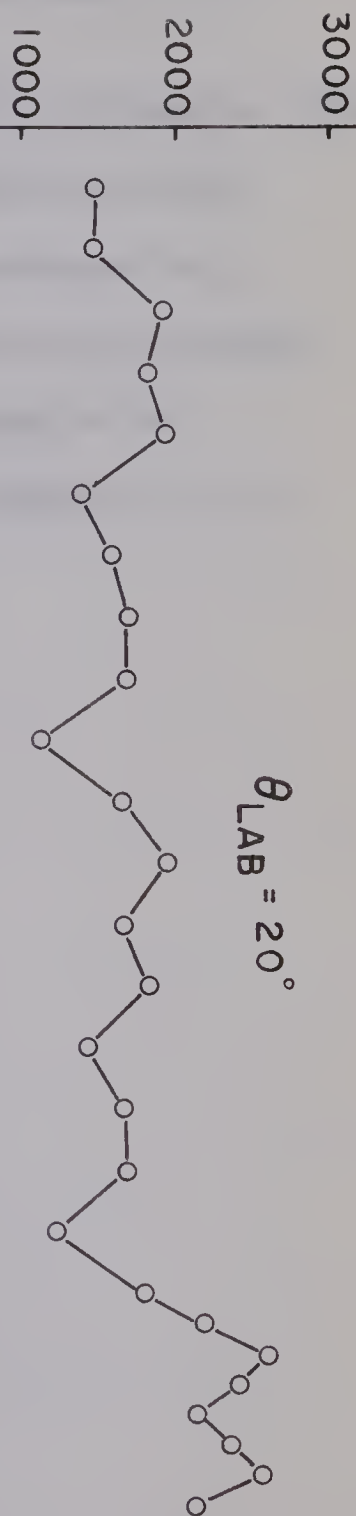


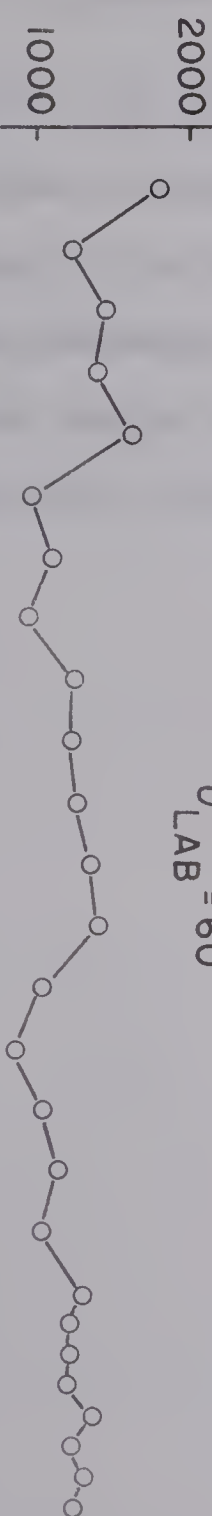
Fig. 5-12 Yield functions of neutrons corresponding to the 1.96 MeV
states of ^{29}P

$^{28}\text{Si}(d,n)^{29}\text{P}_{1.96}$

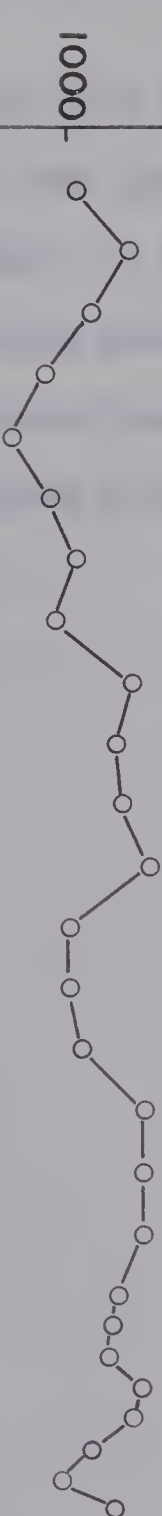
$\theta_{\text{LAB}} = 20^\circ$



$\theta_{\text{LAB}} = 60^\circ$



$\theta_{\text{LAB}} = 120^\circ$



YIELD (ARBITRARY UNITS)

DEUTERON ENERGY (MeV)

the measured polarization angular distribution corresponding to the ground state of ^{29}P is in good qualitative agreement with the derivative rule.

Since this rule is derived by means of an approximate DWBA calculation, this agreement may indicate that the direct reaction contribution is still predominant in this energy region. It is difficult to estimate the contribution from compound nuclear processes. A method in the separation of the direct reaction contribution and the compound nuclear effect is described by Austern in Chapter V.D. of Fast Neutron Physics, Part II (Au 63).

APPENDIX I

CALCULATION OF THE $n\text{-}^4\text{He}$ ANALYSING POWER

In this section a description of a computer program written for the calculation of the $n\text{-}^4\text{He}$ analysing power is given. In the calculation, a point target was assumed while the finite geometry of the scattering volume of the polarimeter and the neutron detector was taken into consideration. Since the maximum angle subtended by the scattering volume at a distance of 2 metres from the target was only $\pm 1.5^\circ$, the variation of cross section and polarization of the nuclear reaction over this angular range was not taken into consideration. The program was written in Fortran IV language and used with the IBM 7040 computer at the University of Alberta.

Recently a computer program has been written by G. M. Stinson and S. M. Tang of this laboratory to include the double scattering effect in the calculation of the analysing power. With the inclusion of this effect the analysing power is reduced by about 10 %. Since the difference is within the statistical uncertainty of the polarization measurements, the analysing power used in this thesis is calculated by considering single scattering alone.

A1.1 Principle of Calculation

Fig. A1-1 shows a schematic drawing of the polarization experiment configuration.

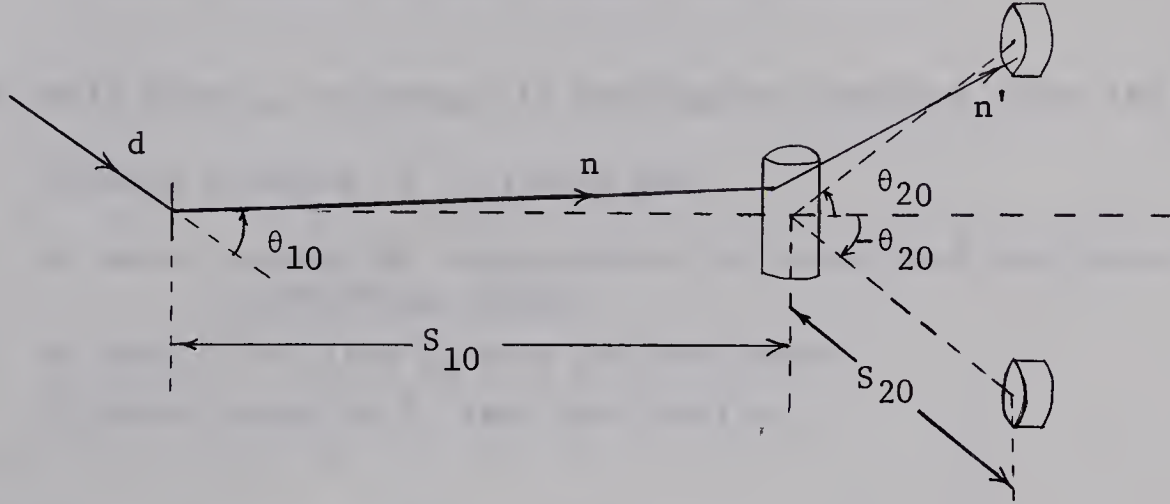


Fig. A1-1. A schematic drawing of the polarization configuration.

In this configuration, the target, the centre of the scattering volume and the centres of the two neutron detectors are in a horizontal plane. Let the distance between the target and the centre of the scattering volume be S_{10} and the distance between the centre of the scattering volume and the centre of the front face of the neutron detector be S_{20} . The scattering volume is placed at an angle of θ_{10} with respect to the incident deuteron beam, which is assumed to be horizontal, while the neutron detectors are placed at an angle of $\pm \theta_{20}$ with respect to the line joining the target and the centre of the scattering volume. For the purpose of convenience in numerical computation, the following coordinate systems[†] are introduced.

[†]The right hand rule is used in defining all the co-ordinate systems

(I) Deuteron reaction frame of reference with origin at the target.

Z_1 axis - along the incident deuteron direction and horizontal

X_1 axis - 90° from Z_1 axis and horizontal

Y_1 axis - normal to Z_1X_1 plane, i.e. vertical

(II) This frame of reference is obtained by rotating about the Y_1 axis through an angle of θ_{10} , such that

Z_2 axis - along the line joining the target and the centre of the scattering volume

X_2 axis - 90° from Z_2 axis and horizontal

Y_2 axis - same as Y_1 axis and vertical

(III) Neutron scattering frame of reference

This frame of reference is obtained by translating along Z_2 axis through a distance of S_{10} , such that

Z_3 axis - along the line joining the target and the centre of the scattering volume

X_3 axis - 90° from Z_3 axis and horizontal

Y_3 axis - normal to Z_3X_3 plane and vertical

(IV) This frame of reference is obtained by rotating about Y_3 axis through an angle of θ_{20} , such that

Z_4 axis - along the line joining the centres of the scattering volume and the neutron detector

X_4 axis - 90° from Z_4 axis and horizontal

Y_4 axis - normal to Z_4X_4 plane and vertical

(V) This frame of reference is obtained by translating along Z_4 axis through a distance of S_{20} , such that

Z_5 axis - along the line joining the centres of the scattering volume and the neutron detector

X_5 axis - 90° from Z_5 and horizontal

Y_5 axis - normal to Z_5Y_5 plane and vertical

For the finite geometry calculation of the analysing power of $n\text{-}^4\text{He}$, both the scattering volume and the neutron detectors are divided into small rectangular cells, and the scattering or the detection of the neutrons are assumed to occur at the centres of the cells. Since the scattering volume is a cylinder of 2 inches in diameter and 4 inches in height, the boundary conditions for the co-ordinates, (x_3, y_3, z_3) , of the centres of each of the cells are:

$$-(2 \times 2.54 - \frac{\Delta Y_3}{2}) \leq y_3 \leq (2 \times 2.54 - \frac{\Delta Y_3}{2}) \text{ cm}$$

and

$$z_3^2 + x_3^2 \leq (2.54)^2 \text{ cm}^2$$

where ΔY_3 is the cell dimension in the Y_3 -axis direction.

As for the neutron detector, which is 3-1/2 inches in diameter and 2 inches in length, the boundary conditions for the co-ordinates (x_5, y_5, z_5) of the centre of each of the cells are:

$$\frac{\Delta Z_5}{2} \leq z_5 \leq (2 \times 2.54 - \frac{\Delta Z_5}{2}) \text{ cm}$$

and
$$x_5^2 + y_5^2 \leq \left(\frac{3.5}{2} \times 2.54\right)^2 \text{ cm}^2$$

where ΔZ_5 is the cell dimension in the Z_5 -axis direction.

Let us now follow one of the neutron events in the system and calculate the different angles required in the numerical computation. The direction cosines of the incident deuteron direction with respect to System II are:

$$A_1 : B_1 : C_1 = -\sin\theta_{10} : 0 : \cos\theta_{10}$$

Since (x_3, y_3, z_3) are the co-ordinates of the centre of a cell in the scattering volume with respect to System III, then with respect to System II the co-ordinates are:

$$(x_3, y_3, S_{10} + z_3)$$

The direction cosines of the line joining the target and the centre of the cell in System II are:

$$A_2 : B_2 : C_3 = \frac{x_3}{G} : \frac{y_3}{G} : \frac{S_{10}+z_3}{G}$$

where
$$G = [x_3^2 + y_3^2 + (S_{10} + z_3)^2]^{1/2}$$

These are just the direction cosines of the outgoing neutron. Hence the angle, θ , between the incident deuteron beam and the outgoing neutron is given by:

$$\cos \theta_1 = A_1 A_2 + B_1 B_2 + C_1 C_2 \quad (A1-1)$$

The direction cosines of the normal to the reaction plane are:

$$A_3 : B_3 : C_3 = \frac{B_1C_2 - B_2C_1}{D} : \frac{A_2C_1 - A_1C_2}{D} : \frac{A_1B_2 - A_2B_1}{D} \quad (A1-2)$$

where $D = [(B_1C_2 - B_2C_1)^2 + (A_2C_1 - A_1C_2)^2 + (A_1B_2 - A_2B_1)^2]^{1/2}$.

With respect to System V, the co-ordinates of the centre of a cell in the neutron detector are (x_5, y_5, z_5) . With respect to System IV the co-ordinates are:

$$(x_5, y_5, S_{20} + z_5).$$

With respect to System III, the co-ordinates are:

$$x_5 \cos \theta_{20} + (S_{20} + z_5) \sin \theta_{20}$$

$$y_5$$

and $-x_5 \sin \theta_{20} + (S_{20} + z_5) \cos \theta_{20}$.

With respect to System II, the co-ordinates are:

$$H_1 = x_5 \cos \theta_{20} + (S_{20} + z_5) \sin \theta_{20}$$

$$H_2 = y_5$$

$$H_3 = -x_5 \sin \theta_{20} + (S_{20} + z_5) \cos \theta_{20} + S_{10}$$

where (H_1, H_2, H_3) are the co-ordinates of the centre of the cell in the neutron detector with respect to System II.

The direction cosines of the straight line joining the centres of the two cells i.e. $(x_3, y_3, S_{10} + z_3)$ in the scattering volume and (H_1, H_2, H_3) in

the neutron detector are:

$$A_4 : B_4 : C_4 = \frac{H_1 - x_3}{E} : \frac{H_2 - y_3}{E} : \frac{H_3 - (S_{10} + z_3)}{E}$$

$$\text{where } E = \{(H_1 - x_3)^2 + (H_2 - y_3)^2 + [H_3 - (S_{10} + z_3)]^2\}^{1/2}$$

These also are the direction cosines of the scattered neutron direction.

Hence the angle, θ_2 , between the incident neutron and the scattered neutron is given by:

$$\cos \theta_2 = A_2 A_4 + B_2 B_4 + C_2 C_4 \quad (\text{A1-3})$$

The direction cosines of the normal to the scattering plane are:

$$A_5 : B_5 : C_5 = \frac{B_2 C_4 - B_4 C_2}{F} : \frac{A_4 C_2 - A_2 C_4}{F} : \frac{A_2 B_4 - A_4 B_2}{F} \quad (\text{A1-4})$$

where

$$F = [(B_2 C_4 - B_4 C_2)^2 + (A_4 C_2 - A_2 C_4)^2 + (A_2 B_4 - A_4 B_2)^2]^{1/2}$$

From equations (A1-2) and (A1-4), the angle, ϕ , between the normals of the reaction and the scattering planes is given by

$$\cos \phi = A_3 A_5 + B_3 B_5 + C_3 C_5 \quad (\text{A1-5})$$

Because of the finite size of the scattering volume and the neutron detectors, $\cos \phi$ is equal to 1 only for the case when the production and the scattering of the neutrons occur in the same plane. In general, if the angle between \vec{n}_1 and \vec{n}_2 is ϕ (see equation 1-1 in Chapter 1), the right-left asymmetry, ϵ ,

is given by

$$\varepsilon = P_1 P_2 \cos \phi$$

instead of the expression in equation (1-2). Since the differential cross section, σ , of the scattered neutron is given by

$$\sigma = |g|^2 + |h|^2 ,$$

equation (1-3) can be written as:

$$P_2 \sigma = -2\text{Im}(g^* h)$$

In the computer program, $P_2 \sigma \cos \phi$ and σ are calculated for every combination of the cells in the scattering volume and the neutron detector. The average value of $P_2 \cos \phi$ is then given by:

$$\langle P_2 \cos \phi \rangle = \frac{\sum_{i=1}^N (P_2 \sigma \cos \phi)_i}{\sum_{i=1}^N \sigma_i} \quad (\text{A1-6})$$

where N is the total number of the possible combinations of the cells. In this way the average analysing power, $\langle P_2 \cos \phi \rangle$, is calculated.

For the completeness in describing the computation process in the program, some algebraic expressions will be given in the following paragraphs.

When $\delta_\ell = 0$ for $\ell > 2$, g and h (see equation (1-3)) can be written as

$$g = \frac{1}{k} \{ P_0(\cos\theta) [\sin\delta_0 e^{i\delta_0}] + P_1(\cos\theta) [2\sin\delta_1^+ e^{i\delta_1^+} + \sin\delta_1^- e^{i\delta_1^-}] \\ + P_2(\cos\theta) [3\sin\delta_2^+ e^{i\delta_2^+} + 2\sin\delta_2^- e^{i\delta_2^-}] \}$$

$$h = \frac{1}{k} \{ P_0^1(\cos\theta) \sin\delta_0 e^{i\delta_0} + P_1^1(\cos\theta) \sin(\delta_1^+ - \delta_1^-) e^{i(\delta_1^+ + \delta_1^-)} \\ + P_2^1(\cos\theta) \sin(\delta_2^+ - \delta_2^-) e^{i(\delta_2^+ + \delta_2^-)} \}$$

Separating g into its real, GR, and imaginary, GI, parts,

$$GR = (GR0) + (GR1)\cos\theta + (GR2) \cos^2\theta$$

$$\text{where } GR0 = \frac{1}{k} \{ \sin\delta_0 \cos\delta_0 - \frac{3}{2} \sin\delta_2^+ \cos\delta_2^+ - \sin\delta_2^- \cos\delta_2^- \}$$

$$GR1 = \frac{1}{k} \{ 2\sin\delta_1^+ \cos\delta_1^+ + \sin\delta_1^- \cos\delta_1^- \}$$

$$GR2 = \frac{1}{k} \{ \frac{9}{2} \sin\delta_2^+ \cos\delta_2^+ + 3\sin\delta_2^- \cos\delta_2^- \}$$

$$\text{and } GI = (GI0) + (GI1) \cos\theta + (GI2) \cos^2\theta$$

$$\text{where } GI0 = \frac{1}{k} \{ \sin^2\delta_0 - \frac{3}{2} \sin^2\delta_2^+ - \sin^2\delta_2^- \}$$

$$GI1 = \frac{1}{k} \{ 2\sin^2\delta_1^+ + \sin^2\delta_1^- \}$$

$$GI2 = \frac{1}{k} \{ \frac{9}{2} \sin^2\delta_2^+ + 3 \sin^2\delta_2^- \}$$

Similarly, separating h into its real, HR, and imaginary, HI, parts,

$$HR = (HR1) \sin\theta + (HR2) \sin 2\theta$$

where

$$HR1 = \frac{1}{k} \{ \sin \delta_1^+ \cos \delta_1^+ - \sin \delta_1^- \cos \delta_1^- \}$$

$$HR2 = \frac{1}{k} \left\{ \frac{3}{2} (\sin \delta_2^+ \cos \delta_2^+ - \sin \delta_2^- \cos \delta_2^-) \right\}$$

and

$$HI = (HI1) \sin \theta + (HI2) \sin 2\theta$$

where

$$HI1 = \frac{1}{k} \{ \sin^2 \delta_1^+ - \sin^2 \delta_1^- \}$$

$$HI2 = \frac{1}{k} \left\{ \frac{3}{2} (\sin^2 \delta_2^+ - \sin^2 \delta_2^-) \right\}$$

These phase shifts have been expressed as power series in neutron energies in Section 1-4 of Chapter I. A subroutine has been written to calculate the energies of the neutrons emitted at different angles from a nuclear reaction. This subroutine also calculates the centre-of-mass angle corresponding to the angle, θ_2 (equation (A1-3)), between the incident neutrons and the scattered neutrons, since the angles in the expressions for g and h are in the centre-of-mass system.

The kinematic expressions[†] used in the subroutine are given below.

Define

$$A = \frac{M_1 M_4 (E_1 / E_T)}{(M_1 + M_2) (M_3 + M_4)}$$

$$B = \frac{M_1 M_3 (E_1 / E_T)}{(M_1 + M_2) (M_3 + M_4)}$$

$$C = \frac{M_2 M_3}{(M_1 + M_2) (M_3 + M_4)} \left(1 + \frac{M_1}{M_2} \frac{Q}{E_T} \right)$$

[†] Obtained from page 162 of Nuclear Data Tables, Part 3, United States Atomic Energy Commission (1960).

$$D = \frac{M_2 M_4}{(M_1 + M_2)(M_3 + M_4)} \left(1 + \frac{M_1}{M_2} \frac{Q}{E_T}\right)$$

where

M_1 = mass of the incident particle

M_2 = mass of the target

M_3 = mass of the outgoing particle

M_4 = mass of the residual nucleus

E_1 = energy of the incident particle

Q = Q-value to the state in the residual nucleus

and $E_T = E_1 + Q$

The energy of the outgoing particle is then given by:

$$E_3 = E_T B [\cos \theta_{lab} \pm (D/B - \sin^2 \theta_{lab})^{1/2}]^2$$

The positive sign is used in the program to reduce the computer running time, since the double values only occur when the neutron energy is ≤ 100 keV. The centre-of-mass angle, θ_{cm} , of the outgoing particle is given by

$$\cos \theta_{cm} = \left(\frac{E_3}{E_T} - B - D \right) / [2(AC)^{1/2}]$$

For the case of n - ^4He scattering, the centre-of-mass angle is obtained by putting in the above expression, the appropriate masses and setting Q equal to zero.

A1.2 Description of the Computer Program

An alphabetic list of the definitions and symbols used in the program is given in Table A1-1. Tables A1-2 and A1-3 give the input and output quantities. Also at the end of the Appendix, a flow diagram and a Fortran listing are given.

TABLE A1-1

An Alphabetic List of Definitions and Symbols

| | |
|---------------|---|
| AMD | mass of deuteron |
| AMN | mass of neutron |
| AMP | mass of residual nucleus |
| AMT | mass of target nucleus |
| AVE(P2) | average value of P_2 |
| AVE(P2COSPHI) | average value of $P_2 \cos \phi$ |
| CPHI | $\cos \phi$ |
| DED | increment in deuteron energy |
| DTHE10 | increment in θ_{10} |
| E3 | energy of outgoing neutron in the finite geometry calculation |
| EDI | initial value of deuteron energy |
| EDF | final value of deuteron energy |
| EN | energy of outgoing neutron from the nuclear reaction |
| EXN | excitation energy of a state in the residual nucleus |
| NED | number of steps in the increment of E_D |
| NTHE10 | number of steps in the increment of θ_{10} |
| PPX3 | a running index for increment in PX3 |
| PPY3 | a running index for increment in PY3 |
| PPZ3 | a running index for increment in PZ3 |
| PPX5 | a running index for increment in PX5 |
| PPY5 | a running index for increment in PY5 |
| PPZ5 | a running index for increment in PZ5 |
| PX3 | number of parts into which the scattering volume is divided along the X_3 -axis |
| PY3 | number of parts into which the scattering volume is divided along the Y_3 -axis |
| PZ3 | number of parts into which the scattering volume is divided along the Z_3 -axis |

Table A1-1 (continued)

| | |
|--------|---|
| PX5 | number of parts into which the neutron detector is divided along the X_5 -axis |
| PY5 | number of parts into which the neutron detector is divided along the Y_5 -axis |
| PZ5 | number of parts into which the neutron detector is divided along the Z_5 -axis |
| P2X | $P_2\sigma$ |
| P2X0 | intermediate value of $P_2\sigma$ in the process of summation |
| P2XCPH | $P_2\sigma \cos\phi$ |
| P2XCP0 | intermediate value of $P_2\sigma \cos\phi$ in the process of summation |
| Q | Q-value to the ground state of the residual nucleus in the nuclear reaction |
| REACT | title of the nuclear reaction |
| S10 | distance between the target and the centre of the scattering volume |
| S20 | distance between the centre of the scattering volume and the front face of the neutron detector |
| THE10I | initial angle of the outgoing neutrons from the nuclear reaction for the increment in θ_{10} |
| THE10F | final angle of the outgoing neutrons from the nuclear reaction for the increment in θ_{10} |
| THE1L | angle of outgoing neutrons in the finite geometry calculation |
| THE20 | angle between the line joining the target and the centre of the scattering volume and the line joining the centres of the scattering volume and the neutron detector. |
| THE2C | scattered neutron angle in centre-of-mass system |
| THE2L | scattered neutron angle in laboratory system |
| THETA | angle of outgoing neutrons in the laboratory system |
| THETB | angle of outgoing neutrons in the centre-of-mass system |
| X | $n\text{-}^4\text{He}$ scattering cross section, i.e. σ |
| X0 | intermediate value of σ in the summation process. |

TABLE A1-2[†]

Input Quantities

| Card No. | Parameters | Format |
|----------|--------------------------------|--------------|
| 1 | REACT | 1X, 15H |
| 2 | AMD, AMT, AMN, AMP Q, EXN | 4F9.5, 2F7.4 |
| 3 | EDI, EDF, DED | 3F5.2 |
| 4 | PZ3, PX3, PY3 PZ5, PX5, PY5 | 6F6.1 |
| 5 | S10, S20, THE20 | 3F7.2 |
| 6 | THE10I, THE10F, DTHE10 | 3F7.2 |

[†] All masses are in amu, all energies are in MeV, all lengths are in cm and all angles are in degrees. Refer to Table A1-1 for explanation of parameters.

Table A1-3. A Sample Output of the Computer Program

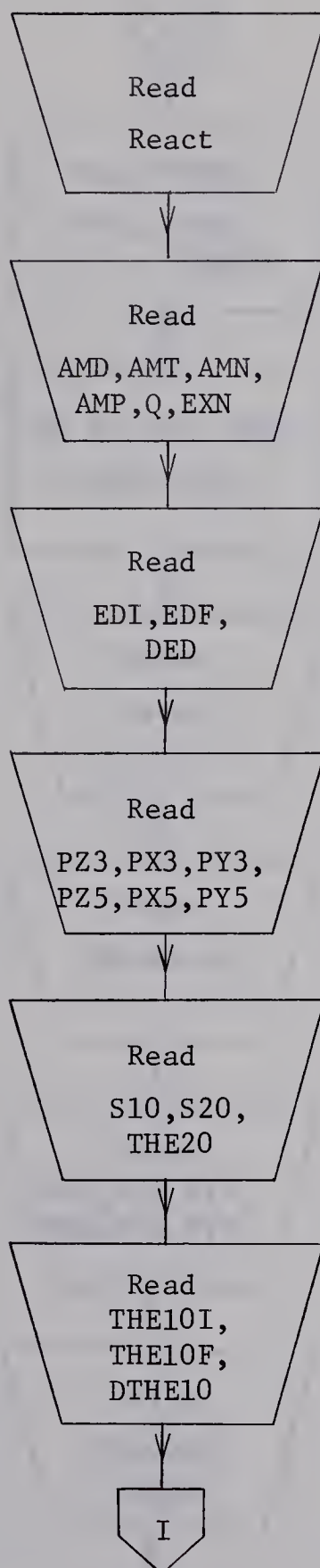
AVERAGE ANALYSING POWER FOR LIQUID HE4 POLARIMETER
SI28(D,N)P29

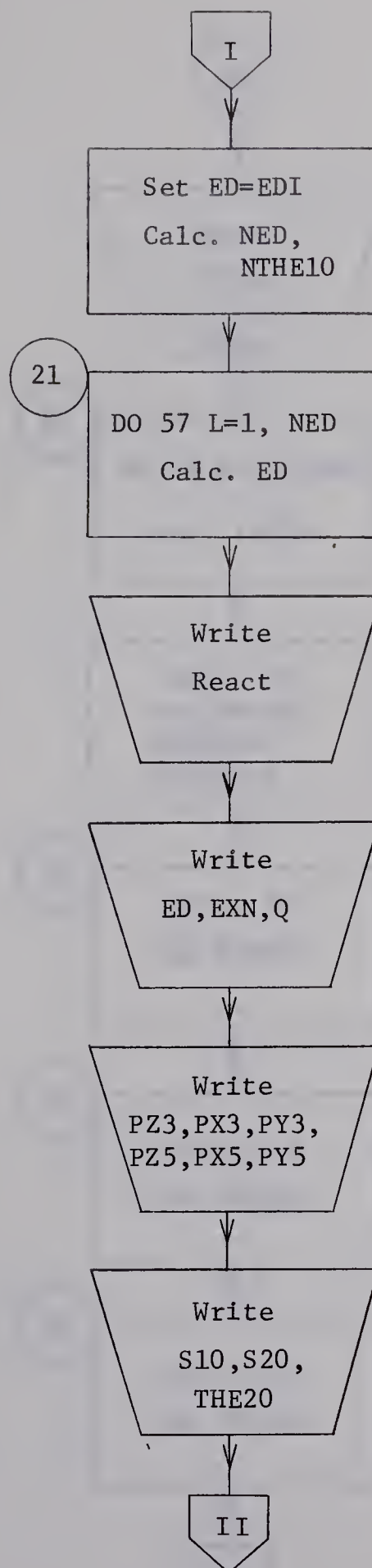
ED= 5.00MEV EXN= 0.0000MEV Q= 0.5200MEV

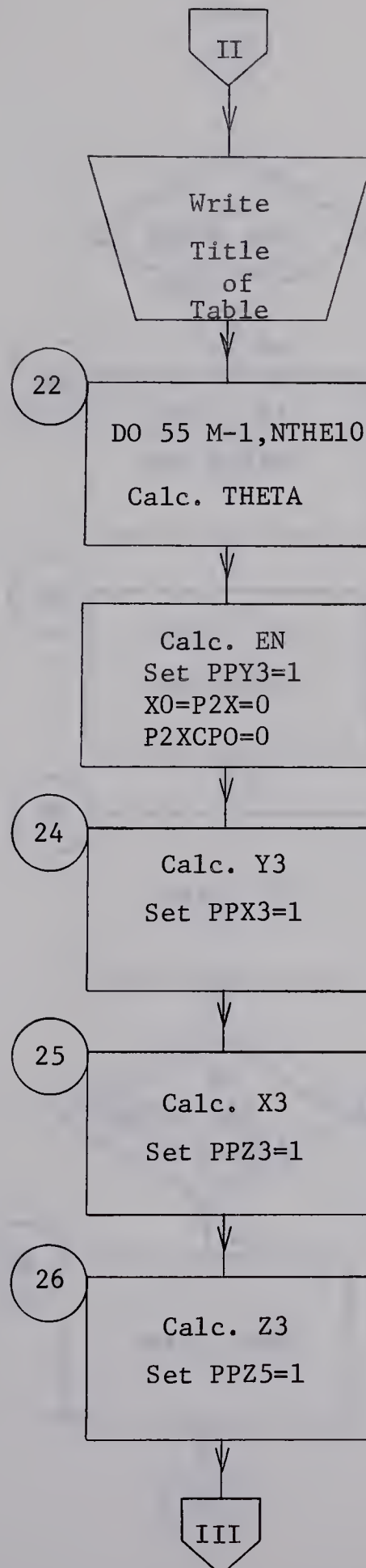
PZ3= 5.0 PX3= 5.0 PY3= 10.0
PZ5= 5.0 PX5= 9.0 PY5= 9.0
S10= 200.00CM S20= 25.00CM THE20= 123.00DEG

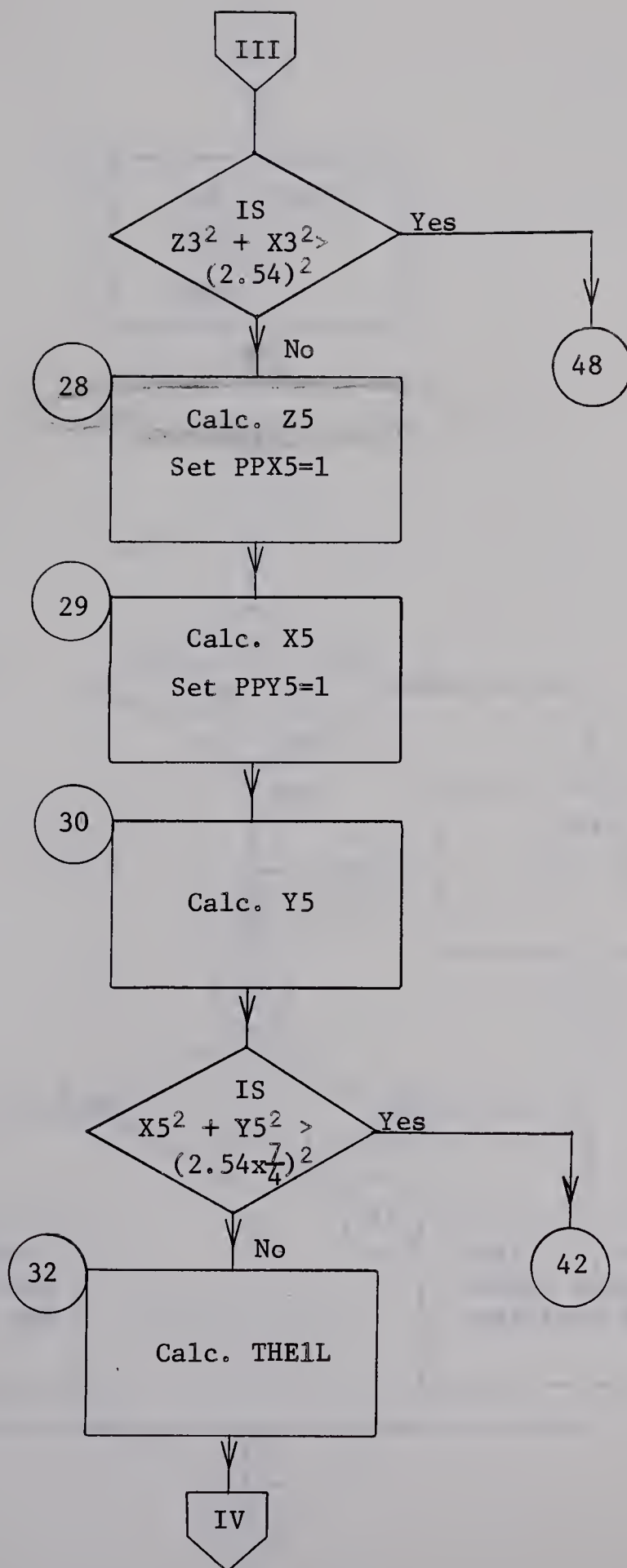
| THETA | THETB | EN(MEV) | TIME(NS/M) | AVE(P2) | AVE(P2COSPHI) |
|--------|--------|---------|------------|---------|---------------|
| 10.00 | 10.47 | 5.4889 | 30.84 | 0.9718 | 0.9519 |
| 20.00 | 20.93 | 5.4655 | 30.90 | 0.9721 | 0.9583 |
| 30.00 | 31.36 | 5.4274 | 31.01 | 0.9725 | 0.9605 |
| 40.00 | 41.75 | 5.3761 | 31.16 | 0.9731 | 0.9619 |
| 50.00 | 52.08 | 5.3135 | 31.34 | 0.9737 | 0.9631 |
| 60.00 | 62.36 | 5.2419 | 31.56 | 0.9744 | 0.9641 |
| 70.00 | 72.56 | 5.1637 | 31.79 | 0.9750 | 0.9651 |
| 80.00 | 82.65 | 5.0818 | 32.05 | 0.9756 | 0.9659 |
| 90.00 | 92.72 | 4.9986 | 32.31 | 0.9761 | 0.9666 |
| 100.00 | 102.68 | 4.9167 | 32.58 | 0.9765 | 0.9672 |
| 110.00 | 112.56 | 4.8387 | 32.84 | 0.9767 | 0.9677 |
| 120.00 | 122.36 | 4.7665 | 33.09 | 0.9769 | 0.9681 |

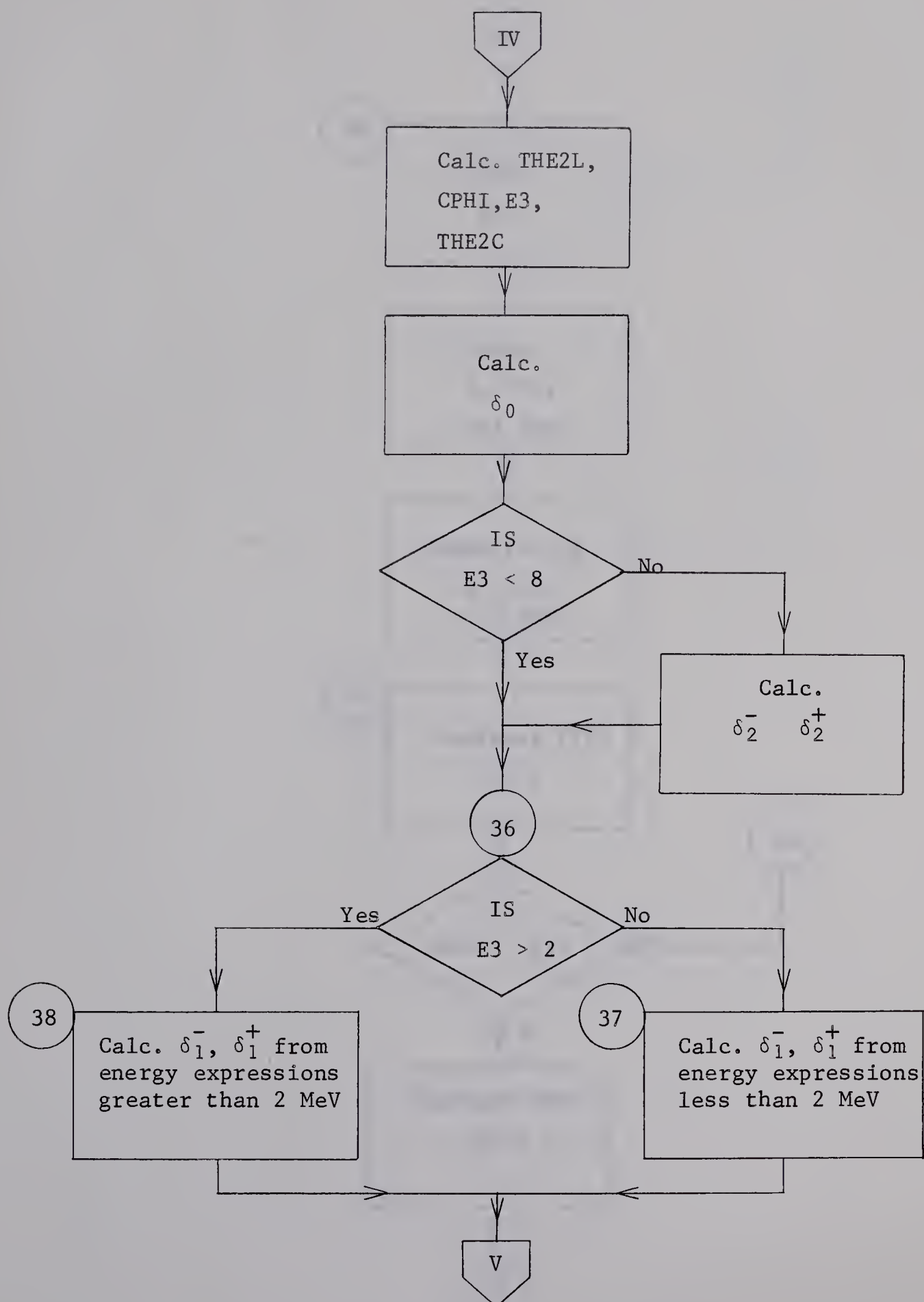
Flow diagram for the calculation of n-⁴He analysing power

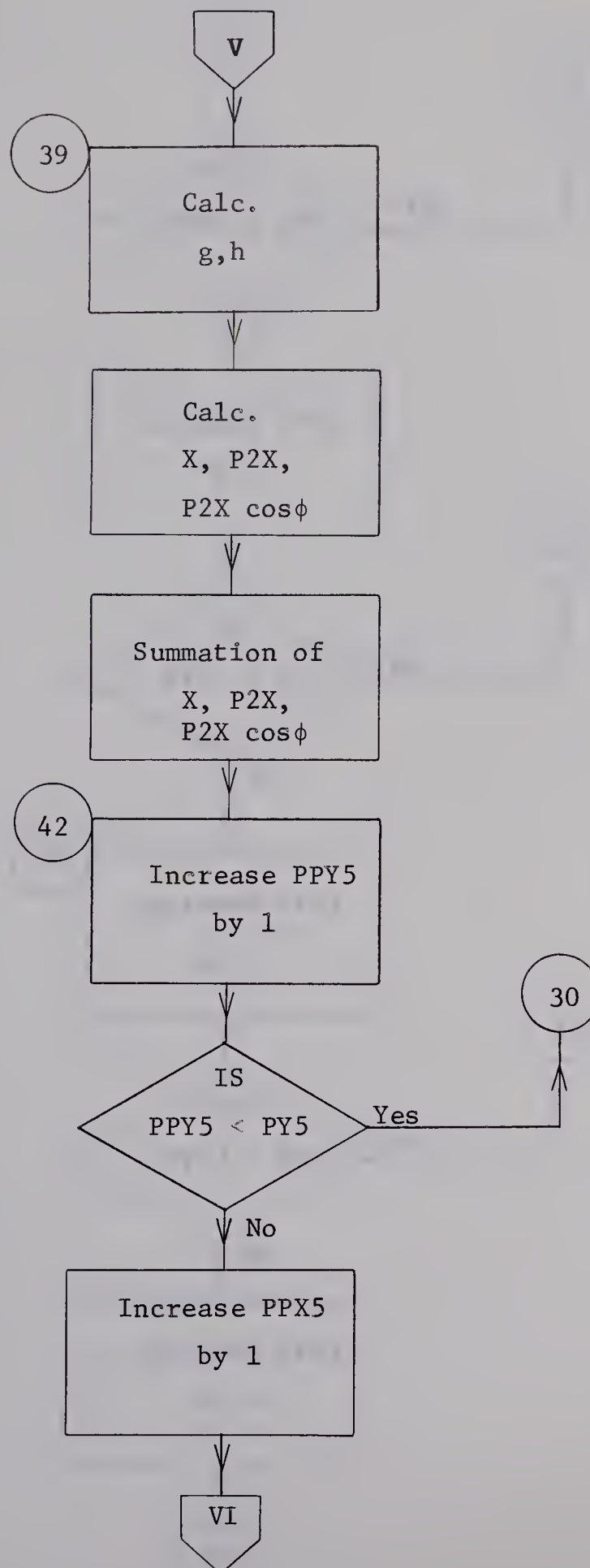


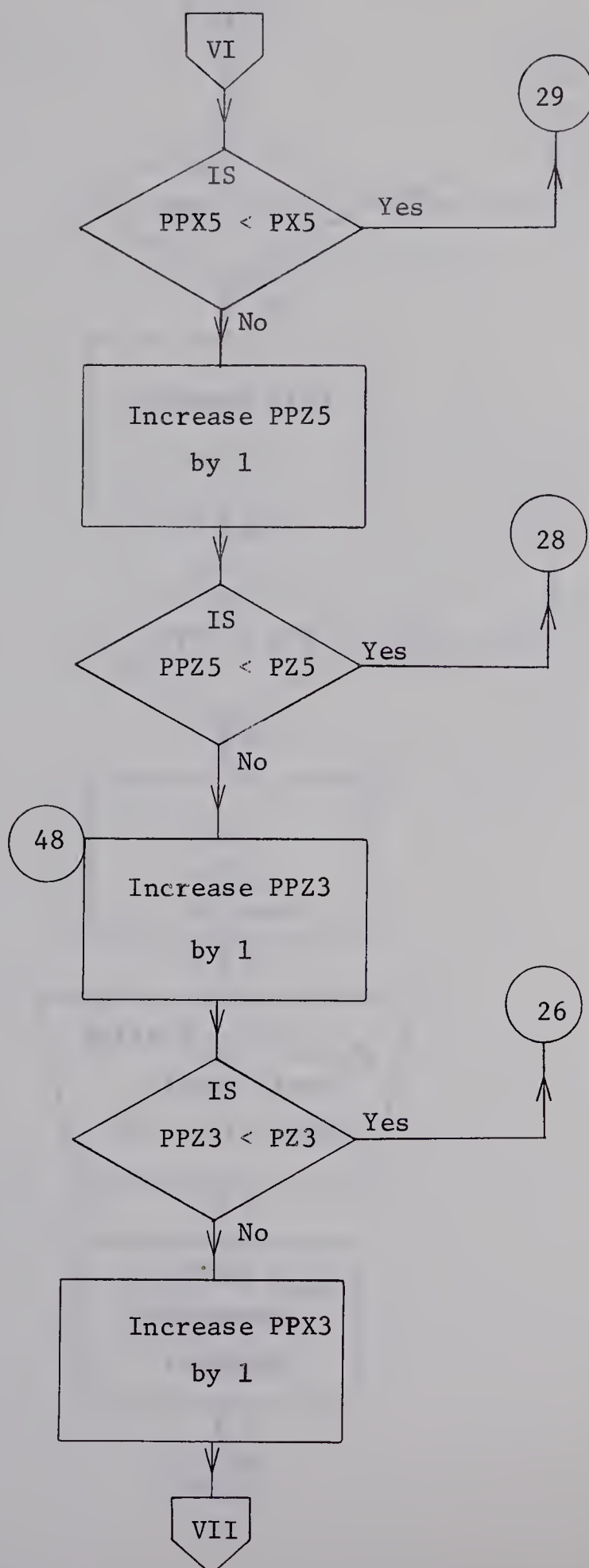


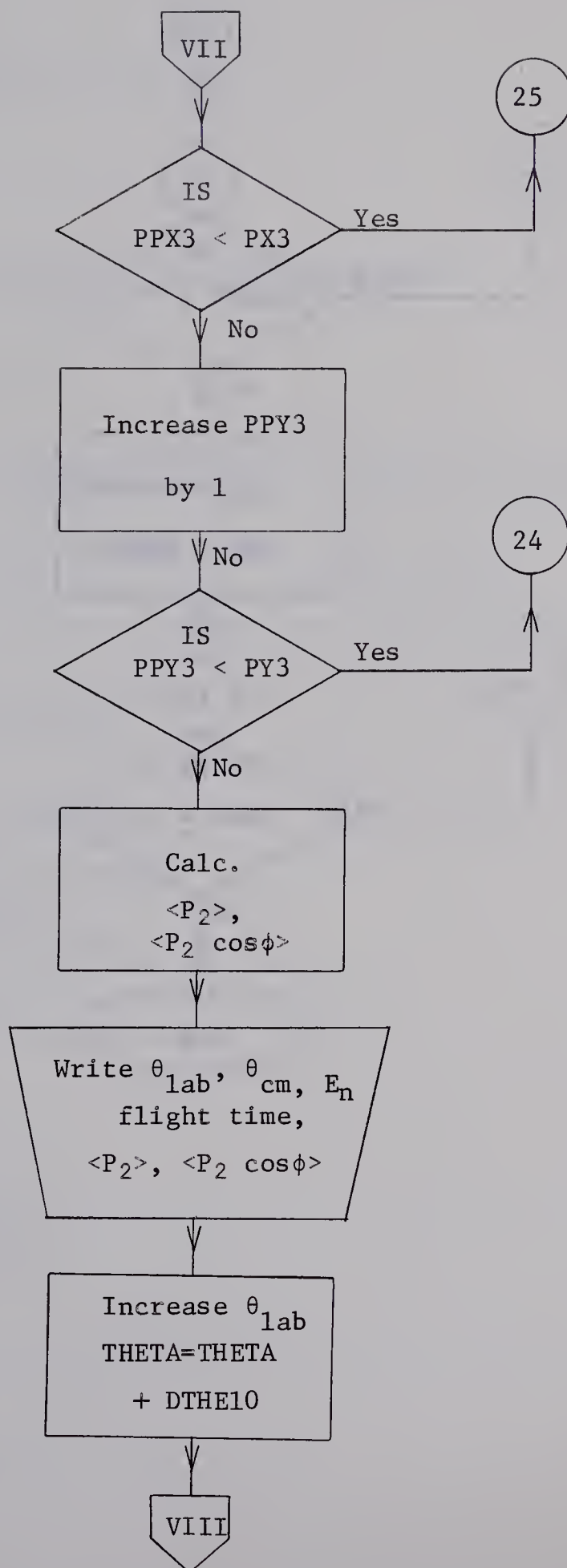


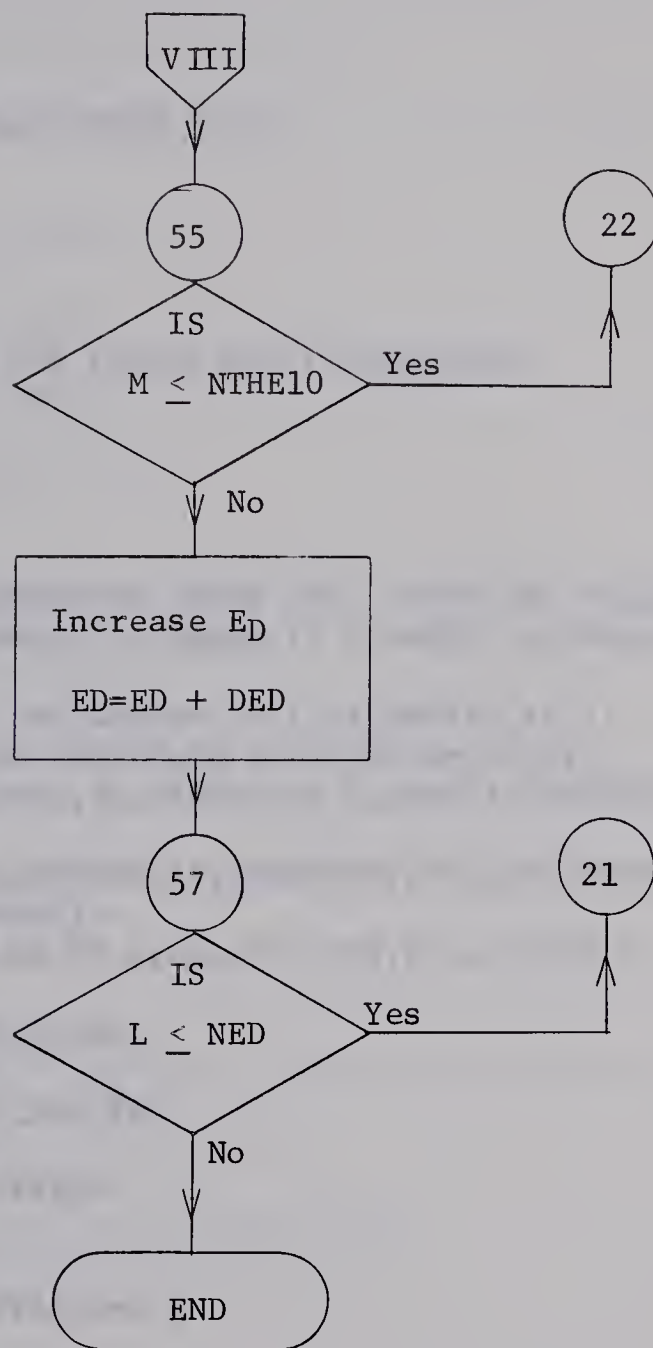












FORTRAN SOURCE LIST

SOURCE STATEMENT

\$IBFTC MAIN

```

C      AVERAGE ANALYSING POWER FOR LIQUID HE4 POLARIMETER
1      FORMAT(1X,15H
2      FORMAT(4F9.5,2F7.4)
3      FORMAT(3F5.2)
4      FORMAT(6F6.1)
5      FORMAT(3F7.2)
6      FORMAT(1H1,50HAVERAGE ANALYSING POWER FOR LIQUID HE4 POLARIMETER)
8      FORMAT(15X,3HED=,F5.2,3HMEV,7X,4HEXN=,F7.4,3HMEV,7X,2HQ=,F7.4,
13HMEV)
9      FORMAT(/,15X,4HPZ3=,F6.1,6X,4HPX3=,F6.1,6X,4HPY3=,F6.1)
10     FORMAT(15X,4HPZ5=,F6.1,6X,4HPX5=,F6.1,6X,4HPY5=,F6.1)
11     FORMAT(15X,4HS10=,F7.2,2HCM,3X,4HS20=,F7.2,2HCM,1X,6HTHE20=,F7.2,
13HDEG)
12     FORMAT(/,10X,5HTHETA,7X,5HTHETB,7X,7HEN(MEV),7X,10HTIME(NS/M),7X,7
1HAVE(P2),7X,13HAVE(P2COSPHI))
13     FORMAT(10X,F7.2,5X,F7.2,5X,F8.4,6X,F7.2,10X,F7.4,7X,F7.4)
      READ (5,1)
      READ(5,2)AMD,AMT,AMN,AMP,Q,EXN
      READ(5,3)EDI,EDF,DED
      READ(5,4)PZ3,PX3,PY3,PZ5,PX5,PY5
      READ(5,5)S10,S20,THE20
      READ(5,5)THE10I,THE10F,DTHE10
20     ED=EDI
      NED=(EDF-EDI)/DED+1.5
      NTHE10=(THE10F-THE10I)/DTHE10+1.5
21     DO 57 L=1,NED
      WRITE(6,6)
      WRITE(6,1)
      WRITE(6,8)ED,EXN,Q
      WRITE(6,9)PZ3,PX3,PY3
      WRITE(6,10)PZ5,PX5,PY5
      WRITE(6,11)S10,S20,THE20
      WRITE(6,12)
      U=0.0174533
      THETA=THE10I
22     DO 55 M=1,NTHE10
C      CALCULATION OF EN
      CTHETA=COS(THETA*U)

```



```

23 CALL ENEG(AMD,AMT,AMN,AMP,ED,Q,EXN,CTHETA,EN,THETB,TIME)
C  CALCULATION OF THEIL FOR OUT-GOING NEUTRON
    PPY3=1.0
    X0=0.0
    P2X0=0.0
    P2XCP0=0.0
24 Y3=-5.08+10.16*(PPY3-0.5)/PY3
    PPX3=1.0
25 X3=-2.54+5.08*(PPX3-0.5)/PX3
    PPZ3=1.0
26 Z3=-2.54+5.08*(PPZ3-0.5)/PZ3
    PPZ5=1.0
27 IF(Z3**2+X3**2.GT.6.45)GO TO 48
28 Z5=5.08*(PPZ5-0.5)/PZ5
    PPX5=1.0
29 X5=-4.445+8.89*(PPX5-0.5)/PX5
    PPY5=1.0
30 Y5=-4.445+8.89*(PPY5-0.5)/PY5
31 IF(X5**2+Y5**2.GT.19.84)GO TO 42
32 A1=-SIN(THETA*U)
    B1=0.0
    C1=COS(THETA*U)
    G=SQRT(X3**2+Y3**2+(S10+Z3)**2)
    A2=X3/G
    B2=Y3/G
    C2=(S10+Z3)/G
    CTHEIL=A1*A2+B1*B2+C1*C2
C  CALCULATION OF THE2L FOR SCATTERED NEUTRON AND COS(PHI) IN LAB.
C  SYSTEM
33 P1=X5*COS(THET20*U)+(S20+Z5)*SIN(THET20*U)
    P2=Y5
    P3=-X5*SIN(THET20*U)+(S20+Z5)*COS(THET20*U)+S10
    E=SQRT((P1-X3)**2+(P2-Y3)**2+(P3-S10-Z3)**2)
    A4=(P1-X3)/E
    B4=(P2-Y3)/E
    C4=(P3-S10-Z3)/E
    CTHE2L=A2*A4+B2*B4+C2*C4
    IF(THETA.EQ.0.0)GO TO 60
    IF(THETA.EQ.180.0)GO TO 60
34 D=SQRT((B1*C2-B2*C1)**2+(A2*C1-A1*C2)**2+(A1*B2-A2*B1)**2)
    A3=(B1*C2-B2*C1)/D
    B3=(A2*C1-A1*C2)/D
    C3=(A1*B2-A2*B1)/D
    F=SQRT((B2*C4-B4*C2)**2+(A4*C2-A2*C4)**2+(A2*B4-A4*B2)**2)
    A5=(B2*C4-B4*C2)/F
    B5=(A4*C2-A2*C4)/F
    C5=(A2*B4-A4*B2)/F
    CPHI=A3*A5+B3*B5+C3*C5
    GO TO 35

```



```

60  CPHI=1.0
C   CALCULATION OF E3
35  CALL ENEG(AMD,AMT,AMN,AMP,ED,Q,EXN,CTHEIL,E3,THETB1,TIME1)
C   CALCULATION OF THE2C FOR SCATTERED NEUTRON IN C.M. SYSTEM
AMD2=1.00898611
AMT2=4.00387611
AMN2=1.00898611
AMP2=4.00387611
Q2=0.0
EXN2=0.0
CALL ENEG(AMD2,AMT2,AMN2,AMP2,E3,Q2,EXN2,CTHE2L,E32,THE2C,TIME2)
C   CALCULATION OF PHASE SHIFTS
DTM=0.0
DTP=0.0
DZP=U*(180.0-21.7684*SQRT(E3)-2.63613*E3+.689548*E3**1.5)
IF(E3.LT.8.0) GO TO 36
DTM=U*(-.0725766*E3+.0133187*E3**2)
DTP=U*(.128117*E3-(.84296E-02)*E3**2+(.110985E-02)*E3**3)
36  IF(E3.GT.2.0) GO TO 38
37  DOP=U*(684.93-2312.49*SQRT(E3)+2493.53*E3-807.582*E3**1.5)
DOM=U*(2.45763*E3+3.55942*E3**2-.505754*E3**3)
TO TO 39
38  DOP=U*(.0648862+180.513*SQRT(E3)-92.6748*E3+19.1394*E3**1.5
1-1.43251*E3**2)
DOM=U*(-10.9749+14.8534*E3-.97544*E3**2+.0197815*E3**3)
C   CALCULATION OF G AND H
39  CTHE2C=COS(THE2C*U)
STHE2C=SIN(THE2C*U)
SDZP=SIN(DZP)
CDZP=COS(DZP)
SDOP=SIN(DOP)
CDOP=COS(DOP)
SDOM=SIN(DOM)
CDOM=COS(DOM)
SDTM=SIN(DTM)
CDTM=COS(DTM)
SDTP=SIN(DTP)
CDTP=COS(DTP)
HK=(1.54617E+12)*SQRT(2.0*AMN*E3)
HKI=1.0/HK
GRO=HKI*(SDZP*CDZP-SDTP*CDTP*3.0/2.0-SDTM*CDTM)
GR1=HKI*(2.0*SDOP*CDOP+SDOM*CDOM)
GR2=HKI*(SDTP*CDTP*9.0/2.0+3.0*SDTM*CDTM)
GR=GRO+GR1*CTHE2C+GR2*CTHE2C*CTHE2C
GIO=HKI*(SDZP*SDZP-SDTP*SDTP*3.0/2.0-SDTM*SDTM)
GI1=HKI*(2.0*SDOP*SDOP+SDOM*SDOM)
GI2=HKI*(SDTP*SDTP*9.0/2.0+3.0*SDTM*SDTM)
GI=GIO+GI1*CTHE2C+GI2*CTHE2C*CTHE2C

```



```

HR1=HKI*(SDOP*CDOP-SDOM*CDOM)
HR2=HKI*(SDTP*CDTP-SDTM*CDTM)*3.0/2.0
HR=HR1*STHE2C+HR2*SIN(2.0*THE2C*U)
HI1=HKI*(SDOP*SDOP-SDOM*SEOM)
HI2=HKI*(SDTP*SDTP-SDTM*SDTM)*3.0/2.0
HI=HI1*STHE2C+HI2*SIN(2.0*THE2C*U)
40  X=GR*GR+GI*GI+HR*HR+HI*HI
    P2X=2.0*(GI*HR-GR*HI)
    P2X=2.0*(GI*HR-GR*HI)
    P2XCPH=P2X*CPHI
    X0=X0+X
    P2X0=P2X0+P2X
    P2XCP0=P2XCP0+P2XCPH
42  PPY5=PPY5+1.0
43  IF(PPY5.LT.PY5)GO TO 30
44  PPX5=PPX5+1.0
45  IF(PPX5.LT.PX5)GO TO 29
46  PPZ5=PPZ5+1.0
47  IF(PPZ5.LT.PZ5) GO TO 28
48  PPZ3=PPZ3+1.0
49  IF(PPZ3.LT.PZ3)GO TO 26
50  PPX3=PPX3+1.0
51  IF(PPX3.LT.PX3)GO TO 25
52  PPY3=PPY3+1.0
53  IF(PPY3.LT.PY3)GO TO 24
    AVP2=P2X0/X0
    AP2CPH=P2XCP0/X0
    WRITE(6,13)THETA,THETB,EN,TIME,AVP2,AP2CPH
55  THETA=THETA+DTHE10
57  ED=ED+DED
    CALL EXIT
    END

```


FORTRAN SOURCE LIST

SOURCE STATEMENT

\$IBFTC ENEG

C KINEMATICS AT ONE ANGLE

SUBROUTINE ENEG(AMU1,AMU2,AMU3,AMU4,E1,QO,EXN,CTHETA,E3,THETB,TIME
1)

U=0.0174533

Q=QO-EXN

ET=E1+Q

AMU=(AMU1+AMU2)*(AMU3+AMU4)

A=AMU1*AMU4*E1/(ET*AMU)

B=AMU1*AMU3*E1/(ET*AMU)

C=AMU2*AMU3*(1.0+AMU1*Q/(AMU2*ET))/AMU

D=AMU2*AMU4*(1.0+AMU1*Q/(AMU2*ET))/AMU

E3=ET*B*(CTHETA+SQRT(D/B-(1.0-CTHETA*CTHETA)))*2

CTHETB=(E3/ET-B-D)/(2.0*SQRT(A*C))

IF(CTHETB.LT.(-1.0))GO TO 13

10 THETB=ARCOS(CTHETB)

GO TO 12

13 THETB=3.14159

12 THETB=THETB/U

TIME=72.24618/SQRT(E3)

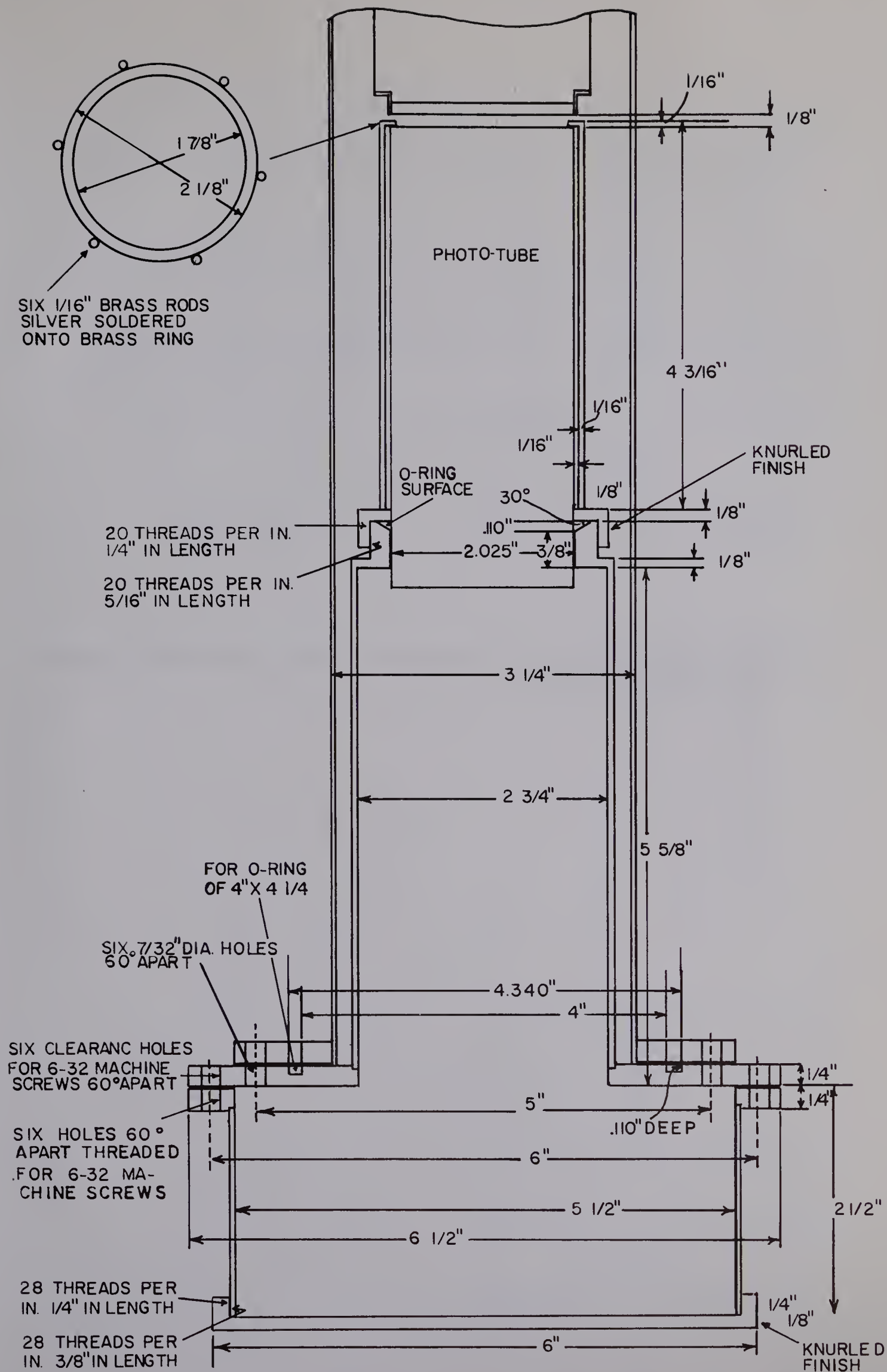
RETURN

END

APPENDIX 2

SOME SCHEMATIC DRAWINGS

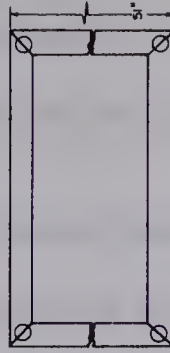
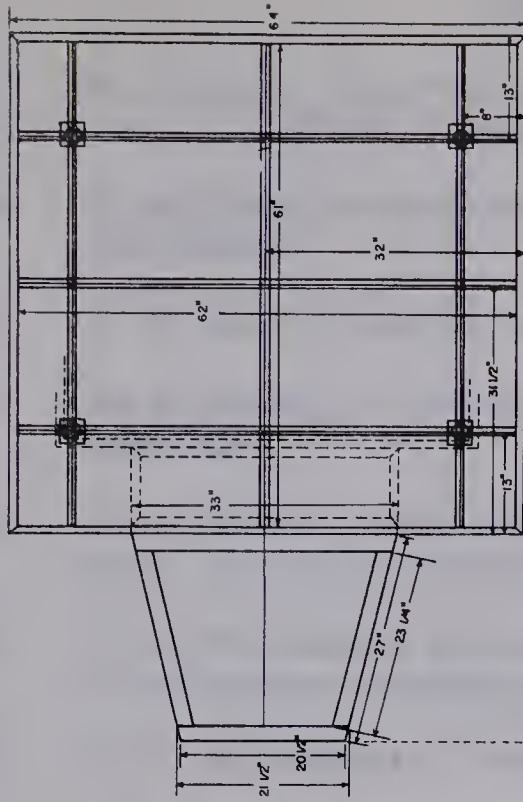
A2-1 A schematic drawing for mounting a RCA 8575 phototube to the tail section of the cryostat



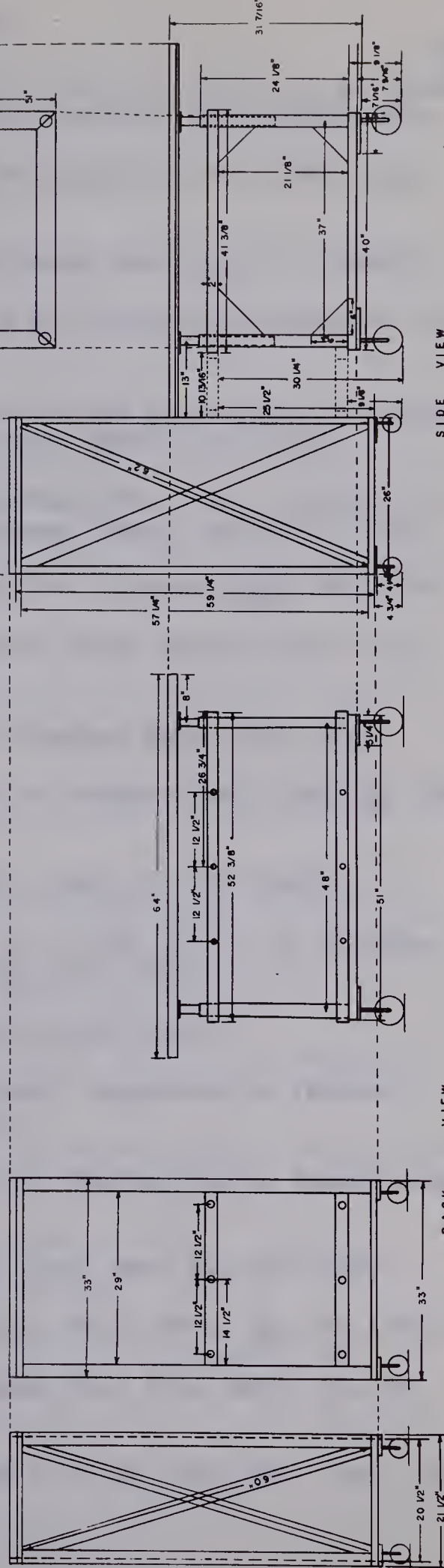
A2-2 A schematic drawing of the channel iron cart for mounting the polarization system

POLARIZATION CART
AND SHIELD SUPPORT

TOP VIEW



SIDE VIEW



BACK VIEW

- Au 63 N. Austern, Fast Neutron Physics Part II, ed. by J. B. Marion and J. L. Fowler (Interscience, New York, 1963) Chapt. V.D.
- Ba 60A Sign Convention for Particle Polarization, Nucl. Phys. 21, 696 (1960)
- Ba 60B J. A. Baicker and K. W. Jones, Nucl. Phys. 17, 424 (1960)
- Ba 61 R. H. Bassel, R. M. Drisko and G. R. Satchler, DWBA code Julie, ORNL-3240
- Ba 64 R. H. Bassel, Some Applications of the Distorted Wave Approximation for Direct Nuclear Reactions, ORNL-P-144 (1964)
- Bi 60 L. C. Biedenharn and G. R. Satchler, Proc. Int. Symposium on Polarization Phenomena of Nucleons (Basel, July 4-8, 1960)
- B1 51 R. J. Blin-Stoyle, Proc. Phys. Soc. (London) 64A, 700 (1951)
- B1 52 J. M. Blatt and L. C. Biedenharn, Revs. Modern Physics 24, 258 (1952)
- Bu 51 S. T. Butler, Proc. Roy. Soc. (London) 208A, 559 (1951)
- Bu 60 B. Buck, R. N. Maddison and P. E. Hodgson, Phil. Mag. 5, 1181 (1960)
- Bu 61 B. Buck and P. E. Hodgson, Phil. Mag. 6, 1371 (1961)
- Bu 66 S. G. Buccino, D. S. Gemmel, L. L. Lee, Jr., J. P. Schiffer and A. B. Smith, Nucl. Phys. 86, 353 (1966)
- Da 59 W. W. Daehnick, Phys. Rev., 115, 1008 (1959)
- Da 66A W. G. Davies, Ph.D. thesis (1966), Department of Physics, University of Alberta, Edmonton
- Da 66B W. G. Davies, W. K. Dawson, G. C. Neilson and K. Ramavataram, Nucl. Phys. 76, 65 (1966)
- Do 52 D. C. Dodder and J. L. Gammel, Phys. Rev. 88, 520 (1952)
- Du 61 P. S. Dubbeldam and R. L. Walter, Nucl. Phys. 28, 414 (1961)
- Es 65 R. J. Esterling and N. H. Lipman, Rev. Sci. Instr. 36, N4, 493 (1965)
- Fl 59 H. Fleishman, H. Einbinder and C. S. Wu, Rev. Sci. Instr. 30, N12, 1130 (1959)

- Ga 58 J. L. Gammel and R. M. Thaler, Phys. Rev. 109, 2041 (1958)
- Ha 63 W. Haeberli, Fast Neutron Physics, Part II, Chapter V.G. Interscience Publishers (1963)
- Ho 66 B. Hoop, Jr. and H. H. Barschall, Nucl. Phys. 83, 65 (1966)
- Hu 58 R. Huby, M. Refai, G. R. Satchler, Nuclear Physics 9, 94 (1958)
- Jo 62 R. C. Johnson, Nucl. Phys. 35, 654 (1962)
- Ju 66 Memorandum to users of the code JULIE, Oak Ridge National Laboratory, 1966. Also ORNL-3240, 1962
- Ka 63 J. R. Kane, R. T. Siegal and A. Suzuki, Rev. Sci. Instr. 34, 817 (1963)
- Le 50 J. V. Lepore, Phys. Rev. 79, 137 (1950)
- Le 57 I. Levintov, A. Miller, E. Tarumov and V. Shamshev, Nucl. Phys. 3, 237 (1957)
- Le 64A L. L. Lee, Jr. and J. P. Schiffer, Phys. Rev. Letters 12, 108 (1964)
- Le 64B L. L. Lee, Jr., J. P. Schiffer, B. Zeidman, G. R. Satchler, R. M. Drisko and R. H. Bassel, Phys. Rev. 136, 971B (1964)
- Ma 64 B. E. F. Macefield, A Compilation of Computer Codes Useful in Nuclear Structure Physics (BNL-9108), 1964
- Me 54 R. Meier, P. Scherrer and G. Trumpy, Helv. Phys. Acta 27, 577 (1954)
- Mi 65 D. W. Miller, Proceedings of the Second International Symposium on Polarization Phenomena of Nucleons, Karlsruhe, 1965
- Ne 53 H. C. Newns, Proc. Phys. Soc. (London) 66A, 477 (1953)
- Pa 58 P. J. Pasma, Nucl. Phys. 6, 141 (1958)
- Pe 66 C. M. Perey and F. G. Perey, Phys. Rev. 152, 923 (1966)
- Pu 65 F. O. Purser, Jr., J. R. Sawers, Jr. and R. L. Walter, Phys. Rev. 140, 870B (1965)

- Ro 59 L. S. Rodberg, Nucl. Phys. 15, 72 (1959)
- Ro 65 L. Rosen, Proceedings of the Second International Symposium on Polarization Phenomena of Nucleon, 1965
- Sa 64 G. R. Satchler, Nucl. Phys. 55, 1 (1964)
- Sa 65 G. R. Satchler, Some Topics in the Theory of Direct Nuclear Reactions, University of Colorado Press (1965)
- Sc 46 J. Schwinger, Phys. Rev. 69, 681 (1946)
- Sc 48 J. Schwinger, Phys. Rev. 73, 407 (1948)
- Se 53 J. D. Seagrave, Phys. Rev. 92, 1222 (1953)
- Si 61 J. E. Simmons and R. B. Perkins, Rev. Sci. Instr. 32, N11, 1173 (1961)
- Te 66 J. W. Tepel, Nucl. Instr. and Meth. 40, 100 (1966)
- Th 59 E. H. Thorndike and W. J. Shalaer, Rev. Sci. Instr. 30, 838 (1959)
- To 61 S. V. Topp and F. L. Hereford, Rev. Sci. Instr. 32, N11, 1173 (1961)
- To 61 W. Tobocman, Theory of Direct Nuclear Reactions, Oxford University Press, 1961
- To 66 M. A. Toosi and E. V. Ivash, Annual Progress Report, Accelerator Laboratory, University of Texas, Dec., 1966
- We 66 W. G. Weitkamp and W. Haeberli, Nucl. Phys. 83, 46 (1966)
- Wi 63 D. L. Weiber, Nucl. Instr. and Meth. 24, 269 (1963)
- Wo 49 L. Wolfenstein, Phys. Rev. 75, 1664 (1949)
- Wo 54 L. Wolfenstein, Phys. Rev. 96, 1654 (1954)
- Wo 56 L. Wolfenstein, Ann. Rev. Nucl. Sci. 6 (1956)

B29878